Alma Mater Studiorum - Università di Bologna

DOTTORATO DI RICERCA IN

Meccanica e Scienze Avanzate Dell'Ingegneria

Ciclo XXXII

Settore scientifico-disciplinare: ING-IND/19 IMPIANTI NUCLEARI

Settore concorsuale: 09/C2

On the optimal control of steady fluid structure interaction systems

Presentata da Leonardo Chirco

Coordinatore Dottorato	Relatore
Chiar.mo Prof. Ing. Marco Carricato	Chiar.mo Prof. Ing. Sandro Manservisi

---

Esame finale anno 2020

For Mum and Dad

Contents

Abstract

Fluid-structure interaction (FSI) systems consist of one or more solid structures that deform by interacting with a surrounding fluid flow and are commonly studied in many engineering and biomedical fields. Usually those kind of problems are solved in a direct approach, however it is also interesting to study the inverse problem, where the goal is to find the optimal value of some control parameters, such that the FSI problem solution is close to a desired one. In this work the optimal control problem is formulated with the Lagrange multipliers and adjoint variables formalism. In order to recover the symmetry of the state-adjoint system an auxiliary displacement field is introduced and used to extend the velocity field to the structure domain. As a consequence, the adjoint interface forces are balanced automatically. The optimality system is derived from the first order necessary condition by taking the Fréchet derivatives of the augmented Lagrangian with respect to all the variables involved. The optimal solution is obtained through a gradient-based algorithm applied to the optimality system. In order to support the proposed approach numerical test with distributed control, boundary control and parameter estimation are performed.

Introduction

Optimization has always been a key aspect in the field of engineering in order to improve the performance of existing devices or to create better ones. As long as the goals to pursue are trivial, improvements can be attained by trial and error without the use of sophisticated mathematical models. When the problem becomes complex the use of the appropriate optimization techniques is instead essential. In this work we refer to adjoint based methods, which have been proven to be a good approach for the optimal control of complex problems where computational fluid dynamics simulations can be performed on the system of interest, see for example [41, 38]. Moreover, these methods have a solid mathematical background and the existence of local optimal solutions can be proven for many interesting cases, [30].

In order to describe the behavior of a dynamical system different mathematical models can be adopted taking into account the peculiarities of the problem and the grade of accuracy that one aims to recover. Lumped-parameter models simplify the description of the behavior of spatially distributed physical systems into a set of discrete entities that, under certain assumptions, approximate the behavior of the distributed system. This approach is used for instance in electronics to substitute Maxwell's equations with Kirchhoff's circuit laws. Ordinary differential equations often model one-dimensional dynamical systems with functions of a single variable and their derivatives. On the other hand, multidimensional phenomena where the variables depend both on time and on the spatial components are modeled by mean of partial differential equations (PDE). Common examples include heat and wave propagation, electrodynamics, quantuum mechanics, fluid and solid motion. In fluid-structure interaction (FSI) the latter two are coupled into a single problem and the set of PDEs describing fluid and solid motion has to be satisfied simultaneously. In this case the fluid-structure mutual interaction is fundamental since the behavior of the solid affects the fluid and vice versa. In details, the fluid, through its pressure, behaves as an external load over the solid structure that deforms and changes the shape of the channel which modifies the fluid dynamic state inside the channel itself.

Many FSI studies have been published in recent years but the optimal control of such problems is still an open challenge. In fact, only few optimal control studies of FSI systems can be found in literature, see for examples [23, 7, 48]. In the recent work [23] the authors study a linear unsteady FSI optimal control problem, written in monolithic form, and introduce a solid velocity so that the adjoint system has the same properties of the state system. In [7] the authors deal with an adjoint formulation for a time-dependent distributed control, namely a force acting on a part of the solid domain, to match a target displacement. In [48] the authors propose a solution approach based on a Newton method to solve Young modulus estimation and stationary optimal control problems. However, in all the steady cases found in literature the optimality system comes directly from the steady FSI equations. The time is not present and the non linear algorithm to recover the final deformation is implicitly determined. Furthermore, the balance between the adjoint displacement, the adjoint velocity and the final deformed interface must be recovered after many non linear iterations. Differently from these approaches, with this new method we desire to recover the symmetry of the state-adjoint system that is characteristic of the time dependent problem where the final deformation is obtained step by step. In order to do this we introduce an auxiliary displacement field and use it to extend the velocity field to the structure domain. As a consequence, the adjoint interface forces are balanced automatically. It is worth pointing out that in this steady optimization problem the physical velocity in the solid is zero, while the fictitious velocity is used as the driving force for the solid motion during the optimization process.

In this work the FSI state and adjoint systems are written in a monolithic form. There are several motivations behind this approach. First, the coupling conditions at the fluid-solid interface are automatically taken into account in the monolithic variational formulation and no sub-iterations are necessary as in the case of partitioned approaches. Furthermore, since in the framework of FSI gradient-based optimization the solution of the adjoint system is used to determine the gradient of the functional, then it is important to solve with a stable and robust method that treats accurately the propagation of the information across the interface. Finally, with this approach, we can use the same solver for both the state and adjoint systems with minor modifications.

This work is organized as follows. In Chapter 1 the FSI framework is introduced under the hypothesis of a continuum material. We first describe the basic principles of the kinematics of such medium in Lagrangian coordinates and in Eulerian ones. By introducing the *Arbitrary Lagrangian Eulerian* mapping we derive the conservation laws of mass and momentum that describe the FSI problem. A brief review of the most common constitutive models for fluids and solids is then reported. The monolithic variational formulation suitable for a Finite Element implementation of the FSI problem is recovered. Finally, we validate our FEM code by performing some well known direct FSI benchmarks available in literature. In Chapter 2 the basic principles of adjoint optimal control are presented and a simple heat conduction example is used in order to introduce and clarify the fundamental aspects of the method. Finally, the algorithms and techniques used to solve a general stationary FSI optimal control problem are illustrated. In Chapter 3 a pressure boundary control problem for the minimization of a solid displacement matching functional is studied. The control aims to find the optimal pressure on a fluid boundary such as the inlet or an auxiliary duct. We implement a simple steepest descent algorithm to determine the gradient direction for the iterative solution of the optimality system. In order to improve the convergence properties of the method we propose a quasi-Newton one. By performing some test cases we compare the performance of these two methods in terms of convergence rate and accuracy. In Chapter 4 we study a distributed optimal control approach. A volumetric force acts on the solid and changes the shape of the structure in order to recover the desired objective. We consider both fluid velocity and solid displacement matching functionals. This approach can be used in practical application to reformulate complex FSI shape optimization problems into simpler distributed control ones. In Chapter 5 an inverse Young modulus estimation problem is studied. In this case the control parameter used is one of the solid material physical properties and the objective is a displacement mismatch minimization. This problem has many industrially relevant applications, since changes in the mechanical properties as a function of temperature are commonly visible. Upper and lower limits on the control are taken into account in order to avoid negative or very high values of the Young modulus, obtaining a variational inequality in the optimality system. We present a projected gradient method in order to deal with these control inequality constraints.

CHAPTER 1

Fluid Structure Interaction

In fluid-structure interaction (FSI) problems, one or more solid structures deform due to the interaction with a surrounding fluid flow. The flow behavior depends on the shape and motion of the structure while the deformation of the structure depends on the fluid mechanics forces acting on the structure. FSI simulations evaluate the stress state of the mechanical component due to the surrounding fluid flow and take into account the effects of the solid deformations on the motion of the interior flows. Furthermore, the FSI effects become more relevant when the dependence between the influence and response becomes stronger.

FSI problems are becoming of great interest in the scientific community since they play an important role in the design of several components. The fluttering of aircraft wings, flapping of an airport windsock, deflection of wind-turbine blades, falling of a leaf, inflation of automobile airbags, dynamics of spacecraft parachutes, and the interaction between blood flow and cardiovascular tissue, are all FSI examples. In literature many works can be found dealing with this subject and the interested reader can see [57, 24, 36, 12, 26, 13, 5, 58, 14, 15, 4] and references therein.

The inherently non linear and time dependent nature of FSI makes it very difficult to use analytical methods in this class of problems. Only a handful of cases have been studied analytically, where simplifying hypotheses have been assumed to find closed-form solutions of the underlying partial differential equations. One can apply some analytical methods in solution of fluid-only or structure-only problems but only few analytical techniques can be extended successfully to the solution of FSI problems. In contrast, there have been significant advances in computational FSI research in recent decades since stable and efficient FSI solvers would be indispensable tools for industry, research laboratories, medical fields, space exploration, and many other contexts.

A comprehensive study of FSI problems remains an open challenge due to their strong non linearity and multi-physics nature. The sets of differential equations and boundary conditions associated with the fluid and structure domains must be satisfied simultaneously. The domains do not overlap and the two systems are coupled at the fluid-structure interface, which requires a set of physically meaningful interface conditions. These coupling conditions are the kinematics compatibility laws and stress balances at the fluid-structure interfaces. The structure domain is in motion and, in most cases, its motion follows the material structure particles or points. This is known as the Lagrangian description of the structural motion. As the structure moves through space, the shape of the fluid subdomain changes to conform to the motion of the structure. The motion of the fluid domain needs to be accounted for in the differential equations and boundary conditions. There are two major classes of methods for tracking the structure deformation, which are known in the discrete setting as the non moving-grid and moving-grid approaches. Furthermore, the motion of the fluid domain is not known a priori since it is a function of the unknown structural displacement. This makes FSI a three-field problem, where the third unknown is the motion of the fluid domain.

The additional challenges in FSI come from the discretization at the fluid-structure interface. The most flexible option is, of course, to have separate fluid and structure discretizations for the individual sub-problems, which results in non-matching meshes at the interface. In this case, one needs to ensure that, despite the non-matching interface meshes, the fluid and structure have the correct coupling of the kinematics and stress profiles. A simpler option is to have matching discretizations at the fluid-structure interface. In this case, the satisfaction of the FSI coupling conditions is much less challenging. However, this choice leads to a lack of flexibility in the discretization choices and mesh refinement levels for the fluid and structure sub-problems. That flexibility becomes increasingly important as the complexity of the fluid-structure interface geometry increases. On the other hand, there are situations where having matching discretizations at the interface is the most effective approach. Another computational challenge in some FSI applications is the need to accommodate very large structural motions. In this case, one needs a robust mesh moving technique and the option to periodically regenerate the fluid mechanics mesh (i.e., re-mesh) to preserve the mesh quality and consequently the accuracy of the FSI computations. The re-meshing procedure requires the interpolation of the solution from the old mesh to the new one. Re-meshing and data interpolation are also necessary for fluid-only computations over domains with known motion. The difference between that and FSI is that the re-meshing can be precomputed in such fluid-only simulations, while in the case of FSI the fluid mechanics mesh quality depends on the unknown structural displacements, and the decision to re-mesh is made on the fly.

There are two major classes of FSI coupling techniques: loosely-coupled and strongly-coupled, which are also referred to as staggered and monolithic, respectively. Monolithic coupling often refers to strong coupling with matching interface discretizations. In loosely-coupled approaches, the equations of fluid mechanics, structural mechanics, and mesh moving are solved sequentially. For a given time step, a typical loosely-coupled algorithm involves the solution of the fluid mechanics equations with the velocity boundary conditions coming from the extrapolated structure displacement rate at the interface, followed by the solution of the structural mechanics equations with the updated fluid mechanics interface traction, and followed by the solution of the mesh moving equations with the updated structural displacement at the interface. This enables the use of existing fluid and structure solvers, a significant motivation for adopting this approach. In addition, for several problems the staggered approach works well and is very efficient. However, convergence difficulties are encountered sometimes, most commonly when the structure is light and the fluid is heavy, and when an incompressible fluid is fully enclosed by the structure. In strongly-coupled approaches, the equations of fluid, structure, and mesh moving are solved simultaneously, in a fully-coupled fashion. The main advantage is that strongly-coupled solvers are more robust. Many of the problems encountered with the staggered approaches are avoided. However, strongly-coupled approaches necessitate writing a fully-integrated FSI solver, virtually precluding the use of existing fluid and structure solvers. There are three categories of coupling techniques in strongly-coupled FSI methods: block-iterative, quasi-direct, and direct coupling. The methods are ranked according to the level of coupling between the blocks of the left-hand-side matrix. In all three cases, iterations are performed within a time step to simultaneously converge the solutions of all the equations involved.

In this work we use a monolithic approach with quasi-direct coupling [55, 56] for the solution of the FSI system. The fluid+structure and mesh systems are treated as two separate blocks, and the non linear iterations are carried out one block at a time. In solving a block of equations for the block of unknowns it is associated with, we use the most current values of the other block of unknowns.

The rest of this chapter is organized as follows. First we describe the kinematics of the continuum in the Eulerian, Lagrangian and Arbitrary Eulerian-Lagrangian (ALE) formulations, that are useful to derive the mass and momentum balance equation for liquid and solid. Then, an overview on the most common constitutive models for FSI is presented. The differential equations describing the unsteady and stationary FSI model are derived, and finally, in order to validate our code we perform some well known benchmark available in literature.

1.1 Governing equations

In this chapter we will focus on the kinematics of the continuum, which is the branch of mechanics that studies the motion properties, such as position and velocity. In the theory of the continuum we are not interested to the real microscopic structure of solid objects, instead we only consider objects that are much larger than the mean free path of their particles. Under these premises, in the next paragraphs we introduce the basic principles of the kinematics of the continuum and balance laws with the formalism of [8] and [21].

1.1.1 Kinematics of the continuum

Let $\Omega \subset \mathbb{R}^3$ be a reference configuration of a structure and let Γ_0 be its boundary. Let $\Omega_t \subset \mathbb{R}^3$ be the current configuration of the given structure and let Γ_t be its boundary. Since all the possible reference configurations are equivalent, we can assume that the reference configuration coincides with the

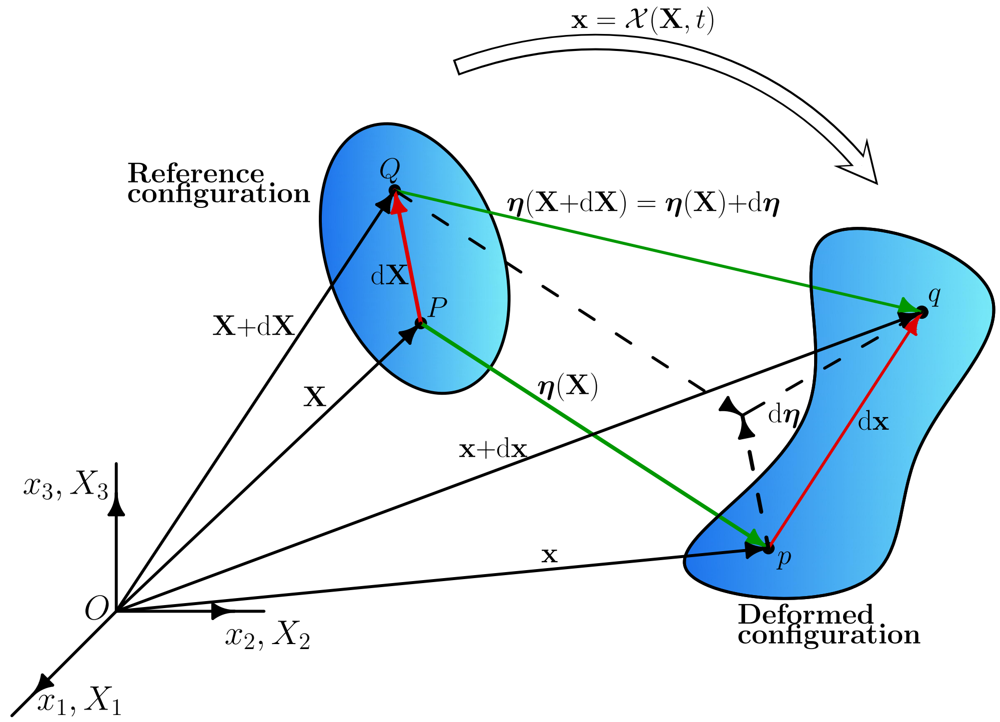

Figure 1.1: Infinitesimal vector $d\mathbf{X}$ in Ω, its deformed version $d\mathbf{x}$ in Ω_t and mapping $\mathcal{X}$.

initial configuration (stress-free) of the structure at time $t = 0$. Let $\mathbf{X}$ be the position of an arbitrary point in the reference configuration and let $\boldsymbol{\eta}$ be the *displacement* of the material point with respect to the initial configuration. We can think of $\boldsymbol{\eta} = \boldsymbol{\eta}(\mathbf{X}, t)$ as a time depending vector field over Ω_t and define a mapping $\mathcal{X}$

$$\mathbf{x} = \mathcal{X}(\mathbf{X}, t) = \mathbf{X} + \boldsymbol{\eta}(\mathbf{X}, t)\,, \tag{1.1}$$

which maps the coordinates of material points in the reference configuration to their counterparts in the current configuration $(\mathbf{x}, t)$. We call the set $(\mathbf{X}, t)$ *Lagrangian coordinates*, named after Joseph Louis Lagrange, or material coordinates, or reference coordinates. The application of these coordinates is called Lagrangian description or reference description. The inverse of the mapping of (1.1) can be written as

$$\mathbf{X} = \mathcal{X}^{-1}(\mathbf{x}, t)\,. \tag{1.2}$$

The set $(\mathbf{x}, t)$ is called *Eulerian coordinates*, named after Leonhard Euler, or space coordinates, and their application is said Eulerian description or spatial description. In the Lagrangian formulation we follow the evolution of a material particle, while in the Eulerian formulation we observe the history of a physical quantity in a given point in the physical space. The Eulerian description is well suited to describe the fluid flow through a fixed spatial region. In this case the fluid particles enter and leave the fixed domain of interest. On the other hand the Lagrangian description is well suited to describe the motion of a body defined as a fixed collection of material particles. The body can change its shape under the action of external and/or internal forces but not its composition. One of the key quantities in deformation analysis is the *deformation gradient* $\mathbf{F} : \Omega \to \mathbb{R}^{3\times 3}$ given by

$$\mathbf{F} = \nabla \mathcal{X}(\mathbf{X}, t) = \frac{\partial \mathbf{x}}{\partial \mathbf{X}}\,, \tag{1.3}$$

and, by substituting (1.1),

$$\mathbf{F} = \mathbf{I} + \frac{\partial \boldsymbol{\eta}}{\partial \mathbf{X}}\,. \tag{1.4}$$

The deformation gradient tensor gives the relationship between a material line $d\mathbf{X}$ before deformation and the line $d\mathbf{x}$ (consisting of the same material as $d\mathbf{X}$) after deformation. Clearly, we can define an inverse deformation gradient $\mathbf{G}$ of the inverse mapping relating Ω to the deformed configuration Ω_t

$$d\mathbf{X} = \mathbf{G} d\mathbf{x}\,. \tag{1.5}$$

Of course, the gradient tensors $\mathbf{F}$ and $\mathbf{G}$ are related by the relations

$$\mathbf{G}(\mathbf{x}, t) = \mathbf{F}^{-1}(\mathbf{X}, t) \qquad \mathbf{F}(\mathbf{X}, t) = \mathbf{G}^{-1}(\mathbf{x}, t)\,, \tag{1.6}$$

where $\mathbf{F}$ is a Lagrangian tensor and $\mathbf{G}$ is an Eulerian tensor. The velocity and acceleration fields of the particle starting at $\mathbf{X}$ in the Lagrangian description, are given by

$$\boldsymbol{v}(\mathbf{X}, t) = \frac{\partial \mathbf{x}}{\partial t}(\mathbf{X}, t)\,, \qquad \mathbf{a}(\mathbf{X}, t) = \frac{\partial^2 \mathbf{x}}{\partial t^2}(\mathbf{X}, t)\,. \tag{1.7}$$

On the other hand, the velocity and acceleration fields in the Eulerian formulation can be written as

$$\boldsymbol{v}(\mathbf{x}, t) = \frac{\partial \mathbf{x}}{\partial t}(\mathcal{X}^{-1}(\mathbf{x}), t)\,, \qquad \mathbf{a}(\mathbf{x}, t) = \frac{\partial^2 \mathbf{x}}{\partial t^2}(\mathcal{X}^{-1}(\mathbf{x}), t)\,. \tag{1.8}$$

The mapping $\mathcal{X}(\mathbf{X}, t)$ has to be invertible and twice continuously differentiable, which implies that cracks and voids do not appear during the deformation. In order to guarantee the local invertibility of the mapping $\mathcal{X}$, the tensor **F** has to be non-singular, which means that

$$J = \det \mathbf{F} \neq 0 \,. \tag{1.9}$$

In order to preserve the orientation the deformation mapping, the determinant J has to be strictly positive everywhere. The deformation is said to be *isochoric* or *volume preserving* if $J = \det \mathbf{F} = 1$ and a material that undergoes only isochoric deformations is *incompressible*. Moreover, J determines the relation between the infinitesimal volumes $d\mathbf{V}$ in the reference configuration and the one $d\mathbf{v}$ in the current configuration

$$d\mathbf{v} = J d\mathbf{V} \,. \tag{1.10}$$

The deformation gradient **F** also expresses the following relation that links the distance between two points, as seen from the reference and current configuration

$$d\mathbf{x} = \mathbf{F} d\mathbf{X} \rightarrow ||d\mathbf{x}|| = \sqrt{d\mathbf{X}^T \mathbf{F}^T \mathbf{F} d\mathbf{X}} \,. \tag{1.11}$$

The difference between the two distances can then be written as

$$||d\mathbf{x}||^2 - ||d\mathbf{X}||^2 = d\mathbf{X}^T \left(\mathbf{F}^T \mathbf{F} - \mathbf{I} \right) d\mathbf{X} = d\mathbf{X}^T 2 \mathbf{E} d\mathbf{X} \,, \tag{1.12}$$

where **E** is the *Green-Lagrange strain tensor*, which by using the (1.4) can be written as

$$\mathbf{E} = \frac{1}{2} \left(\mathbf{F}^T \mathbf{F} - \mathbf{I} \right) = \frac{1}{2} \left(\nabla \boldsymbol{\eta} + \nabla \boldsymbol{\eta}^T + \nabla \boldsymbol{\eta}^T \nabla \boldsymbol{\eta} \right) \,. \tag{1.13}$$

Under the hypothesis of small deformations the last contribution can be neglected, since it involves the dot product between two infinitesimal deformations. Therefore the *small deformation tensor* **D** can be defined as the symmetrical part of the deformation gradient

$$\mathbf{D} = \frac{1}{2} \left(\nabla \boldsymbol{\eta} + \nabla \boldsymbol{\eta}^T \right) \,. \tag{1.14}$$

In the field of continuum mechanics it is common to introduce the so-called *principal invariants* of tensors. The main property of the principal invariants is that they do not change with rotations of the coordinate system. The three principal invariants (I_D, II_D, III_D) of **D** are the coefficients of the characteristic polynomial $p(\lambda)$

$$p(\lambda) = \det(\mathbf{D} - \lambda \mathbf{I}) = \lambda^3 + I_D \lambda^2 - II_D \lambda + III_D = 0 \,, \tag{1.15}$$

and can be computed as functions of the eigenvalues λ_1, λ_2, λ_3 of the matrix $\mathbf{D}$ as

$$I_D = \mathrm{tr}(\mathbf{D}) = \lambda_1 + \lambda_2 + \lambda_3 \,, \tag{1.16}$$

$$II_D = \frac{1}{2}(\mathrm{tr}(\mathbf{D}))^2 - \mathrm{tr}(\mathbf{D}^2) = \lambda_1\lambda_2 + \lambda_2\lambda_3 + \lambda_1\lambda_3 \,, \tag{1.17}$$

$$III_D = \det(\mathbf{D}) = \lambda_1\lambda_2\lambda_3 \,. \tag{1.18}$$

Finally, the *right Cauchy-Green deformation tensor* $\mathbf{C}$ is defined as

$$\mathbf{C} = \mathbf{F}^T\mathbf{F} \,. \tag{1.19}$$

Since in the following paragraphs we will need to compute forces acting on surfaces in both the coordinate system, we now derive some relationships useful for our scope. The relation between infinitesimal surface area elements in the current and reference configurations is known as *Nanson formula*

$$\mathbf{n}ds = J\mathbf{F}^{-T}\mathbf{N}dS \,, \tag{1.20}$$

where we defined $\mathbf{N}dS$ and $\mathbf{n}ds$ as the unit normal vector multiplied by the area element in the reference and deformed configuration, respectively. With $\mathbf{F}^{-T}$ we denoted the transpose of the inverse of the stress tensor $\mathbf{F}^{-T} = (\mathbf{F}^{-1})^T$. Nanson formula (1.20) can be also applied in order to obtain the so-called *Piola identity.* To this aim we use the divergence theorem

$$\int_{\Omega t} \nabla \cdot \psi dv = \int_{\Gamma_t} \psi \cdot \mathbf{n}ds \,. \tag{1.21}$$

By considering $\psi = 1$ identically, the volume integral vanishes and therefore

$$\int_{\Gamma_t} \mathbf{n}ds = \int_{\Gamma_t} J\mathbf{F}^{-T}\mathbf{N}dS = \int_{\Omega_t} \nabla \cdot (J\mathbf{F}^{-T}) = 0 \,, \tag{1.22}$$

which gives the expression of the Piola identity

$$\nabla \cdot (J\mathbf{F}^{-T}) = 0 \,. \tag{1.23}$$

Stress tensors. The Cauchy stress tensor is the most natural and physical measure of the stress measured per unit area of the deformed configuration at a point in the deformed configuration. It is the quantity most commonly used in the Eulerian description of problems in continuum mechanics. However, some other stress measures must be introduced in order to describe continuum mechanics in the Lagrangian formalism. To this aim we first recall that the surface forces $d\mathbf{f}_s$ applied to the Eulerian area element ds can be written in the following form

$$d\mathbf{f}_s = \boldsymbol{\sigma}\mathbf{n}ds\,, \tag{1.24}$$

where $\mathbf{n}$ is the external normal unit vector to the surface delimiting the portion of body and $\boldsymbol{\sigma}$ is the Cauchy stress tensor. In a similar fashion, we introduce a stress tensor $\mathbf{P}$, called the *first Piola-Kirchhoff stress tensor* such that $d\mathbf{f}_s = \mathbf{P}\mathbf{N}dS$. It relates forces in the current configuration to areas in the reference configuration and in general is not symmetric. By using the Nanson formula (1.20) $\mathbf{n}ds = J\mathbf{F}^{-T}\mathbf{N}dS$ we obtain

$$d\mathbf{f}_s = \boldsymbol{\sigma}J\mathbf{F}^{-T}\mathbf{N}dS \Longrightarrow \mathbf{P} = J\boldsymbol{\sigma}\mathbf{F}^{-T}\,. \tag{1.25}$$

The transformation used to obtain the first Piola-Kirchhoff stress tensor from the Cauchy stress tensor is called *Piola transformation*. The Piola transformation $\boldsymbol{\Pi}$ of a second order tensor field $\boldsymbol{\tau} : \Omega \to \mathbb{R}^{3\times 3}$ associated to the mapping $\mathcal{X}$ is the second order tensor field

$$\boldsymbol{\Pi}(\mathbf{X}) = J(\mathbf{X})\boldsymbol{\tau}(\mathcal{X}(\mathbf{X}))\mathbf{F}^{-T}(\mathbf{X})\,, \tag{1.26}$$

for every $\mathbf{X} \in \Omega$.

An important equation gives the relationship between the divergence of a field taken in the two configurations. Let $\boldsymbol{\sigma}$ be a Eulerian tensor field and $\boldsymbol{\Pi}$ its Piola transformation, then we have that

$$\nabla \cdot \boldsymbol{\Pi} = J\nabla \cdot \boldsymbol{\sigma}\,, \tag{1.27}$$

where the divergence terms are taken with respect to the corresponding domain configuration. The proof of the above relation (1.27) uses the Piola identity (1.23) and the chain rule, the full proof can be found in [21]. Sometimes it is useful to introduce another stress tensor in order to relate forces in the reference configuration to areas in the same reference configuration. This is called *second Piola-Kirchhoff stress tensor* $\mathbf{S}$, it is symmetric and defined as

$$\mathbf{S} = \mathbf{F}^{-1}\mathbf{P} = \mathbf{F}^{-1}J\boldsymbol{\sigma}\mathbf{F}^{-T}\,. \tag{1.28}$$

These relations will be useful to transform integrals involving the divergence of a tensor from the current configuration to the reference one and vice versa.

ALE formulation. Until now we have considered only the Eulerian and Lagrangian approaches, however none of them can be applied “as it is” to FSI problems. In fact, the Lagrangian formalism is not suited for the fluid sub-problem, while the Eulerian approach contrasts with our needs of having a fluid mesh that moves following the deformation of the fluid-solid interface. Thus, an intermediate and more general description that combines the advantages of the Eulerian and Lagrangian approaches is introduced. In the *Arbitrary Lagrangian Eulerian* (ALE) description the position of the mesh nodes can either be fixed or changed following a criteria that does not depend on the motion of the material particles. We then use the ALE approach for the fluid sub-problem, while we describe the solid motion with the Lagrangian formalism. In Figure 1.2 a comparison between the Lagrangian, Eulerian and ALE approaches is shown.

We define the following ALE mapping

$$\tilde{\mathcal{A}} : \tilde{\omega} \times \mathbb{R}^+ \to \mathbb{R}^3 \,, \qquad (\tilde{\mathbf{x}}, t) \mapsto \mathbf{x} = \tilde{\mathcal{A}}(\tilde{\mathbf{x}}, t) \,, \tag{1.29}$$

where $\omega(t) = \tilde{\mathcal{A}}(\tilde{\omega}, t)$ for every $t > 0$. Moreover, we define the *ALE mesh velocity* $\tilde{\mathbf{w}}(\tilde{\mathbf{x}}, t)$ as

$$\tilde{\mathbf{w}}(\tilde{\mathbf{x}}, t) = \frac{\partial \tilde{\mathcal{A}}}{\partial t}(\tilde{\mathbf{x}}, t) \,, \qquad \forall \tilde{\mathbf{x}} \in \tilde{\omega} \,. \tag{1.30}$$

The Lagrangian and Eulerian cases can be considered as particular cases of the ALE description. In fact, in the Eulerian formulation the computational domain is fixed ($\omega(t) = \omega(0)$, $\forall t \geq 0$) and the ALE velocity is null $\tilde{\mathbf{w}} = \mathbf{0}$. Vice versa, in the Lagrangian formulation the computational domain moves with the same velocity of the material domain and the ALE and mesh velocities coincide, $\tilde{\mathbf{w}} = \boldsymbol{v}$.

Now, we recall the expressions of the time derivatives of a generic field for the reference, current and ALE configurations. Given a Eulerian field $q(\mathbf{x}, t)$ we define the *Eulerian derivative* as

$$\frac{\partial q}{\partial t}(\mathbf{x}, t) \qquad \forall \mathbf{x} \in \Omega(t) \,, \tag{1.31}$$

which coincides with the standard partial derivative, since the domain is fixed. The time derivative of a Lagrangian field $\tilde{q}(\mathbf{x}, t)$ can be calculated as

$$\frac{D\tilde{q}}{Dt}(\tilde{\mathbf{x}}, t) = \frac{\partial q}{\partial t} + \frac{\partial q}{\partial \mathbf{x}} \cdot \frac{\partial \mathbf{x}}{\partial t} = \frac{\partial q}{\partial t} + \boldsymbol{v} \cdot \nabla q \,, \tag{1.32}$$

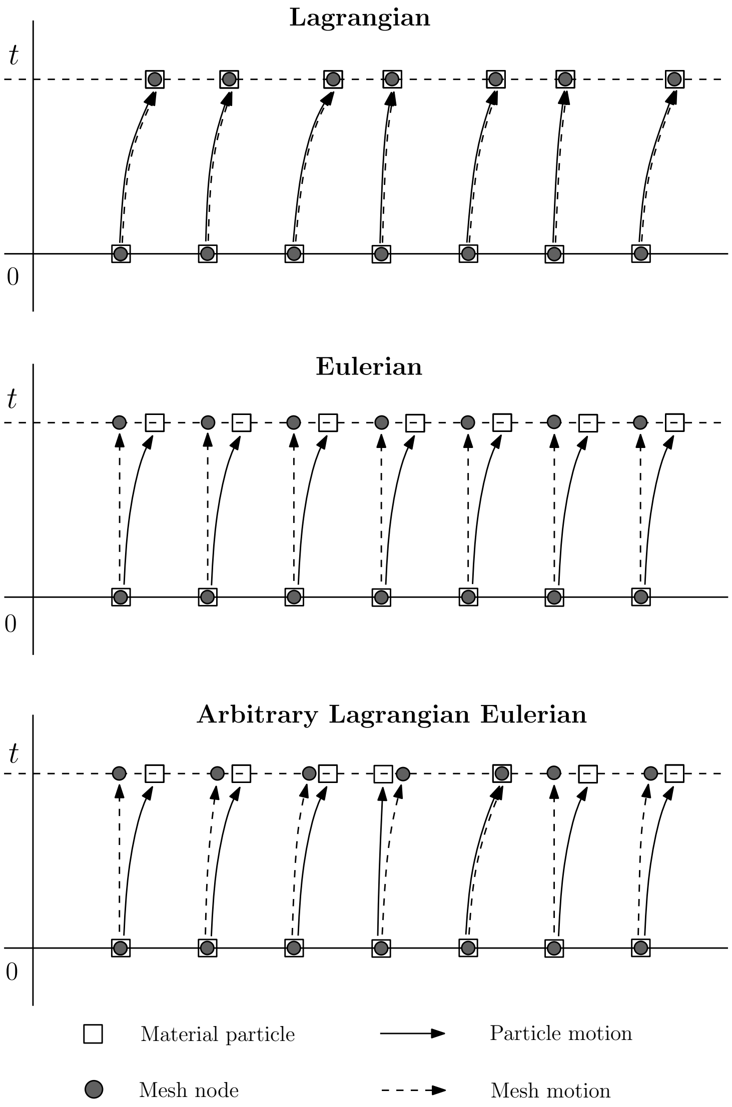

Figure 1.2: Top: 1D Lagrangian description; Middle: 1D Eulerian description; Bottom: 1D ALE (Arbitrary Lagrangian Eulerian) description.

where we applied the chain rule for derivation. The first contribution refers to the time dependence of q, the Eulerian derivative, while the second one takes into account the advection of the field q due to the material velocity $\boldsymbol{v}$. Moreover, the *ALE time derivative* of a Eulerian field reads

$$\left.\frac{\partial q}{\partial t}\right|_{\tilde{\mathcal{A}}} = \frac{d}{dt}\Big(q(\tilde{\mathcal{A}}(\tilde{\mathbf{x}}, t), t)\Big) = \frac{\partial q}{\partial t} + \mathbf{w} \cdot \nabla q \,, \tag{1.33}$$

where the first term is the Eulerian derivative and $\mathbf{w}$ is the Eulerian representation of the computational domain velocity. Here, the second contribution takes into account the advection of the field q due to motion of the mesh.

1.1.2 Conservation laws

We recall that an FSI problem is defined by mean of partial differential equations, the so-called *conservation laws*, that describe the behavior of the fluid and solid. In particular we have balance laws that prescribe the balance of mass, momentum and energy (in the case of non isothermal problems). In order to state the balance laws we first introduce the *Reynolds transport theorem.* Let Ω_t be a material domain, i.e. $\Omega_t = \{\mathbf{x} : \mathbf{x} = \mathcal{X}(\mathbf{X}, t), \mathbf{X} \in \Omega\}$, then

$$\frac{d}{dt} \int_{\Omega_t} \varphi \, d\mathbf{x} = \int_{\Omega_t} \left(\frac{\partial \varphi}{\partial t} + \nabla \cdot (\varphi \boldsymbol{v}) \, d\mathbf{x} \right) . \tag{1.34}$$

The same theorem can be written referring to the ALE formulation, by substituting (1.33) into (1.34). Let $\tilde{\omega}_0 \subset \tilde{\omega}$ an ALE subdomain and $\omega_0(t) = \{\mathbf{x} : \mathbf{x} = \tilde{\mathcal{A}}(\tilde{\mathbf{x}}, t),\ \tilde{\mathbf{x}} \in \tilde{\omega}_0\}$ its image in the ALE mapping, then the following *ALE Reynolds transport formula* holds

$$\frac{d}{dt} \int_{\omega_0(t)} \varphi \, d\mathbf{x} = \int_{\omega_0(t)} \left(\frac{\partial \varphi}{\partial t} + \nabla \cdot (\varphi(\boldsymbol{v} - \mathbf{w})) \, d\mathbf{x} \right) . \tag{1.35}$$

Mass conservation. The first balance equation of the continuum mechanics concerns the mass distribution. Let m be the mass contained in a fixed region $V \subset \mathbb{R}^3$

$$m = \int_V \rho(\mathbf{x}, t) \, d\mathbf{V} \, , \tag{1.36}$$

where $\rho(\mathbf{x}, t)$ is the mass density in the Eulerian description. By applying Reynolds transport theorem to the mass conservation principles we obtain

$$\frac{dm}{dt} = \frac{d}{dt} \int_V \rho(\mathbf{x}, t) = \int_V \left[\frac{\partial \rho}{\partial t} + \nabla \cdot (\rho \boldsymbol{v}) \right] d\mathbf{v} = 0 \, , \tag{1.37}$$

which is the integral form of the mass conservation equation in Eulerian form. If all fields are smooth enough we can write the following local form

$$\frac{\partial \rho}{\partial t} + \nabla \cdot (\rho \boldsymbol{v}) = 0 \, . \tag{1.38}$$

In the case of constant density we recover the *incompressibility* constraint

$$\nabla \cdot \boldsymbol{v} = 0 \, . \tag{1.39}$$

Now we derive the corresponding form of the mass conservation in the Lagrangian formulation. Let $\tilde{V}$ be a fixed set of particles. Therefore, mass conservation reads

$$\frac{dm}{dt} = \frac{d}{dt}\int_{\tilde{V}} \rho \, d\tilde{\mathbf{v}} = \int_{V} \frac{\partial(\rho J)}{\partial t} \, d\mathbf{v} = 0 \,. \tag{1.40}$$

Since V can be chosen arbitrarily we can localize the results to any material point as

$$\frac{\partial}{\partial t}(\rho J) = 0, \qquad \forall t \geq 0 \,. \tag{1.41}$$

This means that the product ρJ does not change in time and is only a function of the material point, namely $\rho J = \rho J(\mathbf{X})$. At $t = 0$ the structure is not deformed and then $J = 1$. Let $\rho_0 = \rho_0(\mathbf{X})$ be the structural mass density in the undeformed configuration, then we recover the following expression of the continuity equation in Lagrangian form

$$\rho_0 = \rho J \,. \tag{1.42}$$

Since ρ_0 is known, by knowing the structural displacement field (i.e. J is known), (1.42) may be used to obtain the density at a material point in the current configuration.

Momentum conservation. The conservation of momentum corresponds with Newton second law of motion applied to a material domain $V(t)$, which states that the resultant of external forces is equal to the rate of change of the total linear momentum of the system. The momentum is given by $\int_{V(t)} \rho \boldsymbol{v} d\mathbf{v}$ and the external forces acting on $V(t)$ can be either volume forces $\mathbf{F}_v$ or surface forces $\mathbf{F}_s$. Therefore momentum conservation can be written as

$$\frac{d}{dt}\int_{V(t)} \rho \boldsymbol{v} d\mathbf{v} = \mathbf{F}_v + \mathbf{F}_s \,. \tag{1.43}$$

The volumetric forces act on the whole domain $V(t)$ and are usually due to external fields, such as gravitational or electromagnetic fields. They can be expressed as the integral over $V(t)$ of a specific force multiplied by the material density

$$\mathbf{F}_v = \int_{V(t)} \rho \mathbf{f}_v \, d\mathbf{v} \,. \tag{1.44}$$

The surface forces $\mathbf{F}_s$ are responsible of the interaction between the material particles contained in $V(t)$ and the exterior through the boundary $\partial V(t)$.

They can be calculated as the surface integral over the boundary $\partial V(t)$ of the Cauchy stress tensor $\boldsymbol{\sigma}$

$$\mathbf{F}_s = \int_{\partial V(t)} \boldsymbol{\sigma}\mathbf{n}\, dS\,. \tag{1.45}$$

By substituting into (1.43) the expressions of the force terms we get

$$\frac{d}{dt}\int_{V(t)} \rho\boldsymbol{v} d\mathbf{v} = \int_{V(t)} \rho\mathbf{f}_v\, d\mathbf{v} + \int_{\partial V(t)} \boldsymbol{\sigma}\mathbf{n}\, dS\,. \tag{1.46}$$

We now use the Reynolds transport formula on the first contribution and the divergence theorem on the term with the Cauchy stress tensor in order to obtain

$$\int_{V(t)} \frac{\partial\rho\boldsymbol{v}}{\partial t}\, d\mathbf{v} + \int_{V(t)} \nabla\cdot(\rho\boldsymbol{v}\boldsymbol{v})\, d\mathbf{v} = \int_{V(t)} \rho\mathbf{f}_v\, d\mathbf{v} + \int_{V(t)} \nabla\cdot\boldsymbol{\sigma}\, d\mathbf{v}\,. \tag{1.47}$$

Since the volume $V(t)$ is arbitrarily chosen we can recover the local formulation of the balance of momentum in Eulerian form

$$\rho\frac{\partial\boldsymbol{v}}{\partial t} + \rho(\boldsymbol{v}\cdot\nabla)\boldsymbol{v} = \rho\mathbf{f}_v + \nabla\cdot\boldsymbol{\sigma} \quad \text{in } \Omega(t),\ t>0\,. \tag{1.48}$$

The Lagrangian formulation of (1.48) can be derived by mapping the integrals back on the undeformed configuration Ω obtaining

$$\frac{d}{dt}\int_{\Omega} \rho J\mathbf{v}\, d\mathbf{v} = \int_{\Omega} \rho J\mathbf{f}_v\, d\mathbf{v} + \int_{\Omega} J\nabla\cdot\boldsymbol{\sigma}\, d\mathbf{v}\,. \tag{1.49}$$

The first term can be rewritten by exploiting (1.41) and (1.42) derived from the mass conservation principle

$$\frac{d}{dt}\int_{\Omega} \rho J\boldsymbol{v}\, d\mathbf{v} = \int_{\Omega} \frac{\partial(\rho J)}{\partial t}\boldsymbol{v}\, d\mathbf{v} + \int_{\Omega} (\rho J)\frac{\partial\boldsymbol{v}}{\partial t}\, d\mathbf{v} = \int_{\Omega} \rho_0\frac{\partial\boldsymbol{v}}{\partial t}\, d\mathbf{v}\,. \tag{1.50}$$

Therefore, by considering the arbitrariness of Ω we have

$$\rho_0\frac{\partial\boldsymbol{v}}{\partial t} = \rho_0\mathbf{f}_v + J\nabla\cdot\boldsymbol{\sigma} \quad \text{in } \Omega,\ t>0\,, \tag{1.51}$$

where the divergence is taken with respect to the deformed coordinates $\mathbf{x}$. By using (1.27) we can transform the divergence term into its Lagrangian form and obtain

$$\rho_0\frac{\partial\boldsymbol{v}}{\partial t} = \rho_0\mathbf{f}_v + \nabla\cdot\mathbf{P} \quad \text{in } \Omega,\ t>0\,, \tag{1.52}$$

where $\mathbf{P} = J\boldsymbol{\sigma}\mathbf{F}^{-T}$ is the first Piola-Kirchhoff stress tensor. Finally, we can write the following momentum balance in the ALE formulation as

$$\rho\frac{\partial\boldsymbol{v}}{\partial t}\bigg|_{\tilde{\mathcal{A}}} + \rho[(\boldsymbol{v}-\mathbf{w})\cdot\nabla]\boldsymbol{v} = \rho\mathbf{f}_v + \nabla\cdot\boldsymbol{\sigma} \quad \text{in } \Omega(t),\ t>0\,. \tag{1.53}$$

1.2 Constitutive models

In the previous sections we have derived the equations for mass and momentum balance, without making any hypothesis on the material. From a mathematical point of view, these equations alone lead to an undetermined system, thus before we can move to the FSI formulation we must take into account some constitutive models for fluid and solid materials. In particular we have to find the relations that link stress to strain and strain to kinematic variables. In the following subsections we will introduce some of the most adopted constitutive equations for fluids and solids.

1.2.1 Newtonian fluids

We now focus on the fluid sub-problem and derive the relation that exists between the Cauchy stress tensor $\boldsymbol{\sigma}$ and the fluid velocity. Newtonian fluids are the simplest mathematical model of fluid that account for viscosity and the viscosity does not depend on the stress state and on the fluid velocity. The stress tensor can be decomposed into an hydrostatic part, which tends to change the volume of the stressed body, and a deviatoric component that is responsible for the fluid distortion rate of deformations as

$$\boldsymbol{\sigma}^f = \boldsymbol{\sigma}^{hyd} + \boldsymbol{\sigma}^{dev} = -p^f \mathbf{I} + \boldsymbol{\tau}\,, \tag{1.54}$$

where the pressure p^f is the Lagrange multiplier associated to the incompressibility constraint (1.39). The pressure can also be written as

$$p^f = -\frac{\mathrm{tr}(\boldsymbol{\sigma})}{3} = \frac{-I_D}{3}\,, \tag{1.55}$$

where I_D is the first invariant of the stress tensor and tr() the trace (i.e. the sum of the diagonal values) of the Cauchy tensor. In the case of a *Newtonian fluid* the deviatoric part $\boldsymbol{\tau}$ is modeled through the following relation

$$\boldsymbol{\tau} = 2\mu^f \mathbf{D} - \frac{2}{3}\mu^f (\nabla \cdot \boldsymbol{v})\mathbf{I} \qquad \tau_{i,j} = 2\mu^f D_{i,j} - \frac{2}{3}\mu^f \frac{\partial u_i}{\partial x_i}\delta_{i,j}\,, \tag{1.56}$$

where $\delta_{i,j}$ is *Kronecker delta* and μ^f the fluid dynamic viscosity. When the fluid is incompressible, by using (1.39) the second term vanishes and thus

$$\boldsymbol{\tau} = 2\mu^f \mathbf{D} \qquad \tau_{i,j} = 2\mu^f D_{i,j}\,. \tag{1.57}$$

The fluid deformation tensor $\mathbf{D}$ can be written as

$$\mathbf{D} = \frac{1}{2}\left(\nabla \boldsymbol{v}^f + (\nabla \boldsymbol{v}^f)^T\right) \qquad D_{i,j} = \frac{1}{2}\left(\frac{\partial v_i}{\partial x_j} + \frac{\partial v_j}{\partial x_i}\right) . \tag{1.58}$$

Therefore, the Cauchy stress tensor for a Newtonian incompressible fluid reads

$$\boldsymbol{\sigma}^f = -p^f \mathbf{I} + \mu^f \left(\nabla \boldsymbol{v}^f + (\nabla \boldsymbol{v}^f)^T\right) . \tag{1.59}$$

This model is suitable for many common liquids and gas, such as water and air, under ordinary conditions. However, many other fluids do not obey the principle of constant viscosity independent of stress, such as colloidal suspensions, blood and synovial fluid. In these cases the viscosity of the non-Newtonian fluid depends on the shear rate or on the shear rate history.

1.2.2 Solid hyperelastic models

In this work we will restrict the presentation only to the class of hyperelastic materials. More complicated cases, such as inelastic materials, may be found in literature, see [53]. The theory of hyperelasticity assumes that the work done by the stress forces in order to deform the solid does not depend on the path followed, but only on the initial and final state. Therefore, a *stored strain energy density function* per unit volume of the undeformed configuration, φ, can be expressed as

$$\varphi = \varphi(\mathbf{F}) . \tag{1.60}$$

Different forms of $\varphi(\mathbf{F})$ lead to different constitutive relationships between stress and strain. The first Piola-Kirchhoff stress tensor $\mathbf{P}$ is obtained by differentiating φ with respect to $\mathbf{F}$ as

$$\mathbf{P}(\mathbf{F}) = \frac{\partial \varphi(\mathbf{F})}{\partial \mathbf{F}} . \tag{1.61}$$

The second Piola-Kirchhoff stress tensor $\mathbf{S}$ can be obtained as a function of the right Cauchy-Green deformation tensor $\mathbf{C}$, remembering that $\mathbf{S} = \mathbf{FP}$ and $\mathbf{C} = \frac{1}{2}(\mathbf{F}\mathbf{F}^{-T} - \mathbf{I})$, or as a function of $\mathbf{E}$ as

$$\mathbf{S} = 2\frac{\partial \varphi(\mathbf{C})}{\partial \mathbf{C}} = \frac{\partial \varphi(\mathbf{E})}{\partial \mathbf{E}} . \tag{1.62}$$

The Cauchy stress tensor $\boldsymbol{\sigma}$ can be computed according to (1.25) or (1.28).

The tensor of elastic moduli is defined as the second derivative of φ with respect to $\mathbf{E}$, namely,

$$\mathbb{C}(\mathbf{E}) = \frac{\partial^2 \varphi(\mathbf{E})}{\partial \mathbf{E} \partial \mathbf{E}} \,. \tag{1.63}$$

The tensor $\mathbb{C}$ is a fourth-rank tensor and, for hyperelastic solids, is independent of the state of deformation. In the most general case the 6×6 components of the elastic tensor differ from each other and all of them have to be determined independently. However, by taking into account symmetry and isotropy the number of different entries can be reduced to only two. Many physically relevant quantities have been introduced to determine the properties of the materials. Among them the *Young modulus*, *Poisson ratio*, *shear modulus*, *bulk modulus* and *Lamé parameters* are mainly used. Young modulus E is a measure of the stiffness of a solid material and is defined as the ratio between stress and strain in a material in the linear elastic regime. Poisson coefficient ν is the negative of the ratio between transverse strain to axial strain

$$\nu = -\frac{d\epsilon_{trans}}{d\epsilon_{axial}} \,. \tag{1.64}$$

For common materials ν is between 0 and 0.5, and almost incompressible materials, such as rubber, have $\nu \to 0.5$, while cork Poisson ratio is close to 0, showing very little lateral expansion when compressed. Bulk modulus k is an indicator of the resistance to compression of a solid and is defined as

$$k = -V \frac{\partial p}{\partial V} \,. \tag{1.65}$$

Finally, other commonly used moduli are the Lamé parameters λ and μ, with the latter also known as shear modulus G in the context of elasticity. Homogeneous isotropic linear elastic materials have their elastic properties uniquely determined by any two moduli among these. Thus, given any two, any other of the elastic moduli can be calculated according to the formulas reported in Table 1.1.

We now aim to obtain the Piola-Kirchhoff and Cauchy stress tensors in the case of incompressible hyperelastic solid. Under these conditions it holds that

$$J = \det \mathbf{F} = III_C = III_b = 1 \,. \tag{1.66}$$

Therefore, in order to ensure the incompressibility constraint of a hyperelastic material the strain energy function can be written as

$$\varphi = \varphi(\mathbf{F}) - p(J-1) \,, \tag{1.67}$$

Table 1.1: Elastic modulus relationships for homogeneous isotropic materials ($R = \sqrt{E^2 + 9\lambda^2 + 2E\lambda}$).

	E	ν	λ	μ
(E, ν)	-	-	$\frac{E\nu}{(1+\nu)(1-2\nu)}$	$\frac{E}{2(1+\nu)}$
(E, λ)	-	$\frac{E-3\lambda+R}{4}$	-	$\frac{2\lambda}{E+\lambda+R}$
(E, μ)	-	$\frac{E}{2\mu} - 1$	$\frac{\mu(E-2\mu)}{3\mu-E}$	-
(ν, λ)	$\frac{\lambda(1+\nu)(1-2\nu)}{\nu}$	-	-	$\frac{\lambda(1-2\nu)}{2\nu}$
(ν, μ)	$2\mu(1+\nu)$	-	$\frac{2\mu\nu}{1-2\nu}$	-
(λ, μ)	$\frac{\mu(3\lambda+2\mu)}{\lambda+\mu}$	$\frac{\lambda}{2(\lambda+\mu)}$	-	-

where the scalar p is the hydrostatic pressure that can be seen as the Lagrangian multiplier that enforces the incompressibility constraint. The first Piola-Kirchhoff tensor can be obtained by substituting (1.67) into (1.61). As a consequence, we need to compute the derivative of $J = \det \mathbf{F}$ with respect to the deformation gradient $\mathbf{F}$. From tensor calculus we have that the derivative of the determinant of a second-order tensor $\mathbf{F}$ is

$$\frac{\partial}{\partial \mathbf{F}} \det(\mathbf{F}) = \det(\mathbf{F})\mathbf{F}^{-T} = J\mathbf{F}^{-T} . \tag{1.68}$$

Thus, the first Piola-Kirchhoff tensor becomes

$$\mathbf{P} = \frac{\partial \varphi}{\partial \mathbf{F}} - pJ\mathbf{F}^{-T} . \tag{1.69}$$

Remembering that $\mathbf{P} = \mathbf{FS}$ we can obtain the second Piola-Kirchhoff tensor as well

$$\mathbf{S} = \mathbf{F}^{-1}\frac{\partial \varphi}{\partial \mathbf{F}} - pJ\mathbf{F}^{-1}\mathbf{F}^{-T} = 2\frac{\partial \varphi}{\partial \mathbf{C}} - \mathbf{F}^{-1}Jp\mathbf{F}^{-T} , \tag{1.70}$$

Finally, the Cauchy stress tensor $\boldsymbol{\sigma}$ is recovered by using the Piola transformation (1.26) with $\boldsymbol{\tau} = p\mathbf{I}$

$$\boldsymbol{\sigma} = -p\mathbf{I} + \boldsymbol{\sigma}^* , \tag{1.71}$$

where $\boldsymbol{\sigma}^*$ can be easily determined once the solid model is chosen.

In the following paragraphs a few models for hyperelastic solids are discussed in terms of strain energy function, range of applicability and known drawbacks.

St. Venant-Kirchhoff. This model is characterized by the following nonlinear formula for the strain energy function

$$\varphi(\mathbf{E}) = \frac{1}{2}\mathbf{E} : \mathbb{C}\mathbf{E}\,, \tag{1.72}$$

that substituted in (1.62) leads to the following linear relationship between the Green–Lagrange strain $\mathbf{E}$ and the second Piola–Kirchhoff stress $\mathbf{S}$

$$\mathbf{S}(\mathbf{E}) = \mathbb{C}\mathbf{E}\,. \tag{1.73}$$

Moreover, in the case of isotropic materials the strain energy function can be rewritten as

$$\varphi(\mathbf{F}) = \lambda(\mathrm{tr}(\mathbf{E}))^2 + 2\mu\,\mathrm{tr}(\mathbf{E}^2)\,, \tag{1.74}$$

where $\mathbf{E}^2 = \mathbf{E} : \mathbf{E}$. Thus the second Piola-Kirchhoff $\mathbf{S}$ becomes

$$\mathbf{S}(\mathbf{E}) = \frac{\partial \varphi(\mathbf{E})}{\partial \mathbf{E}} = \lambda\,\mathrm{tr}(\mathbf{E})\mathbf{I} + 2\mu\mathbf{E}\,. \tag{1.75}$$

This model can be easily adapted to deal with small deformations and incompressible materials. We first substitute $\mathbf{E}$ with the small deformation tensor $\mathbf{D}$. Then the trace of $\mathbf{D}$ coincides with the diverge of the displacement $\boldsymbol{\eta}$ due to the definition of $\mathbf{D}$ in (1.14)

$$\mathrm{tr}(\mathbf{D}) = \frac{\partial \eta_i}{\partial x_i} = \nabla \cdot \boldsymbol{\eta}\,. \tag{1.76}$$

Finally, the Cauchy stress tensor can be written as

$$\boldsymbol{\sigma} = \lambda(\nabla \cdot \boldsymbol{\eta})\mathbf{I} + \mu(\nabla\boldsymbol{\eta} + \nabla\boldsymbol{\eta}^T)\,. \tag{1.77}$$

By comparing this expression with (1.71) we find that the arbitrary solid pressure becomes $p = -\lambda(\nabla \cdot \boldsymbol{\eta})$, where $\lambda \to \infty$ and $(\nabla \cdot \boldsymbol{\eta}) \to 0$.

Since St. Venant-Kirchhoff materials are the simplest among the nonlinear models they are quite used in computational dynamics. However, this model has some disadvantages such as the lack of any term preventing J to approach zero in the stored energy function. This model is therefore mainly adopted when dealing with small strains $\mathbf{E}$.

Neo-Hookean. The Neo-Hookean solid model was first proposed in 1948 by Rivlin in order to improve the St. Venant-Kirchhoff model, see [49]. It is an extension of Hooke law for the case of large deformations and is suitable for plastics and rubber-like substances.

For a Neo-Hookean material, with respect to the current configuration, the strain energy function takes the form

$$\varphi(I_C, J) = \frac{1}{2}\mu(J^{-2/3}I_C - 3) + \frac{1}{2}\left(\lambda + \frac{2}{3}\mu\right)\left(\frac{1}{2}(J^2 - 1) - \ln J\right) . \tag{1.78}$$

The $(J^2 - 1)$ term penalizes the deviation of J from unity and the $\ln J$ term stabilizes the formulation for the regime of strong compression. With this definition of the elastic-energy density, the second Piola–Kirchhoff stress tensor $\mathbf{S}$ may be explicitly computed by using (1.62) and is given by

$$\mathbf{S} = \mu J^{-2/3}\left(\mathbf{I} - \frac{1}{3}I_C\mathbf{C}^{-1}\right) + \frac{1}{2}\left(\lambda + \frac{2}{3}\mu\right)(J^2 - 1)\mathbf{C}^{-1} . \tag{1.79}$$

In the case of incompressible materials the third invariant J is equal to one and then the strain energy function can be written as

$$\varphi(I_C) = \frac{1}{2}\mu(I_C - 3) , \tag{1.80}$$

and the second Piola–Kirchhoff stress tensor as

$$\mathbf{S} = \mu J^{-2/3}\left(\mathbf{I} - \frac{1}{3}I_C\mathbf{C}^{-1}\right) - pJ\mathbf{C}^{-1} . \tag{1.81}$$

The corresponding Cauchy stress tensor can be obtained by using (1.26)

$$\boldsymbol{\sigma} = -p\mathbf{I} + \mu J^{-5/3}(\mathbf{b} - \frac{1}{3}I_b\mathbf{I}) , \tag{1.82}$$

with $I_b = I_C$. Many other hyperelastic models have been proposed, such as Mooney or Mooney-Rivlin materials, and can be found in literature, the interested reader can refer to [45].

1.3 The mathematical model of FSI

In this section we present the mathematical model for a generic fluid-structure interaction problem. We introduce some basic notations for the functional spaces. We use standard notation $H^s(\mathcal{O})$, $s \in \mathbb{R}$ for the Sobolev spaces of order s with respect to the set $\mathcal{O}$, which is either the flow domain Ω, or its boundary Γ, or part of its boundary. Whenever m is a non negative integer, the inner product over $H^m(\mathcal{O})$ is denoted by $(f,g)_m$, where (f,g) denotes the inner product over $H^0(\mathcal{O}) = L^2(\mathcal{O})$. Hence, we associate with $H^m(\mathcal{O})$ its natural norm $||f||_{m,\mathcal{O}} = \sqrt{(f,f)_m}$. For $1 \leq p < \infty$ the Sobolev space $W^{m,p}(\mathcal{O})$ is defined as the closure of $C^\infty(\mathcal{O})$ in the norm

$$||f||^p_{W^{m,p}(\mathcal{O})} = \sum_{|\alpha|<m} \int_{\mathcal{O}} |\left(\frac{\partial}{\partial x}\right)^\alpha f(x)|^p \, dx \, . \tag{1.83}$$

The closure of the space $C_0^\infty(\mathcal{O})$ under the norm $||\cdot||_{W^{m,p}(\mathcal{O})}$ will be denoted by $W_0^{m,p}(\mathcal{O})$. Whenever possible, we will neglect the domain label in the norm. For vector-valued functions and spaces, we use boldface notation. For example, $\mathbf{H}^s(\Omega) = [H^s(\Omega)]^n$ denotes the space of $\mathbb{R}^n$-valued functions such that each component belongs to $H^s(\Omega)$. We denote with $H^s_{\Gamma_d}(\Omega)$ the space of all functions in $H^s(\Omega)$ that vanish on the boundary Γ_d of the bounded open set Ω and with $H^{-s}(\Omega)$ the dual space of $H^s(\Omega)$. The trace space for the functions in $H^1(\Omega)$ is denoted by $H^{1/2}(\Gamma)$. For more information on functional spaces the interested reader can consult [2, 10]. Let us consider a domain $\Omega^t \subset \mathbb{R}^3$ with boundary Γ^t, that consists of a fluid Ω^t_f and a solid part Ω^t_s, so that $\Omega^t = \Omega^t_s \cup \Omega^t_f$ and $\Omega^t_s \cap \Omega^t_f = \emptyset$ at $t \in (0,T]$. The outer boundary $\Gamma^t = \partial\Omega^t$ is then split into the solid boundary $\Gamma^t_s = \Gamma^t \cap \partial\Omega^t_s$ and the fluid one $\Gamma^t_f = \Gamma^t \cap \partial\Omega^t_f$. The surface $\Gamma^t_i = \partial\Omega^t_s \cap \partial\Omega^t_f$ shared between the solid and the fluid is called *fluid-structure interface*. The solid and liquid reference undeformed configurations are denoted with Ω^0_s and Ω^0_f, respectively. Figure 1.3 shows a typical FSI configuration.

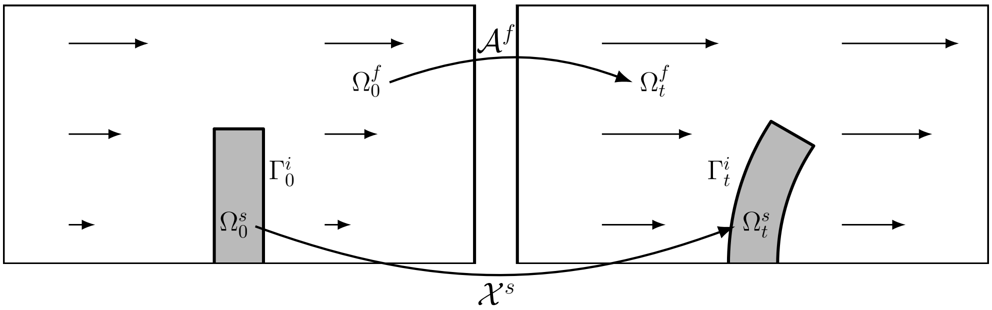

Figure 1.3: Reference and current configuration where a vessel wall interacts with a fluid.

The evolution in time of the solid Ω_s and fluid domain Ω_f are mapped by

$$\mathcal{X}^f : \Omega_0^s \times \mathbb{R}^+ \to \mathbb{R}^3 \, , \tag{1.84}$$

$$\mathcal{A}^f : \Omega_0^f \times \mathbb{R}^+ \to \mathbb{R}^3 \, , \tag{1.85}$$

such that the range of $\mathcal{X}^s(\cdot,t)$ and $\mathcal{A}^f(\cdot,t)$ define Ω_s^t and Ω_f^t, respectively. $\mathcal{X}^s$ maps the coordinates of solid points in the reference configuration to their counterparts in the current configuration through the displacement $\boldsymbol{\eta}^s$

$$\boldsymbol{\eta}^s(t) = \mathcal{X}^s(\mathbf{x}^s,t) - \mathbf{x}_0^s\,. \tag{1.86}$$

The coordinate vector $\mathbf{x}_0$ defines the initial position of the solid domain Ω_0^s. The evolution of the fluid domain Ω_f^t is such that

$$\mathcal{A}^f(\mathbf{x}^f,t) = \mathbf{x}_0^f + \boldsymbol{\eta}^f(\mathbf{x}^f,t)\,, \tag{1.87}$$

where $\boldsymbol{\eta}^f(\mathbf{x}^f,t)$ is defined as an arbitrary extension operator over the fluid domain Ω_t^f and given by

$$\boldsymbol{\eta}^f(\mathbf{x}^f,t) = \mathrm{Ext}(\boldsymbol{\eta}^s|_{\Gamma_i^t}) \quad \text{in} \quad \Omega_0^f\,. \tag{1.88}$$

The extension operator used to evaluate the fluid region displacement is the harmonic or Laplace operator. Other similar operators can be employed as described in [51, 22, 36, 17, 34]. We use the notation $\Omega_s(\boldsymbol{\eta})$ and $\Omega_s(\mathbf{0}) = \Omega_0^s$ for the final and initial domain, respectively. In the following we drop the notation $(\boldsymbol{\eta})$ and $(\mathbf{0})$ over the domain whenever it is not necessary.

The mathematical model of the steady state FSI problem in strong form is defined by the the mass and momentum balance for the fluid and solid (1.39)-(1.51)-(1.53)

$$\nabla\cdot\boldsymbol{v} = 0 \qquad \text{on} \quad \Omega_f\,, \tag{1.89}$$

$$\rho_f(\boldsymbol{v}\cdot\nabla)\boldsymbol{v} - \nabla\cdot\boldsymbol{\sigma}_f = \mathbf{0} \qquad \text{on} \quad \Omega_f\,, \tag{1.90}$$

$$\nabla\cdot\boldsymbol{\sigma}_s(\boldsymbol{\eta}) = \mathbf{0} \qquad \text{on} \quad \Omega_s\,, \tag{1.91}$$

where the derivatives with respect to time have been neglected, the mesh velocity $\mathbf{w}$ is null and no volumetric forces $\mathbf{f}_v$ act on the domain. With ρ_f we denoted the fluid density, $\boldsymbol{\sigma}_f$ is the viscous stress tensor on the fluid and $\boldsymbol{\sigma}_s$ the solid Cauchy stress tensor. The tensors are defined by means of constitutive models. In this work we consider the interaction of an incompressible Newtonian fluid (1.59) with a hyperelastic St. Venant Kirchhoff material (1.77). For the sake's of clarity we report the expressions of the Cauchy stress tensors

$$\boldsymbol{\sigma}_f(p_f,\boldsymbol{v}) := -p_f\mathbf{I} + \mu_f(\nabla\boldsymbol{v} + \nabla\boldsymbol{v}^T)\,, \tag{1.92}$$

$$\boldsymbol{\sigma}_s(\boldsymbol{\eta}) := \lambda_s(\nabla\cdot\boldsymbol{\eta})\mathbf{I} + \mu_s(\nabla\boldsymbol{\eta} + \nabla\boldsymbol{\eta}^T)\,, \tag{1.93}$$

where μ_f is the fluid dynamic viscosity and λ_s and μ_s are the first and second Lamé parameters of the solid. In order to complete the FSI strong formulation we need to provide the following boundary and interface conditions

$$\begin{aligned} \boldsymbol{v} &= \boldsymbol{v}_0 && \text{on } \Gamma_d^f, && \boldsymbol{\eta} = \boldsymbol{\eta}_0 && \text{on } \Gamma_d^s\,, \\ \boldsymbol{\sigma}_f \cdot \mathbf{n}_f &= \mathbf{0} && \text{on } \Gamma_n^f, && \boldsymbol{\sigma}_s \cdot \mathbf{n}_s = \mathbf{0} && \text{on } \Gamma_n^s\,, \\ \boldsymbol{\sigma}_f \cdot \mathbf{n}_f + \boldsymbol{\sigma}_s \cdot \mathbf{n}_s &= \mathbf{0} && \text{on } \Gamma_i, && \boldsymbol{v} = \mathbf{0} && \text{on } \Gamma_i\,, \end{aligned} \tag{1.94}$$

where Γ_d^f and Γ_d^s are the surfaces with Dirichlet boundary conditions for the fluid velocity and solid displacement while on Γ_n^f and Γ_n^s standard homogeneous outflow boundary conditions are imposed. On the interface Γ_i the fluid velocity has to vanish and the normal components of the stress tensors $\boldsymbol{\sigma}$ have to be continuous. We denote with $\mathbf{n}_s$ and $\mathbf{n}_f$ the normal unit vector to the solid and fluid boundary with $\mathbf{n}_s = -\mathbf{n}_f$ on Γ_i. We can write the monolithic FSI system in weak form for the displacement $\boldsymbol{\eta}$ and the velocity field $\boldsymbol{v}$ over $\Omega(\boldsymbol{\eta}) = \Omega_f(\boldsymbol{\eta}) \cup \Omega_s(\boldsymbol{\eta})$, which implicitly incorporates the boundary conditions (1.94) on the common interface Γ_i. The weak or variational problem can be obtained by multiplying (1.89-1.91) with the appropriate test functions $(\psi, \boldsymbol{\phi}) \in L^2(\Omega_f) \times \mathbf{H}^1_{\Gamma_d^s} \cap \mathbf{H}^1_{\Gamma_d^f}(\Omega)$, integrating over the whole computational domain and performing the integration by parts on the terms with $\nabla p \cdot \boldsymbol{\phi}$, $(\nabla \cdot (\mu_f \nabla \boldsymbol{v})) \cdot \boldsymbol{\phi}$, and $(\nabla \cdot (\mu_s \nabla \boldsymbol{\eta} + \lambda_s \mathbf{I} \nabla \cdot \boldsymbol{\eta})) \cdot \boldsymbol{\phi}$ obtaining

$$\int_{\Omega_f} (\nabla \cdot \boldsymbol{v})\, \psi \, d\Omega = 0 \qquad \forall \psi \in L^2(\Omega_f)\,, \tag{1.95}$$

$$\begin{aligned} &\int_{\Omega_f} [(\rho_f (\boldsymbol{v} \cdot \nabla)\boldsymbol{v}) \cdot \boldsymbol{\phi} - p \nabla \cdot \boldsymbol{\phi} + \mu_f \nabla \boldsymbol{v} : \nabla \boldsymbol{\phi}] \; d\Omega + \\ &\quad \int_{\Omega_s} [\lambda_s (\nabla \cdot \boldsymbol{\eta})(\nabla \cdot \boldsymbol{\phi}) + \mu_s \nabla \boldsymbol{\eta} : \nabla \boldsymbol{\phi}] \; d\Omega + \qquad (1.96) \\ &\quad \int_{\Gamma} [\mu_s (\boldsymbol{\nabla} \boldsymbol{\eta} \cdot \mathbf{n}_s) \cdot \boldsymbol{\phi} + \lambda_s (\boldsymbol{\nabla} \cdot \boldsymbol{\eta})(\mathbf{n}_s \cdot \boldsymbol{\phi})]] d\Gamma + \qquad (1.97) \\ &\quad \int_{\Gamma} [[p \mathbf{n}_f - \mu_f (\boldsymbol{\nabla} \boldsymbol{v} \cdot \mathbf{n}_f) \cdot \boldsymbol{\phi}] = 0 \qquad \forall \boldsymbol{\phi} \in \mathbf{H}^1_{\Gamma_d^s}(\Omega) \cap \mathbf{H}^1_{\Gamma_d^f}(\Omega)\,. \end{aligned}$$

The surface integral vanishes due to the boundary and interface conditions (1.94) and this assures that forces at the interface are always computed in an exact way. Finally, the weak form of the FSI system is given by (1.95-1.96).

1.4 Numerical benchmark results

In order to validate our code we perform some well known benchmark available in literature. As first step we consider the Navier-Stokes benchmark [52] proposed by Turek and Schäfer. An evolution of this successful benchmark has been proposed in [57], with the aim of testing different numerical methods and implementations for fluid-structure interaction systems. Since developing and testing an FSI code can be quite a challenging task the authors have split the full problem into smaller and easier partial computational tests. First, only standalone CFD and CSM benchmarks are considered where the fluid solid mutual interaction is neglected. Finally the benchmark results for the complete FSI problem are given. Since the focus of this work is on stationary problems, only the steady benchmark tests are considered and their results are presented in the following sections.

1.4.1 Navier-Stokes benchmark

In this section we describe the domain and the characteristic quantities used in the benchmark [52].

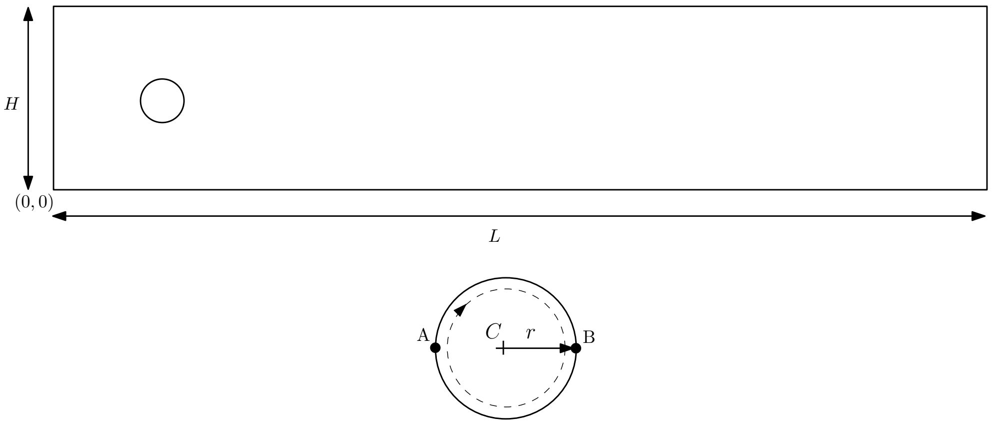

Figure 1.4: Computational domain for Navier-Stokes benchmark.

Domain. Figure 1.4 shows the geometrical properties of the considered domain. The geometry consists of a simple channel of length $L = 2.2m$ and height $H = 0.41m$. A cylinder of radius $r = 0.05m$ and center C is placed into the channel. The dimensions and the coordinates of the reference points A

and B are reported in Table 1.2. We remark that the setting is intentionally non-symmetric. The density of the fluid is given by $\rho = 1 kg\, m^{-3}$ and its viscosity by $\nu_f = 10^{-3} m^2\, s^{-1}$.

Table 1.2: Geometry parameters.

Geometry parameter	Symbol	Value $[m]$
Channel length	L	2.2
Channel width	H	0.41
Cylinder center position	C	(0.2, 0.2)
Cylinder radius	r	0.05
Reference point A	A	(0.15, 0.2)
Reference point B	B	(0.25, 0.2)

Boundary conditions. A parabolic inlet velocity is prescribed on the left side as

$$\boldsymbol{v}(0, y) = \frac{4U_{max} y(H-y)}{H^2}\,, \tag{1.98}$$

where $U_{max} = 0.3 m/s$ is the characteristic velocity and the cylinder diameter $2r = 0.1m$ the reference length. The Reynolds number Re becomes

$$Re = \frac{2\rho U_{avg} r}{\mu} = 20\,, \tag{1.99}$$

since for a parabolic profile the mean value of the inflow velocity is $U_{avg} = \frac{2}{3} U_{max}$. On the right side a homogeneous Neumann boundary condition is imposed, while no-slip conditions are imposed at the other boundaries, including the cylinder surface.

Quantities for comparison. The benchmark parameters are the drag coefficient c_d, the lift coefficient c_l and the pressure drop $\Delta p = p(A) - p(B)$, where A and B are the front and the back of the cylinder, respectively. The forces acting on the submerged bodies are among the quantities of interest for the above-mentioned benchmark tests. Drag and lift coefficients can be easily obtained, once the forces are known, as follows

$$c_d = \frac{2F_x}{\rho L U^2} = \frac{2}{\rho L U^2} \int_S \left(\rho\nu \frac{\partial v_t}{\partial n} n_y - p n_x \right) dS\,, \tag{1.100}$$

$$c_l = -\frac{2F_y}{\rho L U^2} = -\frac{2}{\rho L U^2} \int_S \left(\rho\nu \frac{\partial v_t}{\partial n} n_x + p n_y \right) dS\,, \tag{1.101}$$

where $\mathbf{n} = (n_x, n_y)^T$ is the normal on the surface S and v_t the tangential velocity.

In this work we implemented in our code the method presented in [33] and briefly reported here for clarity. Consider the weak form of the stationary incompressible Navier-Stokes equations

$$\int_\Omega [(\boldsymbol{v} \cdot \nabla \boldsymbol{v}) + \nabla p - \nu \nabla^2 \boldsymbol{v}]\phi \, d\Omega = 0 \qquad \forall \phi \in \mathbf{H}^1(\Omega). \tag{1.102}$$

Consider now an arbitrary test function $\phi_d \in \mathbf{H}^1(\Omega)$ with $(\phi_d)|_S = (1,0)^T$ and $(\phi_d) = (0,0)^T$ on all the other boundaries. After integration by parts the line integrals in (1.100)-(1.101) can be rewritten, obtaining

$$c_d = \frac{2}{\rho L U^2} \int_\Omega \nu \nabla : \nabla \phi_d + (\boldsymbol{v} \cdot \nabla \boldsymbol{v}) \cdot \phi_d - p(\nabla \cdot \phi_d) \, d\Omega \, . \tag{1.103}$$

The following analogous expression can be derived for the lift coefficient considering test functions $\phi_l \in \mathbf{H}^1(\Omega)$ with $(\phi_l)|_S = (0,1)^T$ and $(\phi_l) = (0,0)^T$ on all the other boundaries

$$c_l = \frac{2}{\rho L U^2} \int_\Omega \nu \nabla : \nabla \phi_l + (\boldsymbol{v} \cdot \nabla \boldsymbol{v}) \cdot \phi_l - p(\nabla \cdot \phi_l) \, d\Omega \, . \tag{1.104}$$

By doing so, the line integrals (1.100)-(1.101) on S are replaced by volume integrals on Ω. Furthermore, if we choose ϕ_d and ϕ_l with a small support the number of integrals is reduced to a minimum. Here, the computations are performed only in one layer of cells around the surface S (e.g the cylinder), the shaded mesh cells in Figure 1.5.

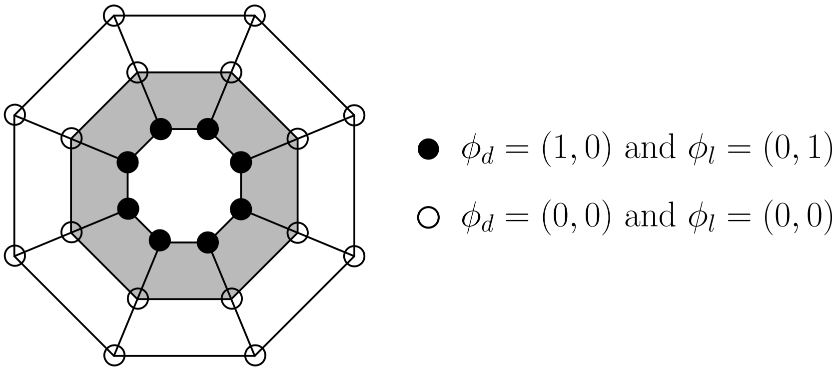

Figure 1.5: Shape functions ϕ_d and ϕ_l for drag and lift computations.

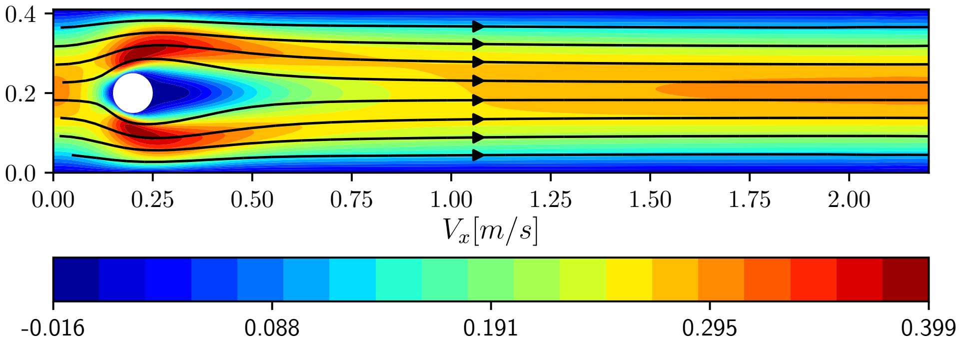

Figure 1.6: Horizontal component of the velocity and streamlines.

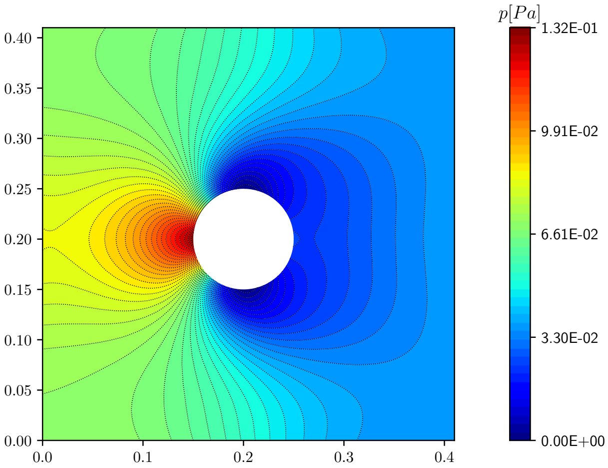

Figure 1.7: Pressure field and isolines near the cylinder.

Table 1.3: Results for the Navier-Stokes benchmark.

Level	Nel	Ndof	Drag	Lift	$\Delta p\ [Pa]$
1	384	3696	5.48815	0.00984	0.12007
2	1056	9884	5.55206	0.01036	0.11792
3	3264	30036	5.57287	0.01053	0.11760
4	14400	130990	5.57797	0.01060	0.11754
Ref			5.57954	0.01062	0.11752

Numerical results. The results of the benchmark computations, obtained with increasing mesh resolution, are summarized in Table 1.3. The reference values have been obtained by high-order spectral method in [42]. Our results are in very good agreement with the reference ones. In Figure 1.6 the velocity field is reported with streamlines, while in Figure 1.7 the pressure profile in the region near the cylinder is shown.

1.4.2 FSI benchmark computational setup

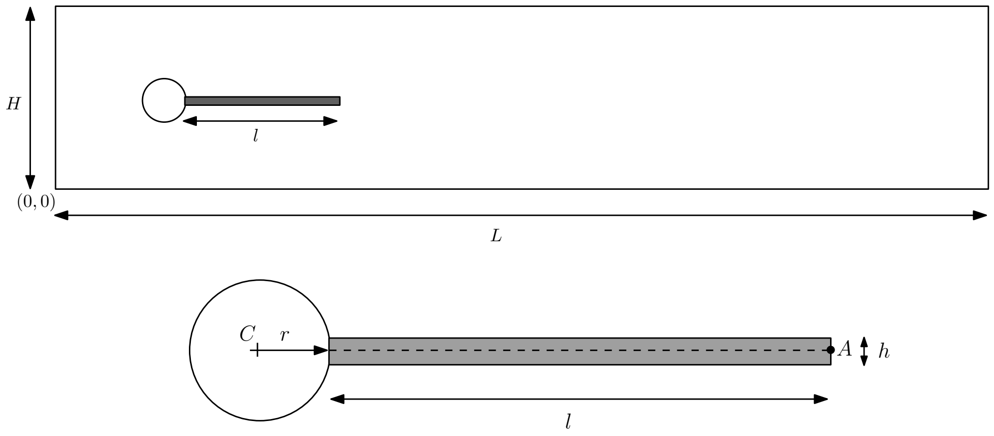

Figure 1.8: Computational domain for FSI benchmark.

In order to test the accuracy of our FSI solver we perform the benchmark proposed in [57]. The fluid is incompressible and Newtonian and interacts with an elastic solid. The equations describing the FSI problem are (1.95-1.96).

Domain. The domain is based on the one used for the Navier-Stokes benchmark and is reported in Figure 1.8. By removing the elastic bar behind the cylinder one can exactly recover the setup of the flow around cylinder configuration. The domain dimensions are: length $L = 2.5m$, height $H = 0.41m$. The circle center is positioned at $C = (0.2, 0.2)m$ and the radius is $r = 0.05m$. The elastic structure bar has length $l = 0.35m$ and height $h = 0.02m$, the right bottom corner is positioned at $(0.6, 0.19)m$ and the left end is fully attached to the fixed cylinder. The control points are $A(t)$, fixed with the structure with $A(0) = (0.6, 0.2)m$ and $B = (0.15, 0.2)m$. The above values are also reported in Table 1.4 for clarity.

Boundary conditions. The boundary conditions for the FSI problems studied are the following

Table 1.4: Geometry parameters for the FSI benchmark.

Geometry parameter	Symbol	Value $[m]$
Channel length	L	2.5
Channel width	H	0.41
Cylinder center position	C	(0.2, 0.2)
Cylinder radius	r	0.05
Elastic structure length	l	0.35
Elastic structure thickness	h	0.02
Reference point A	A	(0.15, 0.2)
Reference point B	B	(0.25, 0.2)

- A parabolic velocity profile is prescribed at the left channel inflow

  $$\boldsymbol{v}(0,y) = \frac{1.5\bar{U}y(H-y)}{(\frac{H}{2})^2} = 1.5\bar{U}\frac{4.0}{0.1681}y(0.41-y)\,, \tag{1.105}$$

  such that the mean inflow velocity is $\bar{U}$ and the maximum of the inflow velocity profile is $1.5\bar{U}$.

- The outflow condition can be chosen by the user, for example stress free or do nothing conditions. The outflow condition effectively prescribes some reference value for the pressure variable p. While this value could be arbitrarily set in the incompressible case, in the case of compressible structure this will have influence on the stress and consequently the deformation of the solid. In this benchmark, the reference pressure at the outflow is set to have zero mean value.

- The no-slip condition is prescribed for the fluid on the other boundary parts.

We would like to point out that the interface conditions are automatically taken into account in our monolithic variational formulation.

1.4.3 CFD partial benchmark

The first test focuses on the fluid dynamics part of the problem, where the flag is taken as a rigid object. The flag is made almost rigid by setting the structural parameters to large values ($\rho_s = 10^6 \frac{kg}{m^3}$, $\mu_s = 10^{12} \frac{kg}{ms^2}$), as

Table 1.5: Results for the Turek CFD benchmark.

Level	Nel	Ndof	Drag (e+01)	Lift
1	1870	17330	1.44023	1.08907
2	9350	68320	1.43366	1.11035
Ref			1.42929	1.11905

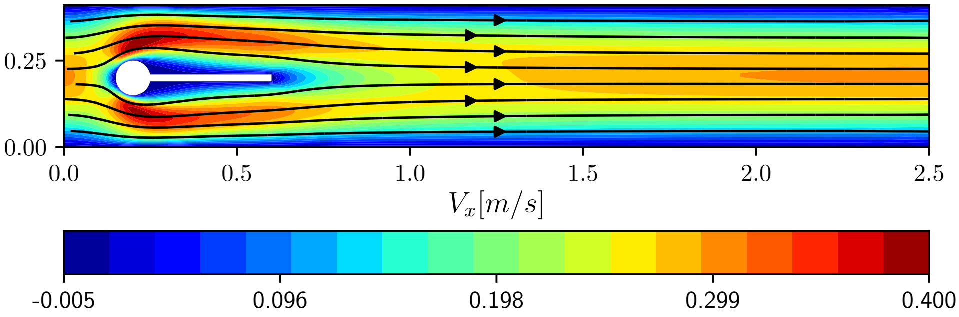

Figure 1.9: Horizontal component of the velocity profile and streamlines.

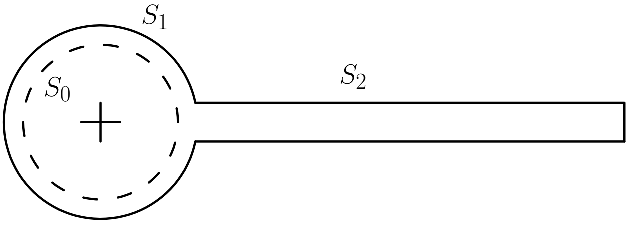

Figure 1.10: Integration path $S = S_1 \cup S_2$ for the drag and lift force calculation.

suggested by the test authors. The fluid parameters are the following

$$\rho_f = 1000\frac{kg}{m^3}\,, \quad \nu_f = 10^{-3}\frac{m^2}{s}\,, \quad \bar{U} = 0.2\frac{m}{s}\,, \quad \mathrm{Re} = \frac{\bar{U}d}{\nu^f} = 20\,.$$

Here the forces exerted by the fluid on the whole submerged body, i.e. lift and drag forces acting on the cylinder and the beam structure together, are among the benchmark quantities for comparison

$$(F_D, F_L) = \int_S \boldsymbol{\sigma}^f \mathbf{n}\, dS = \int_{S_1} \boldsymbol{\sigma}^f \mathbf{n}\, dS + \int_{S_2} \boldsymbol{\sigma}^f \mathbf{n}\, dS\,, \tag{1.106}$$

where $S = S_1 \cup S_2$ denotes the part of the circle being in contact with the fluid (i.e. S_1) plus the part of the boundary of the beam structure which is contact with the fluid (i.e. S_2) and $\mathbf{n}$ is the outer unit normal vector to the integration path that points towards the fluid region, see Figure 1.10. Table 1.5 summarizes the results obtained for this partial computational test, while the velocity profile is reported in Figure 1.9. Our results obtained with two refinement levels show convergence to the reference values, that are obtained with much higher mesh resolutions.

1.4.4 CSM partial benchmark

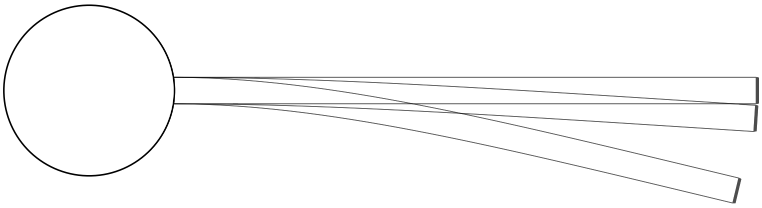

Figure 1.11: Solid deformation for CSM1, CSM2 test benchmark and undeformed configuration.

Table 1.6: Results for the Turek CSM1 benchmark.

Level	Nel	Ndof	Dx(A)(e-03) $[m]$	Dy(A)(e-03) $[m]$
1	1870	17330	-9.4032	-60.9275
Ref			-7.18767	-66.1023

Table 1.7: Results for the Turek CSM2 benchmark.

Level	Nel	Ndof	Dx(A)(e-03) $[m]$	Dy(A)(e-03) $[m]$
1	1870	17330	-0.60587	-16.8514
Ref			-0.469000	-16.9739

The structural tests are computed only for the elastic beam (without the surrounding fluid) adding the gravitational force only on the structural part, $\vec{g} = (0, g)$ $[\frac{m}{s^2}]$. The material properties for the CSM1 test are the following

$$\rho_s = 1000\frac{kg}{m^3}\,, \quad \nu_s = 0.4\,, \quad \mu_s = 0.5 \cdot 10^6\frac{kg}{m\,s^2}\,, \quad \rho_f = 1000\frac{kg}{m^3}\,,$$
$$\nu_f = 10^{-3}\frac{m^2}{s}\,, \quad \bar{U} = 0\frac{m}{s}\,, \quad g = 2\frac{m}{s^2}\,.$$

For CSM2 test the shear modulus μ_s is higher than for CSM1

$$\mu_s = 2 \cdot 10^6 \frac{kg}{m\, s^2} \,,$$

while all the other properties are the same. In Table 1.6 and 1.7 we report the results obtained for the CSM1 and CSM2 tests, respectively. The discrepancy between our results and the reference ones is large for CSM1, where large displacements are involved, since this solid model is accurate only for small displacements. For this reason in the CSM2 case our results are closer to the reference one. In Figure 1.11 the solid displacement profile is reported for both the test configurations together with the undeformed profile.

1.4.5 FSI full benchmark

Table 1.8: Parameter setting for the FSI1 benchmark.

Parameter	Symbol	Measure unit	Value
Solid density	ρ_s	$[10^3 \frac{kg}{m^3}]$	1
Poisson coefficient	ν_s	-	0.4
Shear modulus	μ_s	$[10^6 \frac{kg}{ms^2}]$	0.5
Fluid density	ρ_f	$[10^3 \frac{kg}{m^3}]$	1
Fluid viscosity	ν_f	$[10^{-3} \frac{m^2}{s}]$	1
Density ratio	β	-	1
Dimensionless shear modulus	Ae	-	3.5×10^4
Average inlet velocity	$\bar{U}$	$[\frac{m}{s}]$	0.2
Reynolds number	Re	-	20

Table 1.9: Results for the Turek FSI1 benchmark.

Level	Nel	Ndof	Dx(A)(e-05) $[m]$	Dy(A)(e-04) $[m]$	Drag	Lift
1	1870	17330	2.15828	8.34873	14.4034	0.750155
2	9350	68320	2.16161	8.28078	14.3377	0.757567
3	39270	271280	2.16367	8.23453	14.3074	0.761073
Ref			2.27049	8.20877	14.2943	0.763746

Finally, the mutual interaction between solid and fluid, which is the core of FSI, is taken into account with the stationary FSI1 test. The parameter

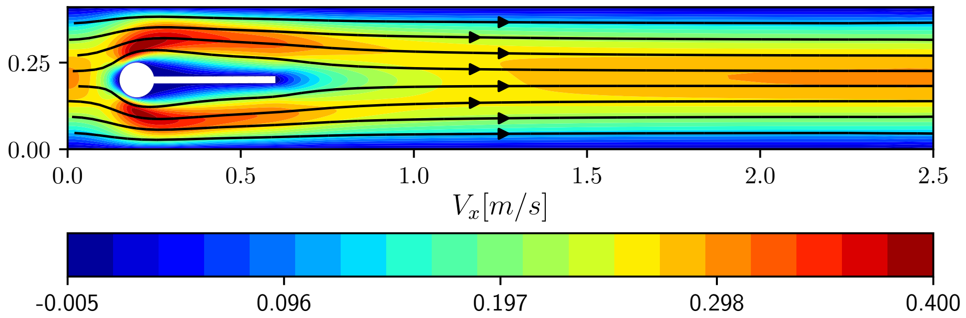

Figure 1.12: Horizontal component of the velocity profile and streamlines.

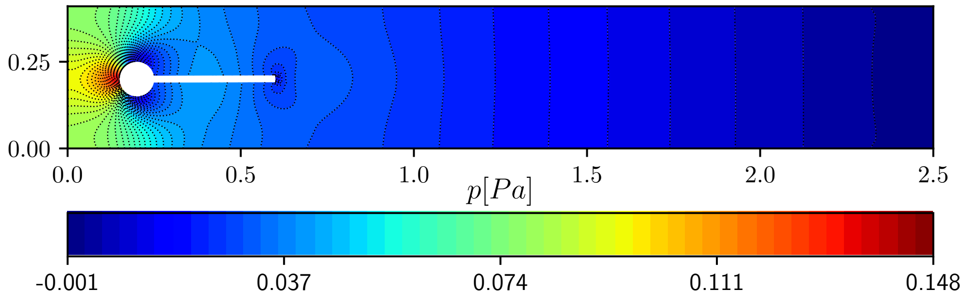

Figure 1.13: Pressure profile in the fluid.

values for this test are given in Table 1.8. The velocity profile and the pressure distribution in the fluid are reported in Figures 1.12 and 1.13, respectively. In Table 1.9 the results obtained with different spatial resolution are reported and compared with the reference values. The results converge to the values given by the benchmark authors, when the mesh resolution is increased.

CHAPTER 2

Optimal FSI control

In the field of computational fluid dynamics (CFD) there is a growing interest towards optimization and nowadays the computational power available allows researchers to study systems that were out of reach just few decades ago. There is a wide literature on optimization processes, which can be based on many different approaches, such as linear feedback methods, adjoint or sensitivities-based optimal control, multi-objective optimization and many others. The interested reader can consult [18, 43, 37, 44, 30, 50, 35] and references therein. Linear feedback methods are commonly employed to operate complex systems like turbine valves-heat exchanger in power plants and are used in electronic applications in the railway or automotive industries [46, 29]. Multi-objective optimization and sensitivities-based optimal control are other interesting research fields that find applications ranging from engineering design to financial predictions of market shares.

In this work we refer to adjoint based methods, which have been proven to be a good approach for the optimal control of complex problems, in which computational fluid dynamics simulations can be performed on the system of interest [59]. Moreover, these methods have a solid mathematical background and the existence of local optimal solutions can be proven for many interesting cases [28]. However, this method is only appropriate when the design variables are continuous. For design variables which can take only integer values (e.g. the number of engines on an aircraft) stochastic procedures such as simulated annealing and genetic algorithms are more suitable, anyway this kind of variables are not common in the field of CFD optimization. Moreover, if the objective function contains multiple minima, then the gradient approach will generally converge to the nearest one without searching for other minima elsewhere in the design space. If the objective function is known to have multiple local minima, and possibly discontinuities, then again a stochastic search method may be more appropriate. The adjoint based method, can then be used only to get improvements from a reference state and not to find the global optimal solution to the problem, unless this is the only minimum of the functional. However, in many practical situations an improvement on a reference state is what is needed because too big changes on the design cannot be performed for physical or practical reasons. In these cases this method could prove useful for the optimal design of engineering devices.

Although the literature is quite heterogeneous, most of it can be classified according to some peculiarities. In *stationary* problems the system variables do not depend on time, while in *unsteady* problems the studied system is optimized during its evolution in time. Another classification can be made between different approaches to control, such as *distributed*, *boundary* and *shape* controls. The difference between them lies in the way the control can act on the problem domain. In the first one, source terms in the interior part of the domain are used as control parameter. This kind of control is not often suitable for practical applications due to technical difficulties or physical limits. However, from a theoretical point of view it can be applied to any problem and the numerical implementation is usually straightforward. The boundary control, where one acts on the system through its external surface, can be considered as a more realistic approach to optimization. However, one has to pay the price of a much more challenging mathematical framework and numerical algorithm implementation. The last one we mention is the shape control, where the controlled parameter is the shape of the domain boundary, as in the case of leading or trailing edge flaps, see [31, 25]. Furthermore, identification of material properties such as Young modulus in solids or fluid viscosity is an inverse problem that can be studied with the adjoint based formalism, see [47].

In the following sections the basic principles of the adjoint optimal control theory are presented. Then we derive the optimality system for a simple example problem. Finally, we introduce the algorithm used for the solution of the optimal control of fluid-structure interaction systems.

2.1 Introduction to adjoint optimal control

In many engineering fields a key process is trying to improve already available devices or creating new ones with enhanced properties. Improving the performances of a machinery in order to use less resources or to increase the productivity or finding a better shape to reduce the air resistance are common examples. The first necessary step when optimizing consists of identifying an *objective*, a quantitative indicator of the performance of the studied system. It may be velocity, time, profit, fuel consumption or any other quantity of interest, provided that it can be quantified in numbers. Clearly, in order to reach the objectives one or more *control parameters* or *variables* have to be changed inside feasible limits. Often these parameters can not be chosen arbitrarily, but have to be restricted, or *constrained*, to a certain range of values. For example, if the temperature is the control variable then it has to be restricted to non negative values. Once the optimal control problem has been set up, an optimization algorithm can be used in order to find the desired solution. This is usually done numerically with the help of a computer or even supercomputers for larger systems.

We now focus on a simple example of an adjoint optimal control problem, useful to introduce and clarify the main aspects of the method. To set up the problem we first need to choose the goal to reach and how we intend to do so. We introduce a *cost functional*, a mathematical formulation that measures how far from the desired target the studied system is. This is usually expressed in terms of the state system variables. Let us consider the case where we want to heat a metal bar in such a way that its temperature distribution matches a given profile. This cost functional $\mathcal{J}$ becomes

$$\mathcal{J}(T) = \frac{1}{2}\int_{\Omega} \omega (T - T_d)^2 \, d\Omega \,, \tag{2.1}$$

where Ω represents the domain of the metal bar and T_d is the target temperature, which can depend on the coordinates or can have a uniform value in the whole domain. This cost functional measures the distance in norm between the metal bar temperature and the target one. We may also be interested not to the whole domain but only to a subdomain of Ω, so we introduce the parameter ω, which is a function of the space. The dependence on the time is not considered here, otherwise the integration in (2.1) should be performed also in time, hugely increasing the complexity of the problem. For time-dependent problems see for example [30]. The partial differential equation (PDE) that models the behavior of the metal bar is the following Poisson equation

$$\nabla \cdot (k \nabla T) + q = 0 \qquad \forall x \in \Omega \,, \tag{2.2}$$

where k is the thermal conductivity of the material and the volumetric heat source q is our distributed control parameter. The solution of the Poisson equation can be found after prescribing the boundary conditions

$$\nabla T \cdot \mathbf{n} = 0 \qquad \text{on } \Gamma_n \,, \tag{2.3}$$

$$T = T_0 \qquad \text{on } \Gamma_d \,, \tag{2.4}$$

where Γ_d are the surfaces with Dirichlet boundary conditions for the temperature, while on Γ_n standard homogeneous Neumann boundary conditions are imposed. In a finite element framework we are interested in the weak formulation of the state system (2.2). We consider test functions ϕ defined in the appropriate functional space V_d

$$\phi \in V_d = \big(\phi \in H^1(\Omega) : \phi = 0 \text{ on } \Gamma_d \big) \,. \tag{2.5}$$

The weak formulation is obtained in the standard way, after integrating by parts the Laplacian term in (2.2) and applying the boundary conditions we recover

$$\int_\Omega -(k \nabla T) \phi \, d\Omega + \int_\Omega q \phi \, d\Omega = 0 \qquad \forall \phi \in V_d \,, \tag{2.6}$$

and in the following we will refer to (2.6) as *state system*. Now we can state the optimal control problem as

Problem. *Find an optimal control q and an optimal state T such that the functional $\mathcal{J}(T)$ given in (2.1) is minimized and the state system (2.6) is satisfied.*

It is worth noticing that the state system behaves as a constraint for the optimization problem, since it limits the possible solutions to a subset of the solution space. Moreover, in many circumstances the control parameter has to be limited somehow to avoid unbounded solutions, with infinite values of the control in some part of the domain. There are mainly two approaches to do so. We can limit the value of the admissible control with an additional constraint, so that it is bounded

$$q < q_{max} \,, \tag{2.7}$$

or we can penalize the objective functional by adding a regularization term to (2.1). Adding this regularization has the effect of forcing better mathematical and numerical properties to the optimization process. This term can be the classic Tychonov term containing the L^2-norm of the control q, penalized with a parameter β

$$\mathcal{J}(T,q) = \frac{1}{2}\int_\Omega \omega(T-T_d)^2\, d\Omega + \frac{\beta}{2}\int_\Omega q^2\, d\Omega\,. \tag{2.8}$$

The value of the parameter β is used to balance the relative importance of the two terms in (2.8). For example, if we choose too high values of β then the control range is limited and the optimization algorithm cannot improve the reference solution efficiently. Under certain circumstances, for example when studying boundary controls, one may wish to impose further requirements on the regularity of the controls, i.e. H^1 controls, so other regularization terms have to be added to the cost functional.

2.2 Optimality system

The above-mentioned problem is an example of constrained optimization problems. Such class of problems may be reformulated as *unconstrained* optimization problems through the Lagrange multiplier method. However we remark that this technique can find only *local* stationary points (maxima or minima) of a functional subject to equality constraints. We recall that a local minimum (T^*, q^*) for the functional of interest is a point such that, for some $\epsilon > 0$

$$\mathcal{J}(T^*,q^*) \leqslant \mathcal{J}(T,q) \quad \forall (T,q) \in \mathcal{T}\times\mathcal{Q} \quad \text{and} \quad ||T^*-T|| < \epsilon\,. \tag{2.9}$$

We now apply the Lagrangian multiplier method to the example of distributed control described in the previous section. The following Lagrangian functional (or augmented functional) is obtained by adding to the objective functional the constraint multiplied by the Lagrangian multiplier ϕ as

$$\mathcal{L}(T,q,\phi) = \mathcal{J}(T,q) + \phi\int_\Omega [\nabla\cdot(k\nabla T) + q]\, d\Omega\,, \tag{2.10}$$

$$\mathcal{L}(T,q,\phi) = \frac{1}{2}\int_\Omega \omega(T-T_d)^2\, d\Omega + \frac{\beta}{2}\int_\Omega q^2\, d\Omega + \int_\Omega [\nabla\cdot(k\nabla T) + q]\phi\, d\Omega\,. \tag{2.11}$$

In the framework of optimal control theory the Lagrange multipliers are interpreted as adjoint variables or *costate*.

By imposing the first order necessary conditions we recover the stationary points of the Lagrangian and the optimality system. We set to zero the Fréchet derivatives taken with respect to all the problem variables T, q and ϕ. The Fréchet derivative used in infinite dimensional spaces differs from the ordinary derivative since its value depends on the arbitrary variation δT

$$\frac{\delta \mathcal{L}}{\delta T} = \lim_{\epsilon \to 0} \frac{\mathcal{L}(T + \epsilon \delta T, q, \phi) - \mathcal{L}(T, q, \phi)}{\epsilon} \,. \tag{2.12}$$

By setting to zero the derivative taken with respect to T we get

$$\frac{\delta \mathcal{L}}{\delta T} = \int_\Omega (T - T_d)\delta T \, d\Omega - \int_\Omega k\nabla\phi \cdot \nabla\delta T \, d\Omega + \int_\Gamma k\nabla\delta T \cdot \mathbf{n}\phi \, d\Gamma = 0 \qquad \forall \delta T \in H^1(\Omega)\,, \tag{2.13}$$

that is the equation for the Lagrangian multiplier ϕ. When a Dirichlet boundary condition is imposed the temperature is fixed and therefore we can assume $\delta T = 0$, since δT is the variation of the temperature T. The appropriate functional space for δT is then $V_d(\Omega) \subset H^1(\Omega)$. Moreover, by taking the variations of (2.3), we get $\nabla\delta T \cdot \mathbf{n} = 0$ on Γ_n, so the surface integral over Γ in (2.13) has to be computed only on the subset Γ_d where Dirichlet boundary conditions are prescribed.

In order to recover the strong form of the adjoint system together with the dual boundary conditions we integrate by parts and obtain

$$\begin{split} \int_\Omega (T - T_d)\delta T \, d\Omega + \int_\Omega \nabla \cdot (k\nabla\phi)\delta T \, d\Omega - \int_{\Gamma_n} k\nabla\phi \cdot \mathbf{n}\delta T \, d\Gamma \\ + \int_{\Gamma_d} k\nabla\delta T \cdot \mathbf{n}\phi \, d\Gamma = 0 \qquad \forall \delta T \in V_d(\Omega)\,. \end{split} \tag{2.14}$$

The dual boundary conditions can be recovered by imposing that the surface integrals in (2.14) must vanish. So, on Γ_n the gradient of ϕ along the normal component is zero and on Γ_d the value of ϕ is zero. The boundary value problem in strong form reads

$$\nabla \cdot (k\nabla\phi) + (T - T_d) = 0 \qquad \forall x \in \Omega\,, \tag{2.15}$$

$$k\nabla\phi \cdot \mathbf{n} = 0 \qquad \text{on} \quad \Gamma_n\,, \tag{2.16}$$

$$\phi = 0 \qquad \text{on} \quad \Gamma_d\,, \tag{2.17}$$

since the variations δT can be chosen arbitrarily. It is worth noticing that the adjoint variable ϕ in (2.15-2.17) satisfies a similar heat transfer equation with the same thermal conductivity of the state temperature in (2.2-2.4) and with a source term proportional to the difference between the temperature and the desired one. Moreover the boundary conditions of the adjoint system are of the same type as in the state problem but they should be assumed homogeneous. This is a typical feature of adjoint problems: when a Dirichlet b.c. is imposed in the state system an homogeneous Dirichlet b.c. must be imposed in the adjoint system. At the same time in the regions where a Neumann b.c. is used, the adjoint system has an homogeneous Neumann b.c..

When considering the variations δq we obtain

$$\frac{\delta \mathcal{L}}{\delta q} = \int_\Omega (\beta q + \phi) \delta q \, d\Omega = 0 \qquad \forall \delta q \in H^1(\Omega) \, , \tag{2.18}$$

which, since the variations δq are arbitrary, becomes a simple algebraic equations for the control q as

$$q = -\frac{\phi}{\beta} \, . \tag{2.19}$$

Finally, when we derive with respect to the Lagrangian multiplier ϕ, we get

$$\frac{\delta \mathcal{L}}{\delta \phi} = \int_\Omega [\nabla \cdot (k \nabla T) + q] \delta \phi \, d\Omega = 0 \qquad \forall \delta \phi \in H^1(\Omega) \, . \tag{2.20}$$

This is the weak form, see (2.2), of the state system. The equations (2.13-2.18-2.20) form the so called *optimality system* and allow to find the stationary point of the Lagrangian functional.

2.2.1 Numerical solution of the optimality system

In order to solve the obtained optimality system, a first possible strategy is solving in a fully coupled fashion, with a *one shot* method. By doing so, for this simple example the system is solved in a fast and reliable way without any optimization algorithm. However, for complex systems the optimality system is made of many nonlinear and strongly coupled equations and the solution becomes too expensive when a fine domain discretization is used. In order to overcome these challenges a *segregated* approach is generally a better alternative. In this approach the equations forming the optimality system are solved independently with appropriate algorithms, known as *optimization* *algorithms*, that reduce the computational expense. In fact, for most practical applications it is far more convenient to solve the non linear state system several times with a segregated approach, than it is to solve the non linear coupled optimality system once with a one shot method.

All these algorithms require the choice of a starting point x_0. When the starting point is a reasonable estimate of the solution, then the algorithms are expected to perform better, i.e, to find the optimal solution faster. Beginning at x_0, a sequence of solutions $\{x_k\}_{k=0}^{\infty}$ is found and the algorithm ends when either no more progress is obtained or a certain convergence criteria is satisfied.

Many different algorithms have been proposed in literature and among them one can distinguish between two main classes, that differ in the way the update solutions are found from the previous ones, *trust region* and *line search*. Both of them require a search direction and a step size, which evaluate the distance from the current solution. In trust region approaches the new iterate is searched in a region around the current solution, the maximum distance between two consecutive iterates is fixed by a step size and the algorithm aims to find the optimal direction. Line search methods are in some sense dual to trust region ones: the step direction is found first and then the step size is chosen in order to minimize the functional along that direction.

In this work we use a gradient based line search approach with a simple Armijo backtracking strategy. The search direction is obtained by solving the adjoint and control equations that give the objective functional gradient direction. A generic iteration of a line search method for the minimization of a functional $\mathcal{J}$ is given by

$$x_{k+1} = x_k + \alpha_k p_k \,, \tag{2.21}$$

where α_k is the step length and p_k is the search direction. In order to guarantee that the the functional is reduced along the search direction it is fundamental that p_k is a descent direction, therefore it usually has the form

$$p_k = -B_k^{-1} \nabla \mathcal{J}_k \,, \tag{2.22}$$

where B_k is a symmetric, non-singular, positive definite matrix. When B_k is the identity matrix the method is known as *steepest descent* and the direction is simply given by the functional gradient. In Newton methods B_k is the exact Hessian matrix of the functional $\nabla^2 \mathcal{J}_k$, while in quasi-Newton methods B_k

approximates the Hessian at every iteration with a low-rank formula, such as *BFGS* [11].

Algorithm 1 Backtracking Line search

```
1. Set $\alpha_k = \alpha^0 > 0$, $\rho \in (0,1)$
while $\mathcal{J}_k(x_k + \alpha_k p_k) > \mathcal{J}_k(x_k)$ do
    2. Set $\alpha_k = \rho\,\alpha_k$
    if $\alpha_k < toll$ then
        Line search not successful                ▷ End of the algorithm
    end if
end while
```

We now focus our attention to the choice of the step length parameter α_k. The main trade-off we have to face is that we would like to find an α_k such that the functional $\mathcal{J}_k$ is significantly reduced, with as less computational effort as possible. An *exact line search* aims to find the value of α_k that minimizes the functional $\mathcal{J}_k$ along the search direction, but in general identifying this value is too expensive. For this reason more feasible strategies perform only an *inexact line search*, reducing $\mathcal{J}_k$ at minimal cost. The *backtracking* line search strategy presented in Algorithm 1 is a commonly used inexact method. The step length α_k is first initialized to a positive value α^0, whose value depends on the choice of the algorithm. Then the step length is reduced by a contraction factor ρ until we obtain a lower functional for the new iterate. The process may also come to an end if α_k becomes lower than a tolerance value *toll*.

Functional sensitivity. Functional sensitivity to the controls or design parameters is an important issue in flow control and deserves a brief discussion. Continuous dependence on data means that a small change in the data, leads to small changes in the solution, i.e., the solution is largely insensitive to the data. This is exactly what one does not want for control and optimization problems. Instead, what one wants is to have at disposal control or design parameters such that small changes in their values effect large changes in the solution; the solution should be very sensitive to small changes in the data. Achieving the goals of optimization is made much easier when the flow is very sensitive to changes in the controls or design parameters. So, in trying to effect control or optimization, one should look for controls or design parameters that have a major effect on the flow and ignore those that do not. Consider for instance a problem where the goal of optimization is to make a given objective functional as small as possible. If the cost functional is not sensitive with respect to a design parameter it means that we can eliminate that parameter from the problem since it is useless for meeting our objective. As an example, it is known that the flow in a channel will develop into the parabolic profile of Poiseuille flow regardless of the inflow condition; the lower the value of the Reynolds number, the quicker the parabolic profile will develop. The flow far away downstream is insensitive, especially for low values of the Reynolds numbers, to the inflow profile one imposes. Thus, insensitivities of the cost functional can be used to induce changes in the choice of design parameters by replacing the useless parameters with others that have a greater effect on the cost functional, or change the cost functional itself so that it becomes more sensitive to the design parameters. These will result in more efficient use of the optimizer, with fewer iterations, and/or better results, with lower functional values or better design parameter values.

2.3 Optimal control of FSI

Algorithm 2 Description of the Steepest Descent algorithm for FSI.

```
1. Set a state $(\boldsymbol{v}^0, p^0, \boldsymbol{\eta}^0)$ satisfying FSI state system    ▷ Setup of the state
2. Compute the functional $\mathcal{J}^0$
3. Set $r^0 = 1$
for $i = 1 \to i_{max}$ do
    4. Solve the adjoint system to obtain the adjoint state $(\boldsymbol{v}_a^i, p_a^i)$
    5. Set the control update with the adjoint variables
    6. Set $r^i = r^0$
    while $\mathcal{J}^i > \mathcal{J}^{i-1}$ do    ▷ Line search
        7. Set $r^i = \rho\, r^i$
        8. Solve FSI state system for $(\boldsymbol{v}^i, p^i, \boldsymbol{\eta}^i)$ with updated control and $r^i$
        if $r^i < toll$ then
            Line search not successful    ▷ End of the algorithm
        end if
    end while
end for
```

In this section we apply the adjoint optimal control theory to a general fluid-structure interaction problem. The system of equation that models our

FSI problem has been reported in Section 1.1. In all the steady cases found in literature the optimality system comes directly from the steady FSI equations. The time is not present and the nonlinear algorithm to define the final deformation is implicitly determined. The balance between the adjoint displacement, the adjoint velocity and the final deformed interface must be recovered after many nonlinear iterations. Moreover, the numerical algorithm cannot be constructed in a very straightforward way. Differently from these approaches, with our method, we desire to recover the symmetry of the state-adjoint system that is characteristic of the time dependent problem where the final deformation is obtained step by step. By doing so the adjoint interface forces are balanced automatically. In order to do this we introduce an auxiliary displacement field and use it to extend the velocity field to the structure domain. This is a steady optimization problem where the physical velocity in the solid is zero while the fictitious velocity is used as the driving force for the solid motion during the optimization process. In the following Chapters we apply a new optimization algorithm to few stationary FSI problem, where both the state and adjoint systems are written in a symmetric monolithic form. There are several motivations behind this approach. First, the coupling conditions at the fluid-solid interface are automatically taken into account in the monolithic variational formulation and no sub-iterations are necessary as in the case of partitioned approaches. Furthermore, since in the framework of FSI gradient-based optimization the solution of the adjoint system is used to determine the gradient of the functional, then it is important to solve with a stable and robust method that treats accurately the propagation of the information across the interface. Finally, with our approach, we can use the same solver for both the state and adjoint systems with minor modifications.

Here, in order to provide a general description of the method, we do not consider a specific objective functional for the minimization problem. However, many choices can be made for example considering solid displacement or fluid velocity profile matching, solid stress state or drag minimization. After the choice of the functional of interest the full Lagrangian functional can be introduced. By imposing vanishing Fréchet derivatives of the Lagrangian functional we obtain the weak form of the FSI state system (1.95-1.96), the adjoint FSI system and the optimality condition. The adjoint system and the optimality system are usually linear in their own unknowns, which depend on the choice of the objective functional. The unknowns of the optimality system are then $(\boldsymbol{v}, p, \boldsymbol{v}_a, p_a, \boldsymbol{\eta}, \boldsymbol{\eta}_a)$ and are strongly coupled in the system. For this reasons a one-shot approach is not feasible and a gradient-based algorithm is used instead.

In Algorithm 2 the outline of the iterative algorithm is reported. After the setup, where the initial state and initial functional value are computed, the algorithm consists of two nested loops. In the outer loop the adjoint system is solved together with the control equation in order to obtain the gradient direction. In the inner loop a backtracking line search with step length parameter r is used. The step length is initially set to one and is iteratively reduced during the line search until a lower value of the objective functional is obtained. This algorithm stops either when the step length becomes lower than a minimum value *toll* or when two consecutively computed functional values are similar, i.e., no more improvements can be obtained. Nonlinear iterations are required for the solution of the FSI state equations (Step 8. in Algorithm 2), thus increasing the complexity of the algorithm. To perform the nonlinear iterations we use a classical Picard method, with a given tolerance ϵ. Since the adjoint FSI system is linear in its unknowns then it can be solved directly without nonlinear iterations. Furthermore, we usually do not need the solution of the adjoint displacement equation to compute the control update and therefore it may be neglected, thus reducing the complexity of the adjoint system.

We would like to focus now on the line search subroutine and in particular on Step 8. in Algorithm 2. During the first steps of every line search the control parameter can have extremely large values, leading to a failure of the FSI solver (e.g. due to not physical, enormous, solid displacement). However, we do not want to limit *a priori* the control parameter range, since by doing so we might lose some optimal control results. As a consequence, every time a line search is unsuccessful we discard the new solution and reload the last optimal solution obtained, that will then be used as *initial* condition during the nonlinear iterations of the following line search.

Furthermore, another aspect we have to keep into consideration concerns the preconditioner used to improve the convergence properties of the linear system we are solving. When solving the linear systems obtained after the discretization our solver keeps the same preconditioner as long as reasonably possible, thus saving computational time. However, under the circumstances above (failure of the FSI solver), the preconditioner in use might have been computed with a very different (and *wrong*) FSI matrix, leading to convergence issues. Therefore, since the FSI preconditioner must not be affected by the previous iterations it has to be computed from scratch at the beginning of every line search.

In the following Chapters some FSI optimal control problems are studied. A pressure boundary control problem is presented in Chapter 3, a distributed control approach in Chapter 4 and in Chapter 5 we studied an inverse parameter estimation problem for the estimate of the solid Young modulus. Every Chapter is self consistent since it contains its specific mathematical formulation and can then be read independently from the others. Few numerical tests are reported at the end of each Chapter. One of the test cases is studied for all the optimal control methods presented, keeping the same geometry, objective functional, reference state, material properties and boundary conditions in order to compare the effectiveness of the methods.

CHAPTER 3

Boundary pressure control

In this Chapter we investigate a pressure boundary optimal control approach to the fluid-structure interaction problem based on the Lagrangian multipliers formalism presented in Chapter 2. The objective of the problem is to minimize a displacement field functional in a specific region of the solid domain. This is obtained through a pressure control acting on a fluid boundary that bends the solid and the location of the fluid domain. The rest of this Chapter is organized as follows. First, we derive the optimality system arising from the Lagrangian functional minimization and since solving iteratively the optimality system with a steepest descent method shows slow convergence we also propose a quasi-Newton method to improve the algorithm, see [44]. Finally, in order to support the proposed approach we implement both the algorithms in our finite element code FEMuS (available at [1]) and perform numerical tests in two and three-dimensional spaces.

3.1 Mathematical model

In this section we present the mathematical model of the FSI problem together with the derivation of the optimality system. The notation used for functional spaces and the mathematical model of the FSI problem can be found in details in Section 1.1. Nevertheless, for the sake of completeness, we report now the strong and weak forms of the FSI state system. The mathematical model of the steady state FSI problem in strong form is defined by the following set of equations

$$\nabla \cdot \boldsymbol{v} = 0 \qquad \text{on } \Omega_f\,, \tag{3.1}$$

$$\rho_f(\boldsymbol{v} \cdot \nabla)\boldsymbol{v} - \nabla \cdot \boldsymbol{\sigma}_f = \mathbf{0} \qquad \text{on } \Omega_f\,, \tag{3.2}$$

$$\nabla \cdot \boldsymbol{\sigma}_s(\boldsymbol{\eta}) = \mathbf{0} \qquad \text{on } \Omega_s\,. \tag{3.3}$$

The viscous stress tensor $\boldsymbol{\sigma}_f$ of a Newtonian fluid and the Cauchy strain tensor $\boldsymbol{\sigma}_s$ of a St. Venant Kirchhoff material read

$$\boldsymbol{\sigma}_f(p, \boldsymbol{v}) := -p\mathbf{I} + \mu_f(\nabla\boldsymbol{v} + \nabla\boldsymbol{v}^T)\,, \tag{3.4}$$

$$\boldsymbol{\sigma}_s(\boldsymbol{\eta}) := \lambda_s(\nabla \cdot \boldsymbol{\eta})\mathbf{I} + \mu_s(\nabla\boldsymbol{\eta} + \nabla\boldsymbol{\eta}^T)\,, \tag{3.5}$$

where p_f is the fluid pressure, μ_f the dynamic viscosity of the fluid while λ_s and μ_s are the solid Lamé parameters. In order to complete the FSI strong formulation we need to provide the following boundary and interface conditions

$$\begin{aligned}
\boldsymbol{v} &= \boldsymbol{v}_0 \quad \text{on } \Gamma_d^f, & \boldsymbol{\eta} &= \boldsymbol{\eta}_0 \quad \text{on } \Gamma_d^s\,,\\
\boldsymbol{\sigma}_f \cdot \mathbf{n}_f &= \mathbf{0} \quad \text{on } \Gamma_n^f, & \boldsymbol{\sigma}_s \cdot \mathbf{n}_s &= \mathbf{0} \quad \text{on } \Gamma_n^s\,,\\
\boldsymbol{\sigma}_f \cdot \mathbf{n}_f + \boldsymbol{\sigma}_s \cdot \mathbf{n}_s &= \mathbf{0} \quad \text{on } \Gamma_i, & \boldsymbol{v} &= \mathbf{0} \quad \text{on } \Gamma_i\,,
\end{aligned} \tag{3.6}$$

where Γ_d^f and Γ_d^s are the surfaces with Dirichlet boundary conditions for the fluid velocity and solid displacement, while on Γ_n^f and Γ_n^s standard homogeneous outflow boundary conditions are imposed. On the interface Γ_i the fluid velocity has to vanish and the normal components of the stress tensors $\boldsymbol{\sigma}$ have to be continuous. We denote with $\mathbf{n}_s$ and $\mathbf{n}_f$ the normal unit vector to the solid and fluid boundary with $\mathbf{n}_s = -\mathbf{n}_f$ on Γ_i. We remark that, by using a monolithic approach in a finite element framework, the interface conditions are imposed directly in the same solver and there is no need to iterate and obtain the correct interface values, see [32, 19, 20].

We can write the monolithic FSI system in weak form for the displacement $\boldsymbol{\eta}$ and for the velocity field $\boldsymbol{v}$ over $\Omega(\boldsymbol{\eta}) = \Omega_f(\boldsymbol{\eta}) \cup \Omega_s(\boldsymbol{\eta})$, which implicitly incorporates the boundary conditions (3.6) on the common interface Γ_i.

$$
\begin{aligned}
&\int_{\Omega_f} (\nabla \cdot \boldsymbol{v})\, \psi \, d\Omega \; = 0 && \forall \psi \in L^2(\Omega_f)\,, && (3.7)\\
&\int_{\Omega_f} [(\rho_f(\boldsymbol{v}\cdot\nabla)\boldsymbol{v})\cdot\boldsymbol{\phi} - p\nabla\cdot\boldsymbol{\phi} + \mu_f\nabla\boldsymbol{v} : \nabla\boldsymbol{\phi}]\, d\Omega + \\
&\quad \int_{\Omega_s} [\lambda_s(\nabla\cdot\boldsymbol{\eta})(\nabla\cdot\boldsymbol{\phi}) + \mu_s\nabla\boldsymbol{\eta} : \nabla\boldsymbol{\phi}]\, d\Omega + && && (3.8)\\
&\quad \int_{\Gamma} [\mu_s(\boldsymbol{\nabla}\boldsymbol{\eta}\cdot\mathbf{n}_s)\cdot\boldsymbol{\phi} + \lambda_s(\boldsymbol{\nabla}\cdot\boldsymbol{\eta})(\mathbf{n}_s\cdot\boldsymbol{\phi})]] d\Gamma + \\
&\quad \int_{\Gamma} [[p\mathbf{n}_f - \mu_f(\boldsymbol{\nabla}\boldsymbol{v}\cdot\mathbf{n}_f)\cdot\boldsymbol{\phi}]\, d\Gamma = 0 && \forall \boldsymbol{\phi} \in \mathbf{H}^1_{\Gamma^s_d}(\Omega) \cap \mathbf{H}^1_{\Gamma^f_d}(\Omega)\,.
\end{aligned}
$$

The surface integrals vanish due to the boundary and interface conditions (3.6) and consequently the weak form of the FSI system is given by (3.7-3.8). If we now use the standard techniques to obtain the optimality system then the adjoint system results with uncoupled boundary conditions on the interface. This optimality system shows non-symmetric and non-monolithic patterns that differ from those of the state variable equations (3.7-3.8). In order to solve state and adjoint equations with a similar monolithic structure we need to extend the state variables in an appropriate way.

Over the solid domain $\Omega_s(\boldsymbol{\eta})$ we define the auxiliary displacement field $\widehat{\boldsymbol{\eta}}$, solution of the following Laplace operator and boundary conditions

$$
\begin{aligned}
&\nabla^2\widehat{\boldsymbol{\eta}} = \mathbf{0} \qquad \mathbf{x} \in \Omega_s\,, && (3.9)\\
&\widehat{\boldsymbol{\eta}} = \boldsymbol{\eta} \quad \text{on } \Gamma_i\,, && (3.10)\\
&\widehat{\boldsymbol{\eta}} = \mathbf{0} \quad \text{on } (\partial\Omega_s - \Gamma_i)\,. && (3.11)
\end{aligned}
$$

Therefore, over the whole domain Ω, we can define the velocity field $\boldsymbol{v}$ as

$$
\boldsymbol{v} = \left\{ \begin{array}{cc} \tau\,(\boldsymbol{\eta} - \widehat{\boldsymbol{\eta}}) & \text{on } \Omega_s(\boldsymbol{\eta}) \\ \boldsymbol{v} & \text{solution of (3.1)-(3.2) on } \Omega_f(\boldsymbol{\eta}) \end{array} \right. , \tag{3.12}
$$

with τ a positive constant. It is clear that $\Omega_f(\boldsymbol{\eta}) = \Omega_f(\widehat{\boldsymbol{\eta}})$ and $\Omega_s(\boldsymbol{\eta}) = \Omega_s(\widehat{\boldsymbol{\eta}})$ with $\boldsymbol{v} = 0$ on Γ_i. During the optimization process the function

$$
\widehat{\boldsymbol{\eta}} : \Omega_s(\widehat{\mathbf{0}}) \to \Omega_s(\widehat{\mathbf{1}}) \tag{3.13}
$$

can be seen as a mapping that defines the solid domain during the displacing process. The velocity field $\boldsymbol{v}$ is assumed to be continuous over Γ_i. It is important to remark that the physical velocity in the solid is zero. With this extension we may compute differential quantities of a functional, like shape derivatives of $\Omega_s(\widehat{\boldsymbol{\eta}})$ and $\Omega_f(\widehat{\boldsymbol{\eta}})$. It is more convenient to impose on the boundary Γ_i the (3.12), which allows variation of the fields $\widehat{\boldsymbol{\eta}}$ and $\boldsymbol{\eta}$ even over the solid domain, instead of (3.10). With this notation the FSI problem can be written as

$$\int_{\Omega_f(\widehat{\boldsymbol{\eta}})} (\nabla \cdot \boldsymbol{v})\, \psi \, d\Omega = 0 \qquad \forall \psi \in L^2(\Omega_f)\,, \tag{3.14}$$

$$\begin{aligned} &\int_{\Omega_f(\widehat{\boldsymbol{\eta}})} [(\rho_f(\boldsymbol{v} \cdot \nabla)\boldsymbol{v}) \cdot \boldsymbol{\phi} - p\nabla \cdot \boldsymbol{\phi} + \mu_f \nabla \boldsymbol{v} : \nabla \boldsymbol{\phi}]\, d\Omega + \\ &\quad \int_{\Omega_s(\widehat{\boldsymbol{\eta}})} [\mu_s \nabla \boldsymbol{\eta} : \nabla \boldsymbol{\phi} + \lambda_s(\nabla \cdot \boldsymbol{\eta})(\nabla \cdot \boldsymbol{\phi})]\, d\Omega = 0 \qquad \forall \boldsymbol{\phi} \in \mathbf{H}^1_{\Gamma^s_d} \cap \mathbf{H}^1_{\Gamma^f_d}(\Omega)\,, \end{aligned} \tag{3.15}$$

$$\int_{\Omega_s(\widehat{\boldsymbol{\eta}})} \nabla \widehat{\boldsymbol{\eta}} : \nabla \widehat{\boldsymbol{\eta}}_a \, d\Omega = 0 \qquad \forall\, \widehat{\boldsymbol{\eta}}_a \in \mathbf{H}^1_{\Gamma_s}(\Omega_s)\,, \tag{3.16}$$

$$\int_{\Omega_s(\widehat{\boldsymbol{\eta}})} (\boldsymbol{v} - \tau(\boldsymbol{\eta} - \widehat{\boldsymbol{\eta}})) \cdot \boldsymbol{\beta}_a \, d\Omega = 0 \qquad \forall \boldsymbol{\beta}_a \in \mathbf{L}^2_{\Gamma_s}(\Omega_s)\,. \tag{3.17}$$

In the following we refer to (3.14-3.17) as *state system* in weak form.

3.1.1 Optimality System

In an optimal control framework it is necessary to choose the objective of the problem and the control parameters. In this work we study a displacement matching profile problem where the control is the pressure on a subset of the fluid boundary. The objective functional, that we aim to minimize, then reads

$$\mathcal{J}(\boldsymbol{\eta}, p_c) = \frac{1}{2}\int_{\Omega_d} \omega ||\boldsymbol{\eta} - \boldsymbol{\eta}_d||^2 \, d\Omega + \frac{1}{2}\beta \int_{\Gamma_c} |p_c|^2 \, d\Gamma\,. \tag{3.18}$$

The first term takes into account the difference in norm between the solid displacement $\boldsymbol{\eta}$ and its target value $\boldsymbol{\eta}_d$. The solid sub-domain $\Omega_d \subseteq \Omega_s$ is the observation region where we want to reach the objective and ω is a constant weight function that vanishes on the boundary $\partial\Omega_d$. The second term is a regularization contribution needed to penalize the boundary pressure p_c, which is then limited to the space of non singular square integrable functions $L^2(\Gamma)$. In order to derive the optimality system we write the following augmented Lagrangian that is the sum of the objective functional and of the FSI equations multiplied by appropriate Lagrangian multipliers, i.e. the adjoint variables

$$
\begin{aligned}
\mathcal{L}(p, \boldsymbol{v}, \boldsymbol{\eta}, \widehat{\boldsymbol{\eta}}, p_a, \boldsymbol{v}_a, \widehat{\boldsymbol{\eta}}_a, \widehat{\mathbf{s}}_a, \beta_a) &= \mathcal{J}(\boldsymbol{\eta}, p_c) + \int_{\Omega_f} (\nabla \cdot \boldsymbol{v})\, p_a \, d\Omega \\
&+ \int_{\Gamma_c} (\boldsymbol{v}_a \cdot \mathbf{n}) p \, d\Gamma + \int_{\Omega_f} [\rho_f (\boldsymbol{v} \cdot \nabla)\boldsymbol{v} + \nabla p - \nabla \cdot (\mu_f \nabla \boldsymbol{v})] \cdot \boldsymbol{v}_a \, d\Omega \\
&+ \int_{\Omega_s} \big[-\nabla \cdot (\mu_s \nabla \boldsymbol{\eta} + \lambda_s \mathbf{I} (\nabla \cdot \boldsymbol{\eta})) \big] \cdot \boldsymbol{v}_a \, d\Omega + \int_{\Omega_s} \nabla^2 \widehat{\boldsymbol{\eta}} \cdot \widehat{\boldsymbol{\eta}}_a \, d\Omega \qquad (3.19) \\
&+ \int_{\Gamma_i} \widehat{\mathbf{s}}_a \cdot \left[(\widehat{\boldsymbol{\eta}} - \boldsymbol{\eta}) + \frac{\boldsymbol{v}}{\tau} \right] d\Gamma + \int_{\Omega_s} \boldsymbol{\beta}_a \cdot [\boldsymbol{v} - \tau(\boldsymbol{\eta} - \widehat{\boldsymbol{\eta}})] \, d\Omega \, .
\end{aligned}
$$

We use label a to denote the adjoint variable $(p_a, \boldsymbol{v}_a, \widehat{\boldsymbol{\eta}}_a, \boldsymbol{\beta}_a)$ of the corresponding state variable. Then, the solution that minimizes the functional $\mathcal{J}$ under the constraints given by the FSI system is a stationary point of the Lagrangian functional $\mathcal{L}$ and therefore can be computed by imposing the following first order necessary minimization condition

$$
\delta \mathcal{L} = 0 \, . \qquad (3.20)
$$

In the following we use notation δq for the variation of the generic function q and $(D\mathcal{L}/Dq)\delta q$ for the Fréchet derivative of functional $\mathcal{L}$ in the direction δq. Moreover, the shape derivatives of the functionals F_1 and F_2 on a moving domain with velocity $\delta \boldsymbol{v}$ are given by [54]

$$
\frac{dF_1}{d\Omega(\widehat{\boldsymbol{\eta}})} \delta \boldsymbol{v} = \int_{\partial\Omega(\widehat{\boldsymbol{\eta}})} y \delta \boldsymbol{v} \cdot \mathbf{n} \, d\Gamma \, , \qquad (3.21)
$$

$$
\frac{dF_2}{d\Gamma(\widehat{\boldsymbol{\eta}})} \delta \boldsymbol{v} = \int_{\Gamma(\widehat{\boldsymbol{\eta}})} (\nabla_n + \chi) \, y \delta \boldsymbol{v} \cdot \mathbf{n} \, d\Gamma \, , \qquad (3.22)
$$

where ∇_n is the normal derivative operator and χ the mean curvature of Γ. Since the variations of all the variables are independent we can extract and set to zero the sum of terms containing each variation [30]. When we consider the variations of the adjoint variables $(p_a, \boldsymbol{v}_a, \widehat{\boldsymbol{\eta}}_a, \boldsymbol{\beta}_a)$ we obtain the weak form of the FSI *state system* (3.14-3.17), which can be solved with a monolithic approach. When we focus on the variations of the state variables $(\boldsymbol{v}, p, \boldsymbol{\eta}, \widehat{\boldsymbol{\eta}})$ we obtain the weak form of the adjoint system. We start collecting $\delta \boldsymbol{v}$ terms obtaining

$$
\begin{aligned}
&\frac{D\mathcal{L}}{D\boldsymbol{v}}\delta\boldsymbol{v} = \int_{\Omega_f} (\nabla\cdot\delta\boldsymbol{v})\, p_a\, d\Omega \;+ \int_{\Omega_s} \delta\boldsymbol{v}\cdot\boldsymbol{\beta}_a\, d\Omega + \int_{\Gamma_c} \left[(\nabla_n+\chi)\frac{\beta p^2}{2}\right]\delta\boldsymbol{v}\cdot\mathbf{n}\, d\Gamma + \\
&\int_{\Omega_f} \Big[\, (\rho_f(\delta\boldsymbol{v}\cdot\nabla)\boldsymbol{v})\cdot\boldsymbol{v}_a + (\rho_f(\boldsymbol{v}\cdot\nabla)\delta\boldsymbol{v})\cdot\boldsymbol{v}_a - \nabla\cdot(\mu_f\nabla\delta\boldsymbol{v})\cdot\boldsymbol{v}_a\Big]\, d\Omega + \\
&\int_{\partial\Omega_f} (\nabla\cdot\boldsymbol{v})\, p_a\, \delta\boldsymbol{v}\cdot\mathbf{n}\, d\Gamma \;+ \int_{\partial\Omega_d} \omega\frac{(\boldsymbol{\eta}-\boldsymbol{\eta}_d)^2}{2}\delta\boldsymbol{v}\cdot\mathbf{n}\, d\Omega + \frac{1}{\tau}\int_{\Gamma_i} \delta\boldsymbol{v}\cdot\widehat{\mathbf{s}}_a\, d\Gamma + \\
&\int_{\partial\Omega_f} \boldsymbol{v}_a\cdot\Big[\rho_f(\boldsymbol{v}\cdot\nabla)\boldsymbol{v} + \nabla p - \nabla\cdot(\mu_f\nabla\boldsymbol{v})\Big]\delta\boldsymbol{v}\cdot\mathbf{n}\, d\Gamma \;+ \qquad\qquad (3.23) \\
&\int_{\partial\Omega_s} \boldsymbol{v}_a\cdot\Big[\, -\nabla\cdot(\mu_s\nabla\boldsymbol{\eta} + \lambda_s\mathbf{I}(\nabla\cdot\boldsymbol{\eta}))\,\Big]\delta\boldsymbol{v}\cdot\mathbf{n}\;\, d\Gamma + \\
&\int_{\partial\Omega_s} \big(\nabla^2\widehat{\boldsymbol{\eta}}\cdot\widehat{\boldsymbol{\eta}}_a\big)\,\delta\boldsymbol{v}\cdot\mathbf{n}\, d\Gamma + \int_{\Gamma_i} (\nabla_n+\chi)\left[\widehat{\mathbf{s}}_a\cdot\left[(\widehat{\boldsymbol{\eta}}-\boldsymbol{\eta}) + \frac{\boldsymbol{v}}{\tau}\right]\right]\;\delta\boldsymbol{v}\cdot\mathbf{n}\, d\Gamma + \\
&\int_{\partial\Omega_s} \boldsymbol{\beta}_a\cdot[\boldsymbol{v} - \tau(\boldsymbol{\eta}-\widehat{\boldsymbol{\eta}})]\;\delta\boldsymbol{v}\cdot\mathbf{n}\, d\Gamma = 0 \qquad\qquad \forall\delta\boldsymbol{v}\in\mathbf{H}^1_{\Gamma^f_d\cap\Gamma^s_d}(\Omega)\,.
\end{aligned}
$$

Many terms can be rearranged and simplified in order to obtain a system suitable to numerical solution. First we notice that the shape derivative terms vanish when the integrated function vanishes on the boundary, so the terms integrated on $\partial\Omega_s$ and $\partial\Omega_f$ in (3.23) can be neglected. Furthermore one can prove that the following term

$$
\int_{\Gamma_i} (\nabla_n+\chi)\left[\widehat{\mathbf{s}}_a\cdot\left[(\widehat{\boldsymbol{\eta}}-\boldsymbol{\eta}) + \frac{\boldsymbol{v}}{\tau}\right]\right]\;\delta\boldsymbol{v}\cdot\mathbf{n}\, d\Gamma\,, \tag{3.24}
$$

is equal to zero, too. In fact when we multiply by the curvature χ the term in square brackets, which is zero due to (3.17), we obtain a null contribution. The term $\widehat{\mathbf{s}}_a$ is defined on the surface Γ_i and a constant extension of this value towards the normal direction to the surface leads to a null normal gradient of this term, so (3.24) becomes

$$
\int_{\Gamma_i} \widehat{\mathbf{s}}_a\cdot\nabla_n\left[(\widehat{\boldsymbol{\eta}}-\boldsymbol{\eta}) + \frac{\boldsymbol{v}}{\tau}\right]\;\delta\boldsymbol{v}\cdot\mathbf{n}\, d\Gamma\,. \tag{3.25}
$$

Since (3.17) is valid on the whole domain Ω_s, this term vanishes [54]. The surface integral over $\partial\Omega_d$ vanishes since the weight function ω is vanishing over that surface and does not depend on $\widehat{\boldsymbol{\eta}}$, which means that the target region Ω_d moves integrally with Ω_s. Finally, the controlled boundary Γ_c is fixed so the integral over that surface vanishes. After these simplifications the variation in $\delta\boldsymbol{v}$ gives

$$\begin{aligned}&\int_{\Omega_f} [(\rho_f(\delta\boldsymbol{v}\cdot\nabla)\boldsymbol{v})\cdot\boldsymbol{v}_a + (\rho_f(\boldsymbol{v}\cdot\nabla)\delta\boldsymbol{v})\cdot\boldsymbol{v}_a - \nabla\cdot(\mu_f\nabla\delta\boldsymbol{v})\cdot\boldsymbol{v}_a]\,d\Omega + \\ &\int_{\Omega_f}(\nabla\cdot\delta\boldsymbol{v})\,p_a\,d\Omega + \int_{\Omega_s}\delta\boldsymbol{v}\cdot\boldsymbol{\beta}_a\,d\Omega + \frac{1}{\tau}\int_{\Gamma_i}\delta\boldsymbol{v}\cdot\widehat{\mathbf{s}}_a\,d\Gamma \quad \forall\delta\boldsymbol{v}\in\mathbf{H}^1_{\Gamma^f_d\cap\Gamma^s_d}(\Omega)\,.\end{aligned}\tag{3.26}$$

For $\delta\boldsymbol{\eta}$ we have

$$\begin{aligned}\frac{D\mathcal{L}}{D\boldsymbol{\eta}}\delta\boldsymbol{\eta} = &\int_{\Omega_d}\omega(\boldsymbol{\eta}-\boldsymbol{\eta}_d)\delta\boldsymbol{\eta}\,d\Omega + \int_{\Omega_s}[\mu_s\nabla\delta\boldsymbol{\eta}:\nabla\boldsymbol{v}_a + \lambda_s(\nabla\cdot\delta\boldsymbol{\eta})(\nabla\cdot\boldsymbol{v}_a)]\;d\Omega \\ &-\tau\int_{\Omega_s}\delta\boldsymbol{\eta}\cdot\boldsymbol{\beta}_a\,d\Omega - \int_{\Gamma_i}\widehat{\mathbf{s}}_a\cdot\delta\boldsymbol{\eta}\,d\Gamma = 0 \qquad \forall\delta\boldsymbol{\eta}\in\mathbf{H}^1_{\Gamma^s_d}(\Omega_s)\,.\end{aligned}\tag{3.27}$$

By performing integration by parts on the term where the variation $\delta\boldsymbol{\eta}$ is differentiated we obtain the values of $\boldsymbol{\beta}_a$ and $\widehat{\mathbf{s}}_a$

$$\boldsymbol{\beta}_a = -\frac{1}{\tau}\nabla\cdot[\mu_s\nabla\boldsymbol{v}_a + \lambda_s\mathbf{I}(\nabla\cdot\boldsymbol{v}_a)] + \frac{\omega}{\tau}(\boldsymbol{\eta}-\boldsymbol{\eta}_d)\,,\tag{3.28}$$

$$\widehat{\mathbf{s}}_a = [\mu_s\nabla\boldsymbol{v}_a + \lambda_s\mathbf{I}(\nabla\cdot\boldsymbol{v}_a)]\cdot\mathbf{n}\,.\tag{3.29}$$

By using (3.28-3.29), the (3.26) becomes

$$\begin{aligned}&\int_{\Omega_f}(\nabla\cdot\delta\boldsymbol{v})\,p_a\,d\Omega + \frac{1}{\tau}\int_{\Omega_s}[\mu_s\nabla\boldsymbol{v}_a:\nabla\delta\boldsymbol{v} + \lambda_s(\nabla\cdot\boldsymbol{v}_a)(\nabla\cdot\delta\boldsymbol{v})]\;d\Omega + \\ &\int_{\Omega_f}\Big[(\rho_f(\delta\boldsymbol{v}\cdot\nabla)\boldsymbol{v})\cdot\boldsymbol{v}_a + (\rho_f(\boldsymbol{v}\cdot\nabla)\delta\boldsymbol{v})\cdot\boldsymbol{v}_a - \nabla\cdot(\mu_f\nabla\delta\boldsymbol{v})\cdot\boldsymbol{v}_a\Big]\,d\Omega + \\ &\frac{1}{\tau}\int_{\Omega_d}\omega(\boldsymbol{\eta}-\boldsymbol{\eta}_d)\delta\boldsymbol{v}\,d\Omega = 0 \qquad \forall\delta\boldsymbol{v}\in\mathbf{H}^1_{\Gamma^f_d\cap\Gamma^s_d}(\Omega)\,.\end{aligned}\tag{3.30}$$

Collecting $\delta\widehat{\boldsymbol{\eta}}$ we obtain

$$\int_{\Omega_s}\nabla\delta\widehat{\boldsymbol{\eta}}:\nabla\widehat{\boldsymbol{\eta}}_a\,d\Omega + \tau\int_{\Omega_s}\delta\widehat{\boldsymbol{\eta}}\cdot\boldsymbol{\beta}_a\,d\Omega + \int_{\Gamma_i}\widehat{\mathbf{s}}_a\cdot\delta\widehat{\boldsymbol{\eta}}\,d\Gamma = 0 \quad \forall\delta\widehat{\boldsymbol{\eta}}\in\mathbf{H}^1_{\Gamma^s_d}(\Omega_s)\,.\tag{3.31}$$

With (3.28-3.29) the (3.31) reads

$$\begin{aligned}\int_{\Omega_s}\nabla\widehat{\boldsymbol{\eta}}_a:\nabla\delta\widehat{\boldsymbol{\eta}}\,d\Omega = &-\int_{\Omega_s}[\mu_s\nabla\boldsymbol{v}_a:\nabla\delta\widehat{\boldsymbol{\eta}} + \lambda_s(\nabla\cdot\boldsymbol{v}_a)(\nabla\cdot\delta\widehat{\boldsymbol{\eta}})]\;d\Omega + \\ &\int_{\Omega_d}\omega(\boldsymbol{\eta}-\boldsymbol{\eta}_d)\delta\widehat{\boldsymbol{\eta}}\,d\Omega \qquad \forall\delta\widehat{\boldsymbol{\eta}}\in\mathbf{H}^1_{\Gamma^s}(\Omega_s)\,.\end{aligned}\tag{3.32}$$

Finally, the equation for the variation δp gives

$$\int_{\Gamma_c} (p\beta + \boldsymbol{v}_a \cdot \mathbf{n})\delta p \; d\Gamma - \int_{\Omega_f} (\nabla \cdot \boldsymbol{v}_a)\delta p \; d\Omega = 0 \qquad \forall \delta p \in L^2(\Omega)\,. \tag{3.33}$$

The contribution of the surface term over the controlled boundary Γ_c gives the following control equations

$$p_c = p = -\frac{\boldsymbol{v}_a \cdot \mathbf{n}}{\beta}\,. \tag{3.34}$$

To summarize, the adjoint system in weak form is represented by

$$\int_{\Omega_f} (\nabla \cdot \boldsymbol{v}_a)\delta p \; d\Omega = 0 \qquad \forall \delta p \in L^2(\Omega)\,, \tag{3.35}$$

$$\begin{aligned}
&\int_{\Omega_f} (\nabla \cdot \delta\boldsymbol{v})\, p_a \, d\Omega + \frac{1}{\tau}\int_{\Omega_s} [\mu_s \nabla \boldsymbol{v}_a : \nabla \delta\boldsymbol{v} + \lambda_s (\nabla \cdot \boldsymbol{v}_a)(\nabla \cdot \delta\boldsymbol{v})] \; d\Omega + \\
&\quad \int_{\Omega_f} \Big[(\rho_f (\delta\boldsymbol{v} \cdot \nabla)\boldsymbol{v}) \cdot \boldsymbol{v}_a + (\rho_f (\boldsymbol{v} \cdot \nabla)\delta\boldsymbol{v}) \cdot \boldsymbol{v}_a - \nabla \cdot (\mu_f \nabla \delta\boldsymbol{v}) \cdot \boldsymbol{v}_a \Big] \; d\Omega + \\
&\quad \frac{1}{\tau}\int_{\Omega_d} \omega(\boldsymbol{\eta} - \boldsymbol{\eta}_d)\delta\boldsymbol{v} \, d\Omega = 0 \qquad \forall \delta\boldsymbol{v} \in \mathbf{H}^1_{\Gamma^f_d \cap \Gamma^s_d}(\Omega)\,,
\end{aligned} \tag{3.36}$$

$$\begin{aligned}
&\int_{\Omega_s} \nabla \widehat{\boldsymbol{\eta}}_a : \nabla \delta\widehat{\boldsymbol{\eta}} \, d\Omega = -\int_{\Omega_s} [\mu_s \nabla \boldsymbol{v}_a : \nabla \delta\widehat{\boldsymbol{\eta}} + \lambda_s (\nabla \cdot \boldsymbol{v}_a)(\nabla \cdot \delta\widehat{\boldsymbol{\eta}})] \; d\Omega + \\
&\quad \int_{\Omega_d} \omega(\boldsymbol{\eta} - \boldsymbol{\eta}_d)\delta\widehat{\boldsymbol{\eta}} \, d\Omega \qquad \forall \delta\widehat{\boldsymbol{\eta}} \in \mathbf{H}^1_{\Gamma^s}(\Omega_s)\,.
\end{aligned} \tag{3.37}$$

If one is interested in the strong form of the *adjoint system*, for instance to obtain a proper finite volume discretization, it is necessary to perform integration by parts on the terms where the variations δ are differentiated. After performing the integration by parts, we recover the adjoint state $(\boldsymbol{v}^f_a, \boldsymbol{v}^s_a, p_a) \in \mathbf{H}^1_{\partial\Omega_f - \Gamma_i}(\Omega_f) \cap \mathbf{H}^2(\Omega_f) \times \mathbf{H}^1_{\partial\Omega_s - \Gamma_i}(\Omega_s) \cap \mathbf{H}^2(\Omega_s) \times L^2_0(\Omega_f) \cap \mathbf{H}^1(\Omega_f)$, by solving

$$\nabla \cdot \boldsymbol{v}^f_a = 0\,, \tag{3.38}$$

$$-\rho_f (\nabla \boldsymbol{v})^T \boldsymbol{v}^f_a + \rho_f [(\boldsymbol{v} \cdot \nabla)\boldsymbol{v}^f_a] + \nabla p_a - \nabla \cdot (\mu_f \nabla \boldsymbol{v}^f_a) = \frac{\omega}{\tau}(\boldsymbol{\eta} - \boldsymbol{\eta}_d)\,, \tag{3.39}$$

$$\nabla \cdot \mathbf{S}(\boldsymbol{v}^s_a) = 0\,. \tag{3.40}$$

with boundary conditions defined as

$$\begin{array}{ll}
\boldsymbol{v}^s_a = \boldsymbol{v}^f_a & \text{on } \Gamma_i\,, \\
\boldsymbol{\sigma}_s(\boldsymbol{v}^s_a) \cdot \mathbf{n} = \boldsymbol{\sigma}_f(\boldsymbol{v}^f_a) \cdot \mathbf{n} & \text{on } \Gamma_i\,, \\
\mu_f (\nabla \boldsymbol{v}_a) \cdot \mathbf{n} = -(\boldsymbol{v} \cdot \mathbf{n})\, \boldsymbol{v}_a\,,\ p_a = 0 & \text{on } \Gamma^f_n\,, \\
\boldsymbol{v}_a = 0 & \text{on } \Gamma_{fd} \cup \Gamma_{sd}\,.
\end{array} \tag{3.41}$$

We remark the duality between (3.41) and (3.6). In fact if a Dirichlet boundary condition for a state variable is set then the corresponding adjoint variable must satisfy the same type of condition in homogeneous form. The adjoint velocity $\boldsymbol{v}_a$ must be continuous and different from zero on the interface since the source term $\omega(\boldsymbol{\eta} - \boldsymbol{\eta}_d)/\tau$ is active only in the solid region and the information has to propagate towards the control boundary Γ_c, which is part of the fluid domain. We also remark that since we use a monolithic approach with a finite element approximation for both the state (3.14-3.15) and the adjoint system (3.35-3.36) the equilibrium conditions on the interface are automatically satisfied.

3.2 Numerical implementation and tests

The optimality system obtained in the previous section is highly nonlinear and doubles the unknowns of a standard FSI simulation. Its solution is a very difficult task and we propose a *segregated* approach, splitting the solution of the state and adjoint equations to combine the result in the control gradient equation. By doing so we use the same solver for the solution of the state (3.14-3.15) and the adjoint systems (3.35-3.36) with only minor modifications. The outline of the method used for the iterative solution of the optimality system is described in Algorithm 3. After the setup, where the initial state and the initial functional value are computed, the algorithm consists of two nested loops. In the outer loop the adjoint system (3.35-3.36) is solved together with the control equation in order to obtain the gradient direction δp. In the inner loop a backtracking line search based on the Armijo strategy is used [3]. Here we use a contraction factor $\rho = 0.7$. This algorithm stops either when the step length becomes lower than a minimum value $toll = 10^{-8}$ or when two consecutively computed functional values are similar, i.e. no more improvements can be obtained. This algorithm is quite robust however it has a high computational cost: the optimal solution requires many line searches where the state system must be solved. Furthermore this method has a slow convergence rate and relies only on the information available at the current iteration to determine the direction of the functional gradient.

The use of more sophisticated approaches, such as Newton's or quasi-Newton methods, can significantly improve the convergence properties of the algorithm, see [44]. In quasi-Newton methods the approximation of the

Algorithm 3 Description of the Steepest Descent algorithm.

```
1. Set a state $(\boldsymbol{v}^0, p^0, \boldsymbol{\eta}^0)$ satisfying (3.14-3.15)   ▷ Setup of the state - Reference case
2. Compute the functional $\mathcal{J}^0$ in (3.18)
3. Set $r^0 = 1$
for $i = 1 \to i_{max}$ do
    4. Solve the system (3.35-3.36) to obtain the adjoint state $(\boldsymbol{v}_a^i, p_a^i)$
    5. Set the control update $\delta p^i = -(p_c^{i-1} + \boldsymbol{v}_a^i \cdot \mathbf{n}/\beta)$
    6. Set $r^i = r^0$
    while $\mathcal{J}^i(p_c^{i-1} + r^i \delta p^i) > \mathcal{J}^{i-1}(p_c^{i-1})$ do   ▷ Line search
        7. Set $r^i = \rho\, r^i$
        8. Solve (3.14-3.15) for the state $(\boldsymbol{v}^i, p^i, \boldsymbol{\eta}^i)$ with $p_c^i = p_c^{i-1} + r^i \delta p^i$
        if $r^i < toll$ then
            Line search not successful   ▷ End of the algorithm
        end if
    end while
end for
```

Hessian matrix of the functional is computed at every optimization iteration. In our case a quasi-Newton method can be of practical interest if compared to the requirements needed by a Newton's approach. Moreover, since in our work the control parameter is a scalar, the Hessian matrix denoted in the following as **B** has to be intended as the second derivative of the functional. The control update equation for δp becomes

$$\begin{aligned} \mathbf{B}^i &= \frac{\dfrac{\partial \mathcal{J}}{\partial p}(p^{i-1}) - \dfrac{\partial \mathcal{J}}{\partial p}(p^{i-2})}{(p^{i-1} - p^{i-2})}\,, \\ \delta p^i &= -(\mathbf{B}^i)^{-1}(p_c^{i-1} + \boldsymbol{v}_a^i \cdot \mathbf{n}/\beta)\,. \end{aligned} \tag{3.42}$$

Since the above formula evaluates an approximation of the Hessian by using information from the two previous iterations, it can be used only after the first iteration. The first iteration may be computed with a standard steepest descent. We implemented this algorithm in our in-house finite element code FEMuS (available at [1]), that works on multiprocessor architectures with openMPI libraries and uses a multigrid solver with mesh-moving capability [6, 9, 17]. We use standard quadratic-linear elements for the velocity and pressure solution in order to fulfill the *BBL inf-sup* condition. The displacements are approximated with standard quadratic elements. In the rest of this section we report the results obtained for some test cases with different values of the regularization parameter β. We compare the performance of the steepest descent and quasi-Newton methods in terms of total number of line searches, number of optimization iterations and functional reduction attained. The first case is a two-dimensional channel while in the second one we simulate a more complex three-dimensional geometry.

3.2.1 Test 1. Plane channel

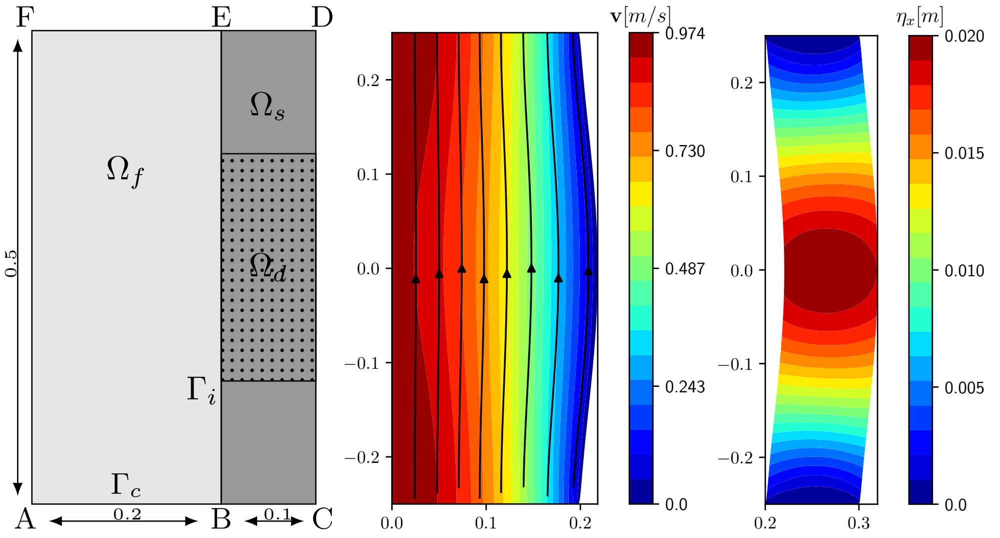

Figure 3.1: Geometry and controlled region defined by dotted square on the right Ω_d (left). Reference case with velocity profiles and streamlines in the liquid (middle). Solid displacement field η_x for the same reference configuration (right).

The geometry of our first test case is shown on the left of Figure 3.1. This simple test case has been studied with the optimal control approaches presented in Chapters 4 and 5, as well. We used the same boundary conditions, physical properties and objective functional, while changing the control parameter in order to compare the different controls in terms of functional reduction.

In this test a fluid flows vertically from the bottom to the top in a plane channel. The fluid region Ω_f is on the left while the solid domain Ω_s, in gray, is on the right. The dotted region is the controlled domain $\Omega_d \subset \Omega_s$ and the lower boundary AB is the control region Γ_c. The left boundary

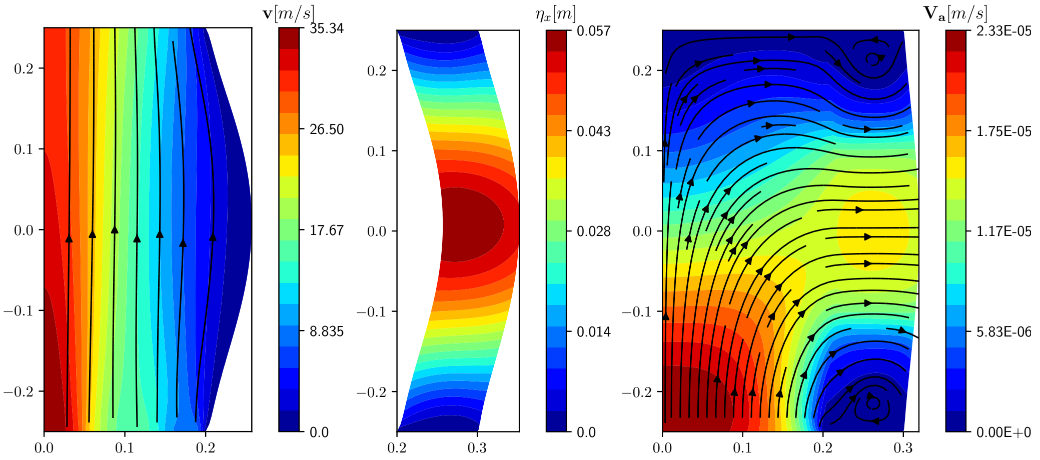

Figure 3.2: Controlled case with velocity profiles $\boldsymbol{v}$ and streamlines in the liquid and displacement $\boldsymbol{\eta}$ in the solid (on the left). Adjoint velocity $\boldsymbol{v}_a$ field and streamlines for the reference case configuration (on the right).

AF is a symmetry axis and on the top EF pressure boundary conditions with $p_{EF} = 10000Pa$ and vanishing tangential velocity are imposed. All the boundaries are fixed except the right segment CD, which is free to move with fixed endpoints C and D. The physical properties are the following

$$\rho_s = \rho_f = 10^3 kg/m^3, \quad \nu_f = 0.07m^2/s, \quad \nu_s = 0.2, \quad E = 10^6 Pa\,, \tag{3.43}$$

so the solid can easily bend. The optimal control algorithm searches the optimal pressure on the lower fluid boundary Γ_c such that the x-component of the displacement over the region Ω_d matches the uniform target value $\eta_d = 0.05m$. The displacement in the remaining part solid domain is not controlled and therefore can have any value, solution of the state system.

Now we present the results referring to the reference case, with $p^0 = 11500Pa$ on Γ_c. In the middle of Figure 3.1 the velocity profile in the fluid domain Ω_f is shown with streamlines. The solid displacement in the solid domain Ω_s is reported on the right of the same figure. The main deformation occurs around the middle point of the right boundary and the maximum value is $\eta_x = 0.02m$, lower than the target value η_d.

We report in Table 3.1 the functionals $\mathcal{J}(\boldsymbol{\eta}, p)$ and the mean values $\bar{\eta}_x$ of the x-component of the displacement in the controlled region Ω_d, obtained with different β values. By reducing β, the controlled solution tends to converge to the desired displacement and the functional values decrease. On the right of the same Figure a comparison is shown among the results obtained

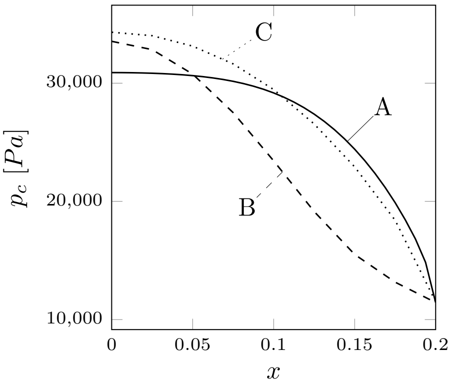

Figure 3.3: Control pressure profile with $\beta = 10^{-8}$ (A), $\beta = 10^{-9}$ (B) and $\beta = 10^{-10}$ (C).

β	$\mathcal{J}(\boldsymbol{\eta}, p)$	$\bar{\eta}_x$ $[m]$
∞	$1.292 \cdot 10^{-5}$	0.0180
10^{-8}	$9.192 \cdot 10^{-6}$	0.0202
10^{-9}	$1.515 \cdot 10^{-6}$	0.0469
10^{-10}	$6.454 \cdot 10^{-7}$	0.0497

Table 3.1: Objective functionals. The reference case with no control is labeled with $\beta = \infty$.

with different values of the regularization parameter β. The control pressure profile over Γ_c is reported as a function of the horizontal coordinate x for three values of the regularization parameter $\beta = 10^{-8}$, 10^{-9} and 10^{-10}. The pressure has a more uniform, regular profile as β, and therefore the intensity of the control, decreases. In Figure 3.2 we reported the results obtained when the optimal control problem is solved with $\beta = 10^{-10}$. On the left the fluid velocity with streamlines and the solid displacement are shown. Finally, on the right of the same figure the adjoint velocity field is reported with streamlines at the beginning of the optimization algorithm.

3.2.2 Test 2. Optimization methods comparison

Here, considering the domain of Figure 3.1, we want to test the accuracy of our algorithm and compare the steepest descent method with the quasi-Newton one. We first perform a forward simulation where we set a uniform pressure value on Γ_c and then compute the average deformation over the controlled region Ω_d. By using a boundary pressure $p_{fw} = 5500Pa$ on Γ_c we have $\bar{\eta} = 0.0582m$. This deformation is then imposed as the desired value η_d of the optimal controlled problem. By doing so we expect to recover, at the end of the optimization algorithm, an average pressure value close to p_{fw} taking in mind that the optimal pressure does not have a flat profile. On the left boundary AF we impose no-slip conditions and on the top EF pressure conditions with $p_{EF} = 4000Pa$ and vanishing tangential velocity.

Table 3.2: Case A. Objective functional value and optimization (Opt.)/line search (L.s.) number of iterations for the steepest descent and quasi-Newton methods as a function of different β. The reference case with no control is labeled with $\beta = \infty$.

	Steepest descent				Quasi-Newton			
β	$\mathcal{J}(\boldsymbol{\eta}, p)$	$p_{opt}[Pa]$	Opt.	L.s.	$\mathcal{J}(\boldsymbol{\eta}, p)$	$p_{opt}[Pa]$	Opt.	L.s.
∞	$2.554 \cdot 10^{-6}$	0	-	-	$2.554 \cdot 10^{-6}$	0	-	-
10^{-7}	$3.182 \cdot 10^{-7}$	5 057	6	193	$3.344 \cdot 10^{-7}$	5 308	4	42
10^{-9}	$8.998 \cdot 10^{-9}$	5 448	12	523	$1.009 \cdot 10^{-8}$	5 321	3	98
10^{-10}	$5.897 \cdot 10^{-9}$	5 467	16	794	$5.892 \cdot 10^{-9}$	5 463	8	65

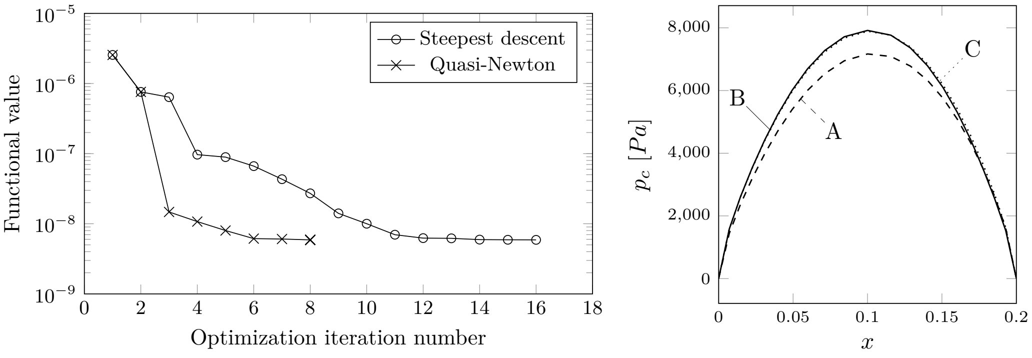

Figure 3.4: Case A. Functional values (left) for the steepest descent and quasi-Newton methods with $\beta = 10^{-10}$ and control pressure profile (right) on the lower fluid boundary Γ_c with $\beta = 10^{-7}$ (A), $\beta = 10^{-9}$ (B) and $\beta = 10^{-10}$ (C).

The physical properties are now the following

$$\rho_s = \rho_f = 10^3 kg/m^3,\ \nu_f = 0.07 m^2/s,\ \nu_s = 0.2,\ \mu_s = 7.65 \cdot 10^4 Pa\,. \quad (3.44)$$

We report in Table 3.2 the results obtained by applying the steepest descent and quasi-Newton methods explained in Algorithm 3 and (3.42) with different β values. With p_{opt} we denoted the mean pressure value on the control surface Γ_c at the end of the optimization process. By reducing β, the mean pressure p_{opt} approaches the optimal one $p_{fw} = 5500 Pa$ since the regularization contribution of the functional becomes negligible with respect to the objective contribution, with smaller corresponding functional values. We notice that the choice of the method does not influence the accuracy of the results in terms of functional reductions and pressure values. However, focusing on a specific value of the regularization parameter, for instance 10^{-10}, the steepest descent takes 16 optimization with 794 line search iterations to converge, while the quasi-Newton takes 8 optimization with only 65 line search iterations. On the left of Figure 3.4 the functional values are reported as a function of algorithm iterations for the two optimization methods, with $\beta = 10^{-10}$. On the right of the same Figure a comparison among the results obtained with different β is shown. The control pressure profile over Γ_c is reported as a function of the horizontal coordinate x for three values of the regularization parameter $\beta = 10^{-7}$, 10^{-9} and 10^{-10}. The pressure has a symmetric profile for all β and takes higher value as β increases.

3.2.3 Test 3. 3D accuracy test

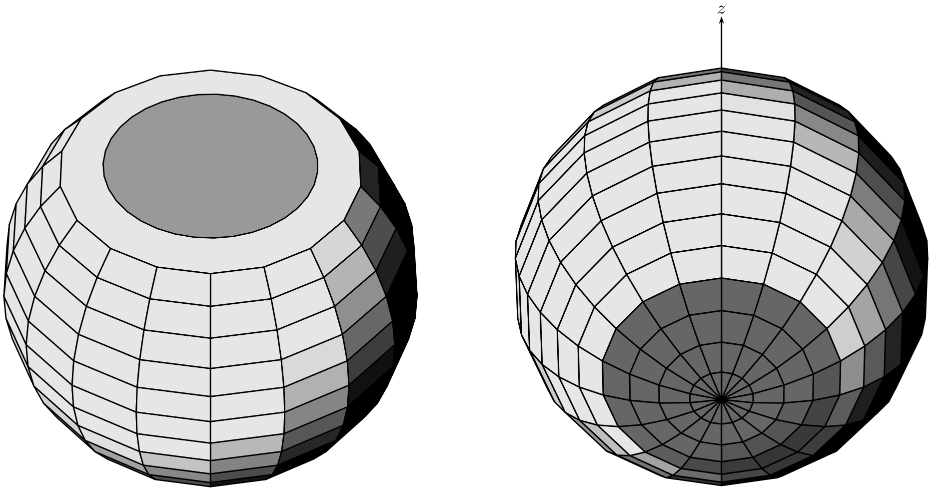

Figure 3.5: Case study geometry. Left: in gray is the liquid control surface Γ_c. Right: in gray is the solid controlled region Ω_d.

In this section we report the results of the three-dimensional geometry shown in Figure 3.5. The spherical domain consists of an external deformable solid that surrounds the internal fluid. On the upper liquid surface we prescribe a boundary condition of uniform pressure and vanishing tangential velocity while the lateral surfaces of the sphere are left free to move. Clearly by increasing the boundary pressure, the solid deformation becomes more

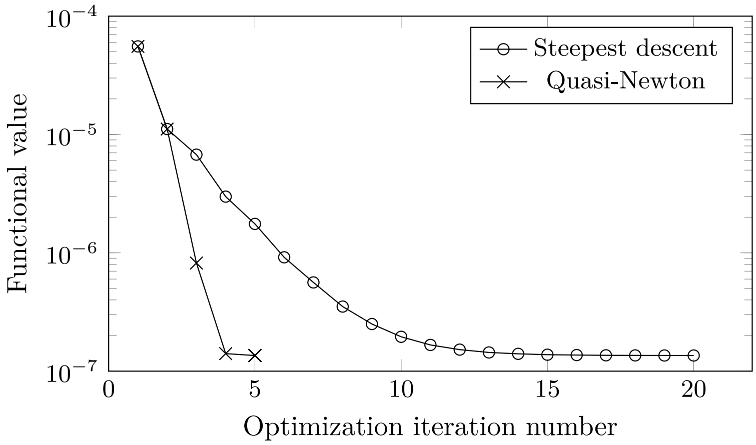

Figure 3.6: Convergence of the functional for the steepest descent and quasi-Newton methods, $\beta = 10^{-8}$.

Table 3.3: Effects of the regularization parameter β on objective functionals, optimization (Opt.) and line search (L.s.) number of iterations for the steepest descent and quasi-Newton methods. The reference case with no control is labeled with $\beta = \infty$.

	Steepest descent				Quasi-Newton			
β	$\mathcal{J}(\boldsymbol{\eta}, p)$	$p_{opt}[Pa]$	Opt.	L.s.	$\mathcal{J}(\boldsymbol{\eta}, p)$	$p_{opt}[Pa]$	Opt.	L.s.
∞	$5.552 \cdot 10^{-5}$	0	-	-	$5.552 \cdot 10^{-5}$	0	-	-
10^{-6}	$1.223 \cdot 10^{-5}$	19 455	8	75	$1.205 \cdot 10^{-5}$	18 809	4	43
10^{-7}	$1.259 \cdot 10^{-6}$	19 959	11	88	$1.260 \cdot 10^{-6}$	19 983	6	34
10^{-8}	$1.356 \cdot 10^{-7}$	20 005	20	126	$1.355 \cdot 10^{-7}$	19 988	5	40

relevant. The solid and fluid properties are the following

$$\rho_s = \rho_f = 10^3 kg/m^3,\ \nu_f = 0.02 m^2/s,\ \nu_s = 0.2,\ \mu_s = 7.65 \cdot 10^5 Pa\,. \tag{3.45}$$

The control problem searches the optimal pressure on the upper boundary such that the z-component of the displacement over the region Ω_d shown on the right of Figure 3.5 matches a uniform target value. We first perform a forward simulation imposing on the inlet boundary a uniform pressure $p_{fw} = 20000 Pa$, then compute the average deformation over the controlled region and obtain $7.0982 \cdot 10^{-2} m$. This value acts as target displacement η_d for our optimization test case. The initial control pressure value is $p^0 = 0 Pa$, far away from the optimal one $p_{fw} = 20000Pa$.

In Table 3.3 we reported the results of the optimization process obtained using both the steepest descent and quasi-Newton methods and for different values of the regularization parameter β. With p_{opt} we denoted the pressure value obtained at the end of the optimization process. We first notice that reducing β the pressure p_{opt} approaches the optimal one $p_{fw} = 20000Pa$. The choice of the method does not afflict the accuracy of the results in terms of functional reductions and pressure values. However, the steepest descent requires more optimization and line search iterations to converge than the quasi-Newton. The latter method is much less computationally expensive from a CPU point of view, while the memory requirements are similar since its implementation only requires to store few values of the functional gradient and control parameter more than for the steepest descent. Finally, in Figure 3.6, is reported the evolution of the functional values during the optimization process. We recall that the first iteration corresponds to the reference state and the second one is always obtained with a steepest descent line search method.

3.2.4 Test 4. 3D with auxiliary channel

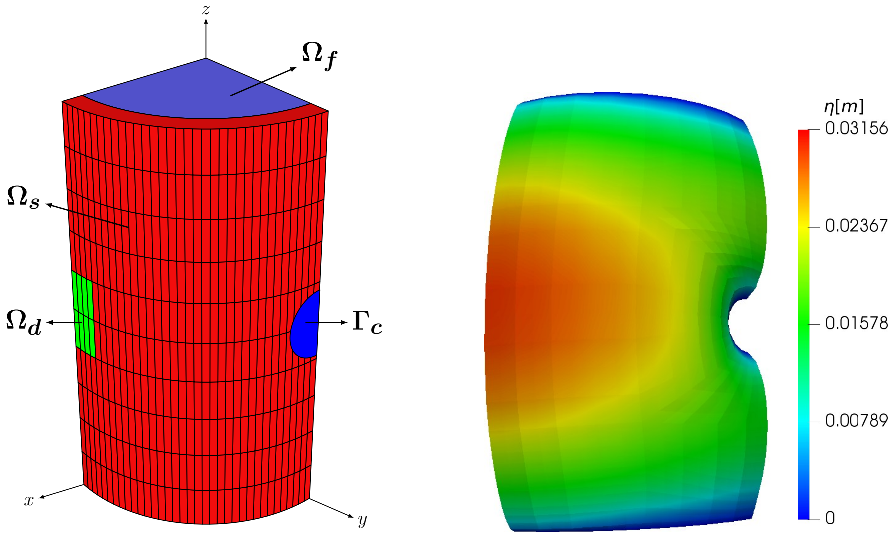

Figure 3.7: Case B. Geometry with controlled domain Ω_d (in green) (left) and solid displacement field for the reference configuration (right).

Table 3.4: Case B. Values of the parameter β and objective functional values with optimization (Opt.) and line search (L.s.) number of iterations for the steepest descent and quasi-Newton methods. The reference case with no control is labeled with $\beta = \infty$.

	Steepest descent			Quasi-Newton		
β	$\mathcal{J}(\boldsymbol{\eta}, p)$	Opt.	L.s.	$\mathcal{J}(\boldsymbol{\eta}, p)$	Opt.	L.s.
∞	$5.919 \cdot 10^{-9}$	-	-	$5.919 \cdot 10^{-9}$	-	-
10^{-9}	$1.258 \cdot 10^{-9}$	7	56	$1.134 \cdot 10^{-9}$	4	33
10^{-10}	$1.176 \cdot 10^{-9}$	7	82	$1.043 \cdot 10^{-9}$	4	39

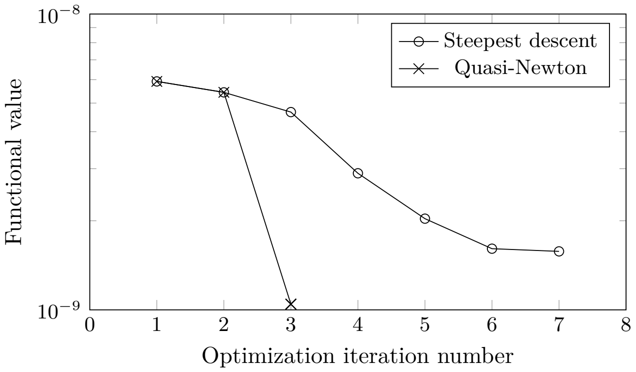

Figure 3.8: Case B. Convergence of the functional for the steepest descent and quasi-Newton methods, $\beta = 10^{-11}$.

Now we consider a test case where the control surface is an auxiliary duct and not the domain main fluid inlet, as it was in the previous cases. This approach could be more suitable for industrial applications. We present the results of the simulations of the three-dimensional geometry shown on the left of Figure 3.7. The domain is a cylindrical channel with a circular hole located in the middle of the cylinder. The radius of the inner fluid region is $0.1m$, the thickness of the solid is $0.015m$ and the height of the channel is $0.3m$. The fluid enters the channel from the bottom with a parabolic velocity profile $\boldsymbol{v} = (0,\, 0,\, 1 - 100 \times (x^2 + y^2))\, m/s$ and flows along the z-axis to the top. On the upper surface we prescribe a uniform pressure conditions $p = 5 \cdot 10^4 Pa$ and vanishing tangential velocity. The solid lateral boundaries are free to move, while the others are fixed. The hole in the solid represents

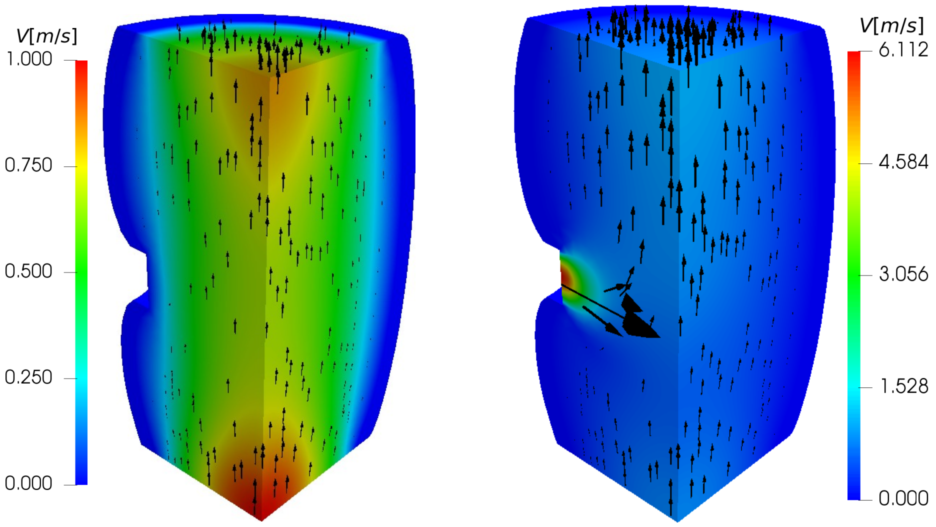

Figure 3.9: Case B. Velocity field profiles in the liquid for the reference case (on the left) and controlled case with $\beta = 10^{-10}$ (on the right).

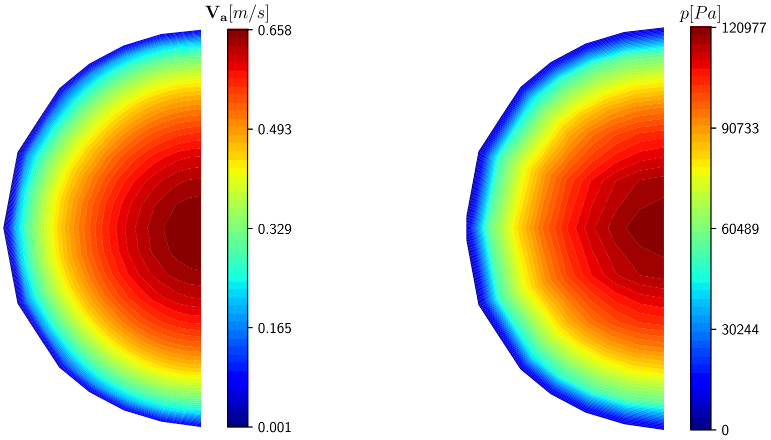

Figure 3.10: Case B. Adjoint velocity (on the left) and pressure (on the right) profiles over the control surface Γ_c for the controlled case with $\beta = 10^{-10}$.

an auxiliary duct connected to the main channel. Clearly if the duct pressure is higher than that of the channel internal fluid, then the auxiliary duct brings more fluid in the liquid domain, behaving as an injection. On the other hand if the pressure is lower than the internal one the fluid exits from the duct. For the case without control we impose a no-slip boundary condition so that the main fluid flow is not altered by the presence of the duct. The physical properties of the solid and liquid are the following

$$\rho_s = \rho_f = 10^3 kg/m^3,\ \nu_f = 0.1 m^2/s,\ \nu_s = 0.2,\ \mu_s = 7.65 \cdot 10^4 Pa\,. \tag{3.46}$$

Our control problem consists of finding the optimal pressure that has to be imposed on the auxiliary duct Γ_c, so that the solid displacement in the region Ω_d shown on the left of Figure 3.7 matches a given value.

First we report the uncontrolled FSI problem and then the results of the optimal controlled problem obtained with the steepest descent and quasi-Newton methods for different values of the regularization term β. On the right of Figure 3.7 the x-component of the solid displacement field is reported and its average value in the controlled region Ω_d, which is about $0.0295m$. We have then chosen as target value of our control problem $\eta_d = 0.031m$, aiming to increase the solid deformation. In Table 3.4 we report the results obtained by applying the steepest descent and quasi-Newton methods. It is worth noticing that the latter method requires less line searches and optimization iterations to minimize the functional, thus reducing the computational effort. Again one can see that the greatest improvement is obtained with the lowest β for both algorithms. We recall that due to its numerical implementation the first step performed by the quasi-Newton method is actually a steepest descent step as clearly visible in Figure 3.8 that shows the evolution of the functional values during the optimization process. In Figure 3.9 the velocity field obtained is compared with the reference case with no control, on the left, and with control, on the right. In the first case the flow is aligned with the channel axis, while in the controlled one the auxiliary duct injects fluid at high velocity into the channel that mixes with the main flow. Finally, in Figure 3.10 the pressure and adjoint velocity fields over the control surface Γ_c are reported. The profiles are very similar, as suggested by the control update equations (3.34, 3.42), with higher values near the center of the duct, that consequently is the region where the control acts more efficiently.

CHAPTER 4

Distributed optimal control applied to Fluid Structure Interaction problems

In this Chapter we study a fluid-structure interaction distributed optimal control problem. Inside this framework, the aim of our control problem is the minimization of two objective functionals with a distributed force that acts in the solid domain and changes the location of both the solid and fluid domains. We first consider a velocity tracking functional in a specific region of the fluid domain. This distributed control for FSI systems can be easily used to find the optimal shape of the solid domain that changes the fluid flow profile accordingly to our goal. The second functional of interest is a solid domain displacement matching functional. This control involves mainly the solid sub-problem, since both the control parameter and the objective functionals are located into the solid sub-domain. This distributed control approach is compared with the boundary control and parameter estimation problems presented in Chapter 3 and 5, respectively.

The rest of this Chapter is organized as follows. First we introduce the FSI governing equations in strong and weak form, then we derive the optimality system arising from the Lagrangian functional minimization. The steepest descent iterative algorithm used for the numerical solution of the optimality system is presented. Finally, in order to support this approach we report numerical tests with different values of the regularization parameter where the distributed force deforms the solid structure in order to minimize the objective functional of interest.

4.1 Mathematical model

In this section we introduce the mathematical formulation of the FSI problem and derive the optimality system. For our steady state FSI problem we consider the interaction of a Newtonian fluid, whose behavior is described by the Navier-Stokes equations, with a St. Venant-Kirchhoff material. The mathematical model in strong form of the FSI problem is then the following

$$\nabla \cdot \boldsymbol{v} = 0 \qquad \text{on } \Omega_f \,, \tag{4.1}$$

$$\rho_f(\boldsymbol{v} \cdot \nabla)\boldsymbol{v} - \nabla \cdot \boldsymbol{\sigma}_f = \mathbf{0} \qquad \text{on } \Omega_f \,, \tag{4.2}$$

$$\nabla \cdot \boldsymbol{\sigma}_s(\boldsymbol{\eta}) = \mathbf{f} \qquad \text{on } \Omega_s \,, \tag{4.3}$$

with $\boldsymbol{v}$ being the fluid velocity field and ρ_f its density. We denote with $\mathbf{f}$ the distributed force that acts exclusively in the solid sub-domain. The constitutive relations for the fluid stress tensor $\boldsymbol{\sigma}_f$ in the Newtonian incompressible case and for the solid Cauchy stress tensor $\boldsymbol{\sigma}_s$ read

$$\boldsymbol{\sigma}_f(p_f, \boldsymbol{v}_f) = -p_f\mathbf{I} + \mu_f(\nabla\boldsymbol{v} + \nabla\boldsymbol{v}^T) \,, \tag{4.4}$$

$$\boldsymbol{\sigma}_s(\boldsymbol{\eta}) = \lambda_s(\nabla \cdot \boldsymbol{\eta})\mathbf{I} + \mu_s(\nabla\boldsymbol{\eta} + \nabla\boldsymbol{\eta}^T) \,, \tag{4.5}$$

where p_f is the fluid pressure, μ_f the dynamic viscosity of the fluid while λ_s and μ_s are the solid Lamé parameters. In order to complete the system (4.1-4.3) it is necessary to define the following appropriate boundary and interface conditions, which are

$$\begin{aligned} \boldsymbol{v} &= \boldsymbol{v}_0 \quad \text{on } \Gamma_d^f, & \boldsymbol{\eta} &= \boldsymbol{\eta}_0 \quad \text{on } \Gamma_d^s \,, \\ \boldsymbol{\sigma}_f \cdot \mathbf{n}_f &= \mathbf{0} \quad \text{on } \Gamma_n^f, & \boldsymbol{\sigma}_s \cdot \mathbf{n}_s &= \mathbf{0} \quad \text{on } \Gamma_n^s \,, \\ \boldsymbol{\sigma}_f \cdot \mathbf{n}_f + \boldsymbol{\sigma}_s \cdot \mathbf{n}_s &= \mathbf{0} \quad \text{on } \Gamma_i, & \boldsymbol{v} &= \mathbf{0} \quad \text{on } \Gamma_i \,, \end{aligned} \tag{4.6}$$

where Γ_d^f and Γ_d^s are the surfaces where Dirichlet boundary conditions are imposed and Γ_n^f and Γ_n^s are the surfaces where standard homogeneous outflow boundary conditions are imposed for the fluid velocity and solid displacement, respectively. With Γ_i we denote the interface between the solid and fluid domain, $\Gamma_i = \partial\Omega_s \cap \partial\Omega_f$.

In order to recover a symmetric formulation of the optimality system that we are going to derive, we introduce the auxiliary mesh displacement $\widehat{\boldsymbol{\eta}}$ defined as

$$\nabla^2 \widehat{\boldsymbol{\eta}} = \mathbf{0} \qquad \mathbf{x} \in \Omega_s \,, \tag{4.7}$$

$$\widehat{\boldsymbol{\eta}} = \boldsymbol{\eta} \quad \text{on } \Gamma_i \;, \tag{4.8}$$

$$\widehat{\boldsymbol{\eta}} = \mathbf{0} \quad \text{on } (\partial\Omega_s - \Gamma_i) \,, \tag{4.9}$$

through which we extend the velocity field to the whole domain Ω, with τ positive and constant

$$\boldsymbol{v} = \begin{cases} \tau(\boldsymbol{\eta} - \widehat{\boldsymbol{\eta}}) & \text{on } \Omega_s, \\ \boldsymbol{v} & \text{solution of (4.1)-(4.2) on } \Omega_f. \end{cases} \tag{4.10}$$

It is clear that at steady state $\Omega_f(\boldsymbol{\eta}) = \Omega_f(\widehat{\boldsymbol{\eta}})$ and $\Omega_s(\boldsymbol{\eta}) = \Omega_s(\widehat{\boldsymbol{\eta}})$ with $\boldsymbol{v} = 0$ on the interface Γ_i. On the fluid-structure interface Γ_i we impose the (4.10) instead of (4.8), since it allows variation of the fields $\widehat{\boldsymbol{\eta}}$ and $\boldsymbol{\eta}$ even over the solid domain. With this notation we can write the following variational formulation of the FSI problem by integrating the strong form over the subdomains Ω_s or Ω_f and multiplying by the appropriate test function

$$\int_{\Omega_f} (\nabla \cdot \boldsymbol{v})\, \psi \, d\Omega \; = 0 \qquad\qquad \forall \psi \in L^2(\Omega_f) \,, \tag{4.11}$$

$$\int_{\Omega_f} \left[(\rho_f (\boldsymbol{v} \cdot \nabla)\boldsymbol{v}) \cdot \boldsymbol{\phi} - p \nabla \cdot \boldsymbol{\phi} + \mu_f \nabla \boldsymbol{v} : \nabla \boldsymbol{\phi} \right] \, d\Omega +$$

$$\int_{\Omega_s} \left[\lambda_s (\nabla \cdot \boldsymbol{\eta})(\nabla \cdot \boldsymbol{\phi}) + \mu_s \nabla \boldsymbol{\eta} : \nabla \boldsymbol{\phi} - \mathbf{f} \right] \, d\Omega + \tag{4.12}$$

$$\int_{\Gamma} [\mu_s (\boldsymbol{\nabla} \boldsymbol{\eta} \cdot \mathbf{n}_s) \cdot \boldsymbol{\phi} + \lambda_s (\boldsymbol{\nabla} \cdot \boldsymbol{\eta})(\mathbf{n}_s \cdot \boldsymbol{\phi})]] d\Gamma + \tag{4.13}$$

$$\int_{\Gamma} [[p \mathbf{n}_f - \mu_f (\boldsymbol{\nabla} \boldsymbol{v} \cdot \mathbf{n}_f) \cdot \boldsymbol{\phi}] = 0 \qquad \forall \boldsymbol{\phi} \in \mathbf{H}^1_{\Gamma^s_d}(\Omega) \cap \mathbf{H}^1_{\Gamma^f_d}(\Omega) \,,$$

$$\int_{\Omega_s(\widehat{\boldsymbol{\eta}})} \nabla \widehat{\boldsymbol{\eta}} : \nabla \widehat{\boldsymbol{\eta}}_a \, d\Omega = 0 \qquad\qquad \forall \, \widehat{\boldsymbol{\eta}}_a \in \mathbf{H}^1_{\Gamma_s}(\Omega_s) \,, \tag{4.14}$$

$$\int_{\Omega_s(\widehat{\boldsymbol{\eta}})} (\boldsymbol{v} - \tau(\boldsymbol{\eta} - \widehat{\boldsymbol{\eta}})) \cdot \boldsymbol{\beta}_a \, d\Omega = 0 \qquad\qquad \forall \boldsymbol{\beta}_a \in \mathbf{L}^2_{\Gamma_s}(\Omega_s) \,. \tag{4.15}$$

The surface integrals on Γ vanish due to the boundary and interface conditions (4.6).

4.1.1 Optimality system

In this work we study two different matching profile problems by using a distributed force that moves and deforms the solid. We consider either a fluid velocity or a solid displacement matching problem by introducing the following objective functional

$$\mathcal{J}(\boldsymbol{v},\boldsymbol{\eta},\mathbf{f}) = \frac{a}{2}\int_{\Omega_d} \omega||\boldsymbol{v}-\boldsymbol{v}_d||^2 d\Omega + \frac{b}{2}\int_{\Omega_d} \omega||\boldsymbol{\eta}-\boldsymbol{\eta}_d||^2 d\Omega + \frac{\beta}{2}\int_{\Omega_c} ||\mathbf{f}||^2 d\Omega\,, \tag{4.16}$$

where $\boldsymbol{v}_d$ and $\boldsymbol{\eta}_d$ are the desired velocity and displacement on the controlled domain region $\Omega_d \subset \Omega_f$ or $\Omega_d \subset \Omega_s$, respectively. The weight function ω of the coordinates $\mathbf{x}$ can be used to give more importance to some parts of Ω_d. When $b = 0$ the objective functional gives a velocity matching problem, while for $a = 0$ a displacement matching problem is defined. The functional is completed with a regularization term which is needed to obtain a control function $\mathbf{f}$ in the space of square integrable functions $L^2(\Omega_c)$, with Ω_c being the solid region where the control can act. The regularization parameter β plays a fundamental role for the numerical solution of the minimization problem. If a too high value of β is chosen the regularization contribution dominates over the objective one and the objective cannot be achieved well, while a lack of regularization can lead to singular solutions or convergence issues in the numerical solution of the problem.

The first step towards the optimality system consists of writing the full Lagrangian of the problem, which is composed of the functional (4.16) and state equations (4.11-4.15) multiplied by the appropriate Lagrangian multipliers, the so-called *adjoint variables*. By doing so we transform a constrained minimization problem into an unconstrained one.

$$\begin{aligned}\mathcal{L}(p,\boldsymbol{v},\boldsymbol{\eta},\widehat{\boldsymbol{\eta}},p_a,\boldsymbol{v}_a,\widehat{\boldsymbol{\eta}}_a,\widehat{\mathbf{s}}_a,\beta_a) &= \mathcal{J}(\boldsymbol{\eta},p_c) + \int_{\Omega_f} (\nabla\cdot\boldsymbol{v})\, p_a \, d\Omega \\ &+ \int_{\Omega_f} [\rho_f(\boldsymbol{v}\cdot\nabla)\boldsymbol{v} + \nabla p - \nabla\cdot(\mu_f\nabla\boldsymbol{v})]\cdot\boldsymbol{v}_a \, d\Omega \\ &+ \int_{\Omega_s} [-\nabla\cdot(\mu_s\nabla\boldsymbol{\eta} + \lambda_s\mathbf{I}(\nabla\cdot\boldsymbol{\eta})) - \mathbf{f}]\cdot\boldsymbol{v}_a\, d\Omega + \int_{\Omega_s} \nabla^2\widehat{\boldsymbol{\eta}}\cdot\widehat{\boldsymbol{\eta}}_a\, d\Omega \\ &+ \int_{\Gamma_i} \widehat{\mathbf{s}}_a\cdot\left[(\widehat{\boldsymbol{\eta}}-\boldsymbol{\eta}) + \frac{\boldsymbol{v}}{\tau}\right] d\Gamma + \int_{\Omega_s} \boldsymbol{\beta}_a\cdot[\boldsymbol{v} - \tau(\boldsymbol{\eta}-\widehat{\boldsymbol{\eta}})]\, d\Omega\,.\end{aligned} \tag{4.17}$$

In order to derive the optimality system we impose the first order necessary condition

$$\delta\mathcal{L} = 0\,. \tag{4.18}$$

In the following we use notation δq for the variation of the generic function q and $(D\mathcal{L}/Dq)\delta q$ for the Fréchet derivative of functional $\mathcal{L}$ in the direction δq. We recall that the shape derivatives of a functional F on a moving domain with velocity $\delta\boldsymbol{v}$ are given by

$$\frac{dF}{d\Omega(\widehat{\boldsymbol{\eta}})}\delta\boldsymbol{v} = \int_{\partial\Omega(\widehat{\boldsymbol{\eta}})} y\delta\boldsymbol{v}\cdot\mathbf{n}\,d\Gamma\,, \tag{4.19}$$

$$\frac{dF}{d\Gamma(\widehat{\boldsymbol{\eta}})}\delta\boldsymbol{v} = \int_{\Gamma(\widehat{\boldsymbol{\eta}})} (\nabla_n + \chi)\,y\delta\boldsymbol{v}\cdot\mathbf{n}\,d\Gamma\,, \tag{4.20}$$

where ∇_n is the normal derivative operator and χ the mean curvature of Γ, see [54]. From the above definitions it is clear that the shape derivatives terms vanish if the integrated function is zero on the integration domain (i.e. the boundary).

The first order necessary condition (4.18) implies that the total variation of the Lagrangian has to vanish. Since each variation is independent from the others then each variation has to be zero. When taking the Fréchet derivatives of the Lagrangian (4.17) with respect to the adjoint variables $(p_a, \boldsymbol{v}_a, \widehat{\boldsymbol{\eta}_a}, \boldsymbol{\beta}_a)$ we recover the weak form of the state system (4.1-4.3), together with the appropriate boundary and interface conditions. When we focus on the variations of the state variables $(\boldsymbol{v}, p, \boldsymbol{\eta}, \widehat{\boldsymbol{\eta}})$ we obtain the weak form of the adjoint system. The equation of the variations $\delta\boldsymbol{\eta}$ reads

$$\frac{D\mathcal{L}}{D\boldsymbol{\eta}}\delta\boldsymbol{\eta} = b\int_{\Omega_d}\omega(\boldsymbol{\eta}-\boldsymbol{\eta}_d)\delta\boldsymbol{\eta}\,d\Omega + \int_{\Omega_s}\left[\mu_s\nabla\delta\boldsymbol{\eta} : \nabla\boldsymbol{v}_a + \lambda_s(\nabla\cdot\delta\boldsymbol{\eta})(\nabla\cdot\boldsymbol{v}_a)\right]d\Omega$$
$$-\,\tau\int_{\Omega_s}\delta\boldsymbol{\eta}\cdot\boldsymbol{\beta}_a\,d\Omega - \int_{\Gamma_i}\widehat{\mathbf{s}}_a\cdot\delta\boldsymbol{\eta}\,d\Gamma = 0 \qquad \forall\delta\boldsymbol{\eta}\in\mathbf{H}^1_{\Gamma^s_d}(\Omega_s)\,. \tag{4.21}$$

By performing integration by parts on the term where the variation $\delta\boldsymbol{\eta}$ is differentiated we obtain the following values of $\boldsymbol{\beta}_a$ and $\widehat{\mathbf{s}}_a$

$$\boldsymbol{\beta}_a = -\frac{1}{\tau}\nabla\cdot\left[\mu_s\nabla\boldsymbol{v}_a + \lambda_s\mathbf{I}(\nabla\cdot\boldsymbol{v}_a)\right] + \frac{b\omega}{\tau}(\boldsymbol{\eta}-\boldsymbol{\eta}_d)\,, \tag{4.22}$$

$$\widehat{\mathbf{s}}_a = \left[\mu_s\nabla\boldsymbol{v}_a + \lambda_s\mathbf{I}(\nabla\cdot\boldsymbol{v}_a)\right]\cdot\mathbf{n}\,. \tag{4.23}$$

We now collect all the terms with $\delta\boldsymbol{v}$ obtaining

$$\frac{D\mathcal{L}}{D\boldsymbol{v}}\delta\boldsymbol{v} = \int_{\Omega_f} (\nabla\cdot\delta\boldsymbol{v})\,p_a\,d\Omega + \int_{\Omega_s} \delta\boldsymbol{v}\cdot\boldsymbol{\beta}_a\,d\Omega + \frac{1}{\tau}\int_{\Gamma_i} \delta\boldsymbol{v}\cdot\widehat{\mathbf{s}}_a\,d\Gamma + \tag{4.24}$$

$$\int_{\Omega_f} \Big[(\rho_f(\delta\boldsymbol{v}\cdot\nabla)\boldsymbol{v}) + (\rho_f(\boldsymbol{v}\cdot\nabla)\delta\boldsymbol{v}) - \nabla\cdot(\mu_f\nabla\delta\boldsymbol{v})\Big]\cdot\boldsymbol{v}_a\,d\Omega +$$

$$\int_{\Omega_d} a\omega(\boldsymbol{v}-\boldsymbol{v}_d)\delta\boldsymbol{v}\,d\Omega + \int_{\Omega_d} b\omega(\boldsymbol{\eta}-\boldsymbol{\eta}_d)\delta\boldsymbol{v}\,d\Omega +$$

$$\int_{\partial\Omega_f} (\nabla\cdot\boldsymbol{v})\,p_a\,\delta\boldsymbol{v}\cdot\mathbf{n}\,d\Gamma + \int_{\partial\Omega_d} \omega\frac{b(\boldsymbol{\eta}-\boldsymbol{\eta}_d)^2 + a(\boldsymbol{v}-\boldsymbol{v}_d)^2}{2}\delta\boldsymbol{v}\cdot\mathbf{n}\,d\Omega +$$

$$\int_{\partial\Omega_f} \boldsymbol{v}_a\cdot\Big[\rho_f(\boldsymbol{v}\cdot\nabla)\boldsymbol{v} + \nabla p - \nabla\cdot(\mu_f\nabla\boldsymbol{v})\Big]\delta\boldsymbol{v}\cdot\mathbf{n}\,d\Gamma + \tag{4.25}$$

$$\int_{\partial\Omega_s} \boldsymbol{v}_a\cdot\Big[-\nabla\cdot(\mu_s\nabla\boldsymbol{\eta} + \lambda_s\mathbf{I}(\nabla\cdot\boldsymbol{\eta})) - \mathbf{f}\Big]\delta\boldsymbol{v}\cdot\mathbf{n}\;d\Gamma +$$

$$\int_{\partial\Omega_s} (\nabla^2\widehat{\boldsymbol{\eta}}\cdot\widehat{\boldsymbol{\eta}}_a)\,\delta\boldsymbol{v}\cdot\mathbf{n}\,d\Gamma + \int_{\Gamma_i} (\nabla_n + \chi)\,\Big[\widehat{\mathbf{s}}_a\cdot\Big[(\widehat{\boldsymbol{\eta}}-\boldsymbol{\eta}) + \frac{\boldsymbol{v}}{\tau}\Big]\Big]\;\delta\boldsymbol{v}\cdot\mathbf{n}\,d\Gamma +$$

$$\int_{\partial\Omega_s} \boldsymbol{\beta}_a\cdot[\boldsymbol{v} - \tau(\boldsymbol{\eta}-\widehat{\boldsymbol{\eta}})]\;\delta\boldsymbol{v}\cdot\mathbf{n}\,d\Gamma = 0 \qquad \forall\delta\boldsymbol{v}\in\mathbf{H}^1_{\Gamma_d^f\cap\Gamma_d^s}(\Omega)\,.$$

The surface terms integrated on $\partial\Omega_s$ and $\partial\Omega_f$ can be simplified since the integrated functions are equal to zero on those surfaces. The terms integrated on $\partial\Omega_d$ vanish as well, since we can take an arbitrary weight function ω that vanishes on $\partial\Omega_d$. Finally, the term referring to the interface shape derivative vanishes due to the (4.10).

By collecting the remaining terms with $\delta\boldsymbol{v}$ we obtain

$$\int_{\Omega_f} (\nabla\cdot\delta\boldsymbol{v})p_a d\Omega + \int_{\Omega_s} \delta\boldsymbol{v}\cdot\boldsymbol{\beta}_a d\Omega + \frac{1}{\tau}\int_{\Gamma_i} \delta\boldsymbol{v}\cdot\widehat{\mathbf{s}}_a d\Gamma + a\int_{\Omega_d} \omega(\boldsymbol{v}-\boldsymbol{v}_d)\delta\boldsymbol{v}d\Omega +$$

$$\int_{\Omega_f} \Big[(\rho_f(\delta\boldsymbol{v}\cdot\nabla)\boldsymbol{v})\cdot\boldsymbol{v}_a + (\rho_f(\boldsymbol{v}\cdot\nabla)\delta\boldsymbol{v})\cdot\boldsymbol{v}_a - \nabla\cdot(\mu_f\nabla\delta\boldsymbol{v})\cdot\boldsymbol{v}_a\Big]\,d\Omega = 0$$

$$\forall\delta\boldsymbol{v}\in\mathbf{H}^1_{\Gamma_d^f\cap\Gamma_d^s}(\Omega)\,. \tag{4.26}$$

By using (4.22-4.23) the (4.26) becomes

$$\int_{\Omega_f} (\nabla\cdot\delta\boldsymbol{v})\,p_a\,d\Omega + \frac{1}{\tau}\int_{\Omega_s} [\mu_s\nabla\boldsymbol{v}_a : \nabla\delta\boldsymbol{v} + \lambda_s(\nabla\cdot\boldsymbol{v}_a)(\nabla\cdot\delta\boldsymbol{v})]\;d\Omega + \tag{4.27}$$

$$\int_{\Omega_f} \Big[(\rho_f(\delta\boldsymbol{v}\cdot\nabla)\boldsymbol{v})\cdot\boldsymbol{v}_a + (\rho_f(\boldsymbol{v}\cdot\nabla)\delta\boldsymbol{v})\cdot\boldsymbol{v}_a - \nabla\cdot(\mu_f\nabla\delta\boldsymbol{v})\cdot\boldsymbol{v}_a\Big]\,d\Omega +$$

$$\frac{b}{\tau}\int_{\Omega_d} \omega(\boldsymbol{\eta}-\boldsymbol{\eta}_d)\delta\boldsymbol{v}\,d\Omega + a\int_{\Omega_d} \omega(\boldsymbol{v}-\boldsymbol{v}_d)\delta\boldsymbol{v}\,d\Omega = 0 \qquad \forall\delta\boldsymbol{v}\in\mathbf{H}^1_{\Gamma_d^f\cap\Gamma_d^s}(\Omega)\,.$$

Collecting $\delta\widehat{\boldsymbol{\eta}}$ we obtain

$$\frac{D\mathcal{L}}{D\widehat{\boldsymbol{\eta}}}\delta\widehat{\boldsymbol{\eta}} = \int_{\Omega_s} \nabla\delta\widehat{\boldsymbol{\eta}} : \nabla\widehat{\boldsymbol{\eta}}_a \, d\Omega + \tau \int_{\Omega_s} \delta\widehat{\boldsymbol{\eta}} \cdot \boldsymbol{\beta}_a \, d\Omega + \int_{\Gamma_i} \widehat{\mathbf{s}}_a \cdot \delta\widehat{\boldsymbol{\eta}} \, d\Gamma = 0 \quad \forall\delta\widehat{\boldsymbol{\eta}} \in \mathbf{H}^1_{\Gamma^s_d}(\Omega_s)\,. \tag{4.28}$$

With (4.22-4.23) the (4.28) reads

$$\int_{\Omega_s} \nabla\widehat{\boldsymbol{\eta}}_a : \nabla\delta\widehat{\boldsymbol{\eta}} \, d\Omega = -\int_{\Omega_s} \left[\mu_s \nabla\boldsymbol{v}_a : \nabla\delta\widehat{\boldsymbol{\eta}} + \lambda_s(\nabla\cdot\boldsymbol{v}_a)(\nabla\cdot\delta\widehat{\boldsymbol{\eta}})\right] d\Omega + b\int_{\Omega_d} \omega(\boldsymbol{\eta} - \boldsymbol{\eta}_d)\delta\widehat{\boldsymbol{\eta}} \, d\Omega \qquad \forall\delta\widehat{\boldsymbol{\eta}} \in \mathbf{H}^1_{\Gamma^s}(\Omega_s)\,. \tag{4.29}$$

When we set to zero the Fréchet derivatives taken with respect to the pressure we obtain

$$\frac{D\mathcal{L}}{Dp}\delta p = \int_{\Omega_f} (\nabla\cdot\boldsymbol{v}_a)\delta p \; d\Omega = 0 \qquad \forall\delta p \in L^2(\Omega)\,. \tag{4.30}$$

Finally, when considering the Fréchet derivatives of the Lagrangian (4.17) with respect to the control parameter $\mathbf{f}$ we obtain the control equation

$$\frac{D\mathcal{L}}{D\mathbf{f}}\delta\mathbf{f} = \int_{\Omega_c} (-\beta\mathbf{f} + \boldsymbol{v}_a)\delta\mathbf{f} \, d\Omega = 0\,. \tag{4.31}$$

The distributed control is proportional to the adjoint velocity by the regularization parameter β, namely $\mathbf{f} = \boldsymbol{v}_a/\beta$. We now collect the contributions obtained and write the following weak form of the adjoint system

$$\int_{\Omega_f} (\nabla\cdot\boldsymbol{v}_a)\delta p \, d\Omega = 0 \qquad \forall\,\delta p \in L^2(\Omega_f)\,, \tag{4.32}$$

$$\begin{aligned}
&\int_{\Omega_f} \left[\big(\rho^f(\delta\boldsymbol{v}\cdot\nabla)\boldsymbol{v}\big)\cdot\boldsymbol{v}_a + \big(\rho^f(\boldsymbol{v}\cdot\nabla)\delta\boldsymbol{v}\big)\cdot\boldsymbol{v}_a + \mu^f\nabla\delta\boldsymbol{v} : \nabla\boldsymbol{v}_a\right] d\Omega + \qquad (4.33)\\
&+\frac{1}{\tau}\int_{\Omega^s} \left[\mu_s \boldsymbol{\nabla}\boldsymbol{v}_a : \boldsymbol{\nabla}\delta\boldsymbol{v} + \lambda_s(\boldsymbol{\nabla}\cdot\boldsymbol{v}_a)(\boldsymbol{\nabla}\cdot\delta\boldsymbol{v})\right] d\Omega + \int_{\Omega_f} (\nabla\cdot\delta\boldsymbol{v})p_a \, d\Omega\\
&+\frac{b}{\tau}\int_{\Omega_d} \omega(\boldsymbol{\eta} - \boldsymbol{\eta}_d)\delta\boldsymbol{v} \, d\Omega + a\int_{\Omega_d} \omega(\boldsymbol{v} - \boldsymbol{v}_d)\delta\boldsymbol{v} \, d\Omega = 0 \quad \forall\delta\boldsymbol{v} \in H^1_{\Gamma_{fd}\cup\Gamma_{sd}}(\Omega)\,,
\end{aligned}$$

$$\int_{\Omega_s} \nabla\widehat{\boldsymbol{\eta}}_a : \nabla\,\delta\widehat{\boldsymbol{\eta}} \, d\Omega + \int_{\Omega_s} \mu^s\nabla\boldsymbol{v}_a : \nabla\delta\widehat{\boldsymbol{\eta}} \, d\Omega = 0 \qquad \forall\delta\widehat{\boldsymbol{\eta}} \in H^1_{\Gamma_{sd}}(\Omega_s)\,. \tag{4.34}$$

The equation for the adjoint displacement $\boldsymbol{\eta}_a$ has been neglected since we do not need the adjoint displacement to determine the force $\mathbf{f}$.

By performing integration by parts on the system (4.32-4.34) it is possible to determine the strong form of the adjoint system together with the boundary conditions for the adjoint variables. After performing the integration by parts, we recover the adjoint state $(\boldsymbol{v}_a^f, \boldsymbol{v}_a^s, p_a) \in \mathbf{H}^1_{\partial\Omega^f - \Gamma_i}(\Omega^f) \cap \mathbf{H}^2(\Omega^f) \times \mathbf{H}^1_{\partial\Omega^s - \Gamma_i}(\Omega^s) \cap \mathbf{H}^2(\Omega^s) \times L^2_0(\Omega^f) \cap \mathbf{H}^1(\Omega^f)$, by solving

$$\begin{aligned} &\boldsymbol{\nabla} \cdot \boldsymbol{v}_a^f = 0\,, && (4.35)\\ &-\rho_l (\boldsymbol{\nabla} \boldsymbol{v})^T \boldsymbol{v}_a^f + \rho_l [(\boldsymbol{v} \cdot \boldsymbol{\nabla}) \boldsymbol{v}_a^f] + \boldsymbol{\nabla} p_a - \boldsymbol{\nabla} \cdot (\mu_l \boldsymbol{\nabla} \boldsymbol{v}_a^f) = \\ &\qquad a\omega(\boldsymbol{v} - \boldsymbol{v}_d) + b\frac{\omega}{\tau}(\boldsymbol{\eta} - \boldsymbol{\eta}_d)\,, && (4.36)\\ &\boldsymbol{\nabla} \cdot \boldsymbol{\sigma}_s(\boldsymbol{v}_a^s) = 0\,. && (4.37) \end{aligned}$$

with boundary conditions defined as

$$\begin{aligned} &\boldsymbol{v}_a^s = \boldsymbol{v}_a^f && \text{on } \Gamma_i\,, \\ &\boldsymbol{\sigma}_s(\boldsymbol{v}_a^s) \cdot \mathbf{n} = \boldsymbol{\sigma}_f(\boldsymbol{v}_a^f) \cdot \mathbf{n} && \text{on } \Gamma_i\,, \\ &\mu_f (\nabla \boldsymbol{v}_a) \cdot \mathbf{n} = -(\boldsymbol{v} \cdot \mathbf{n})\, \boldsymbol{v}_a\,,\ \ p_a = 0 && \text{on } \Gamma_n^f\,, \\ &\boldsymbol{v}_a = 0 && \text{on } \Gamma_{fd} \cup \Gamma_{sd}\,. \end{aligned} \qquad (4.38)$$

The optimality system is then composed by the state (4.11-4.15) and adjoint (4.32-4.34) systems coupled with the control equation (4.31).

4.2 Numerical implementation and tests

Due to the strong non-linearity of the problem a one-shot solution of the optimal system can not be performed. In this work we use a segregated approach for the solution of the optimality system where we solve the state system, the adjoint system and the control equation separately and iteratively, see for example [16]. By doing so we can also use the same solver to compute both the adjoint and state systems with only minimal modifications. The iterative algorithm used to minimize the objective functional is the simple *Steepest Descent method* described in Algorithm 4.

The algorithm starts by solving the state system (4.11-4.15) with no control in order to obtain the solution of the reference case $(\boldsymbol{v}^0, p^0, \boldsymbol{\eta}^0)$. Then the gradient direction is obtained from the solution of the adjoint equations (4.31), where $\boldsymbol{v}_a$ is known once that the adjoint system (4.32-4.34) has been solved. The core of the algorithm consists of the backtracking line search process, where the state system is solved iteratively, reducing the value of

Algorithm 4 Description of the Steepest Descent algorithm.

```
1. Set a state $(\boldsymbol{v}^0, p^0, \boldsymbol{\eta}^0)$ satisfying (4.11-4.15)   ▷ Setup of the state - Reference case
2. Compute the functional $\mathcal{J}^0$ in (4.16)
3. Set $r^0 = 1$
for $i = 1 \rightarrow i_{max}$ do
    4. Solve the system (4.32)-(4.34) to obtain the adjoint state $(\boldsymbol{v}_a^i, p_a^i)$
    5. Set the control update $\delta\mathbf{f}^i = (\mathbf{f}^{i-1} - \boldsymbol{v}_a^i/\beta)$
    6. Set $r^i = r^0$
    while $\mathcal{J}^i(\mathbf{f}^{i-1} + r^i\delta\mathbf{f}^i) > \mathcal{J}^{i-1}(\mathbf{f}^{i-1})$ do   ▷ Line search
        7. Set $r^i = \rho\, r^i$
        8. Solve (4.11-4.15) for the state $(\boldsymbol{v}^i, \mathbf{f}^i, \boldsymbol{\eta}^i)$ with $\mathbf{f}^i = \mathbf{f}^{i-1} + r^i\delta\mathbf{f}^i$
        if $r^i < toll$ then
            Line search not successful   ▷ End of the algorithm
        end if
    end while
    if $||\mathcal{J}^i(\mathbf{f}^{i-1} + r^i\delta\mathbf{f}^i) - \mathcal{J}^{i-1}(\mathbf{f}^{i-1})||/\mathcal{J}^{i-1}(\mathbf{f}^{i-1}) < \tau$ then
        9. Convergence reached   ▷ End of the algorithm
    end if
end for
```

the control parameters by a contraction factor ρ until a functional reduction is obtained. We set $\rho = 0.7$. The step length r determines how far from the current state solution we are moving along the gradient direction, which is given by $\delta\mathbf{f}$. This algorithm comes to an end either when two consecutively computed functionals are almost equal and no further improvements can be achieved or when r becomes lower than a tolerance value $toll = 10^{-7}$.

This algorithm requires several solutions of the state and adjoint systems in order to find the optimal control, however it does not need a great amount of memory which is similar to a standard, direct FSI simulation. We implemented this algorithm in our in-house finite element code FEMuS, available at [1], which works on multiprocessor architectures with openMPI libraries, uses a multigrid solver with mesh-moving capability and PETSc libraries for the solution of the linear systems. We use standard quadratic-linear elements for all the variables except the pressure that is assumed linear to satisfy the *BBL inf-sup* condition. The displacements are approximated with standard quadratic elements.

4.2.1 Test 1. Velocity matching

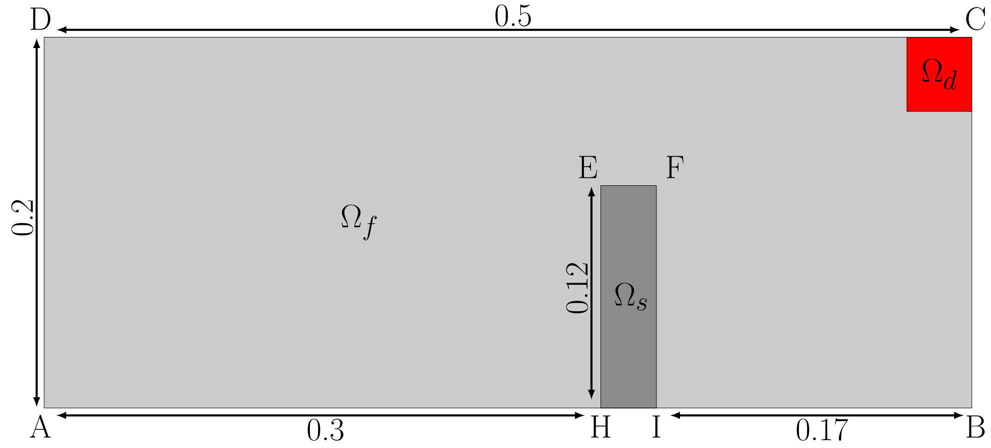

Figure 4.1: Case study. Domain overview with the solid region (Ω_s), the fluid region (Ω_f) and the controlled region (Ω_d).

In this section we present the results obtained by applying Algorithm 4 to a two-dimensional test case. In Figure 4.1 we report the domain considered with the geometrical properties. The origin of the reference system is the bottom left corner (point A). The solid region Ω_s is colored with darker gray while the fluid region Ω_f with lighter gray. The fluid controlled region $\Omega_d = [0.465, 0.5]m \times [0.16, 0.2]m$, which is located near the channel exit, is shown in red. We impose pressure boundary conditions with vanishing tangential velocity on the left and right surfaces, $p_{AD} = 10000Pa$ and $p_{BC} = 9750Pa$, respectively. On the lower boundary AB we prescribe a no-slip condition, while the upper surface CD is a symmetry axis and we set a homogeneous Neumann boundary condition for all the state and adjoint variables apart from u_y and u_{ay} that vanish. All the boundaries are fixed with the exception of the interface Γ_i, that may move with fixed endpoints H and I. The physical properties are $\rho_s = \rho_l = 1000kg/m^3$ with $\mu_l/\rho_l = 0.07Pa\, m^3 s/kg$ and $\mu_s = 76250Pa$ so that the flow is not turbulent and the solid can bend easily. The Young modulus E_s and Poisson coefficient ξ are equal to $183000Pa$ and $\xi = 0.2$, respectively.

According to Algorithm 4, we start solving the state system (4.11-4.15) assuming $\mathbf{f} = 0$ in order to obtain the reference case, which is reported in Figure 4.2. The velocity profile is reported on the top of this Figure, while on the bottom the pressure field with iso-lines is shown. Since the solid obstacle

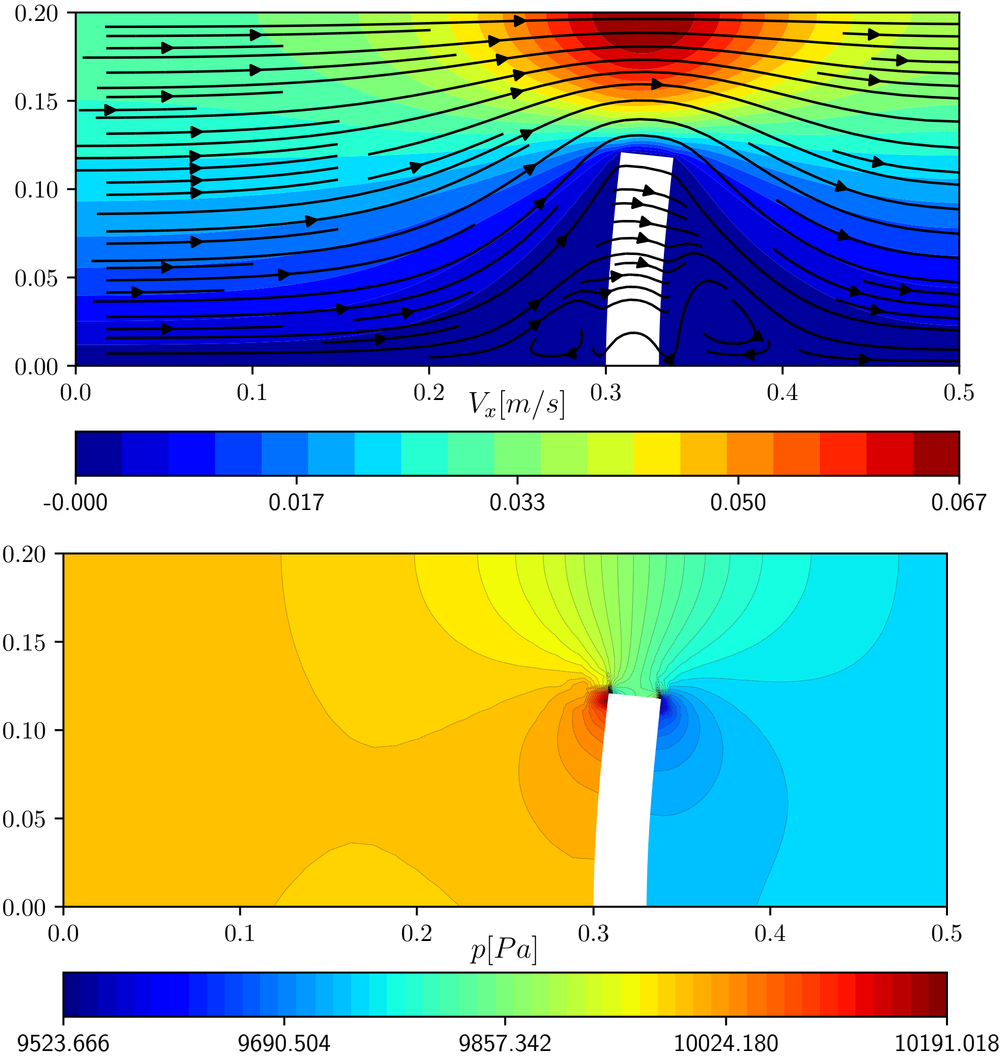

Figure 4.2: Reference geometry with velocity (m/s) profile in the fluid region (on the top). Pressure (Pa) profile and iso-lines in the fluid region (on the bottom).

reduces the fluid domain cross section the fluid has to accelerate to satisfy the mass conservation equation. Furthermore, the solid object is responsible for the majority of the pressure losses as it can be seen on the bottom of Figure 4.2.

Our optimal control problem consists in finding the optimal solid deformation so that the axial component of the velocity (v_x) matches a desired profile over the controlled domain Ω_d. The solid is deformed by a distributed force $\mathbf{f}$ which is the control parameter acting in the whole solid domain, see

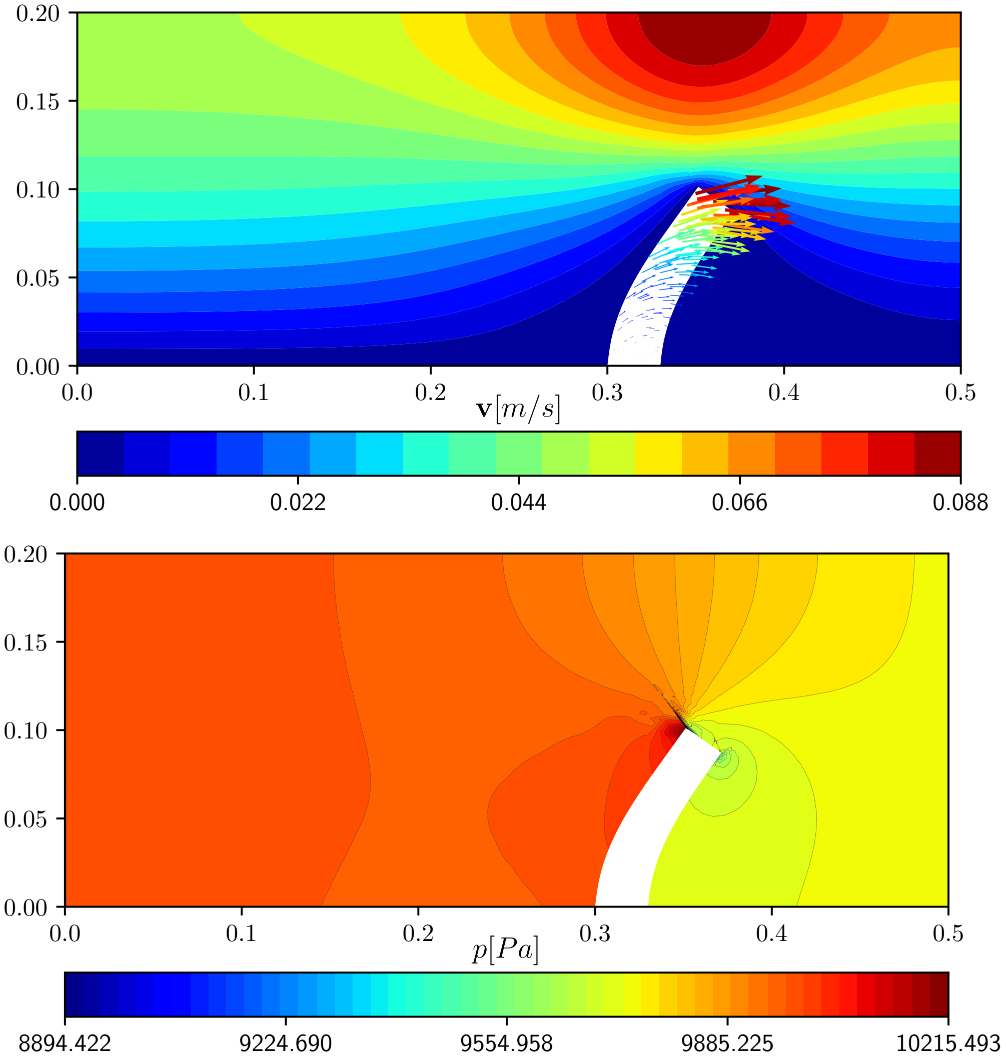

Figure 4.3: Velocity (m/s) profile in the fluid region and force (N) vectors (on the top), $\beta = 10^{-9}$. Pressure (Pa) field and iso-lines in the fluid region (on the bottom), $\beta = 10^{-9}$.

(4.3). In the reference case with no control we obtain a mean value of v_x over Ω_d equal to $\bar{v}_x = 0.037\ m/s$. We then choose a constant target value $v_{xd} = 0.065\ m/s$ in the whole controlled domain, thus requiring a higher fluid velocity near the channel outlet. The objective functional becomes

$$\mathcal{J}(v_x, \mathbf{f}) = \frac{1}{2}\int_{\Omega_d} \omega (v_x - 0.065)^2 d\Omega + \frac{1}{2}\beta \int_{\Omega_s} ||\mathbf{f}||^2 d\Omega\,, \tag{4.39}$$

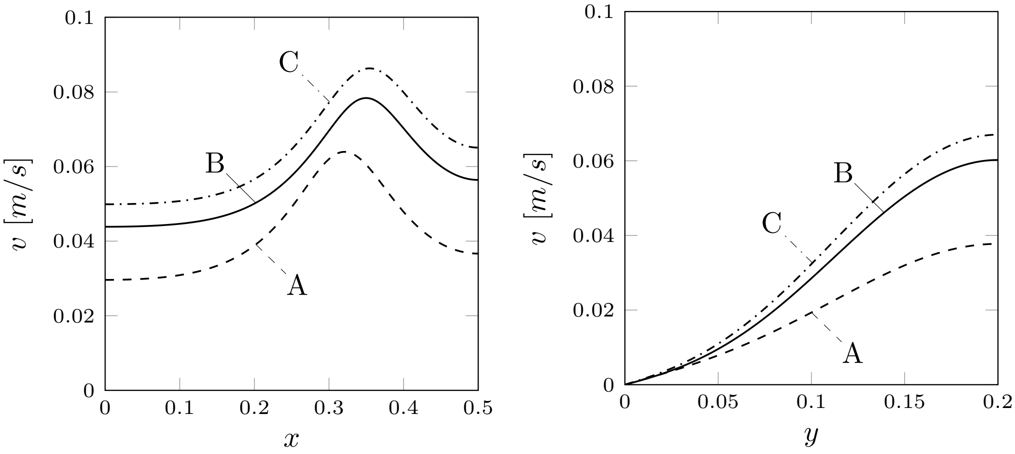

Figure 4.4: On the left axial velocity u_x, profile on a line at $x = 0.49m$. On the right u_x on a line at $y = 0.18m$. Result (A) obtained with no control, (B) with $\beta = 10^{-7}$ and (C) with $\beta = 10^{-9}$.

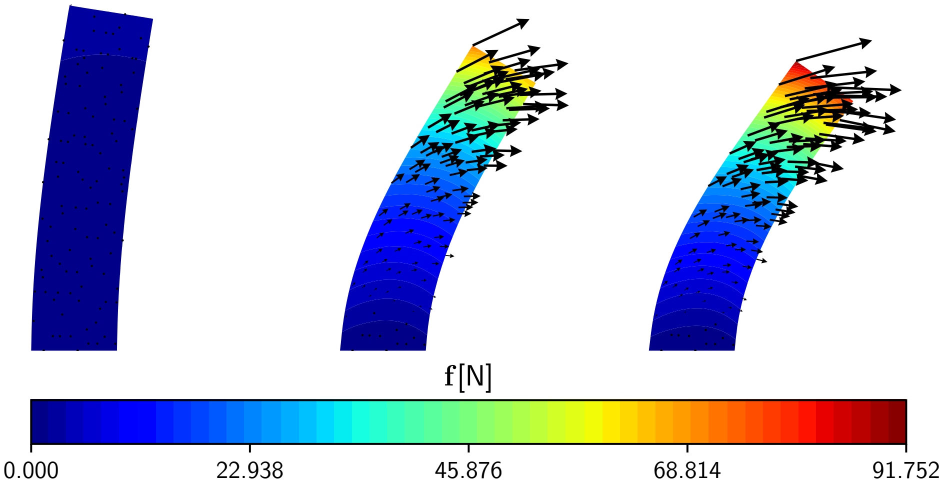

Figure 4.5: Force vectors in black and magnitude in colors on the solid domain for $\beta = 10^{-5}$, 10^{-7}, 10^{-9} from left to right.

in which we set

$$\omega = \begin{cases} 1 & \mathbf{x} \in \Omega_d, \\ 0 & \text{otherwise.} \end{cases}$$

Once the reference case is set up it is possible to solve the optimality system with the technique described in Algorithm 4.

We now report the results obtained for different values of the regularization parameter $\beta = 10^{-5}$, 10^{-7}, 10^{-9}. On the top of Figure 4.3 we report the

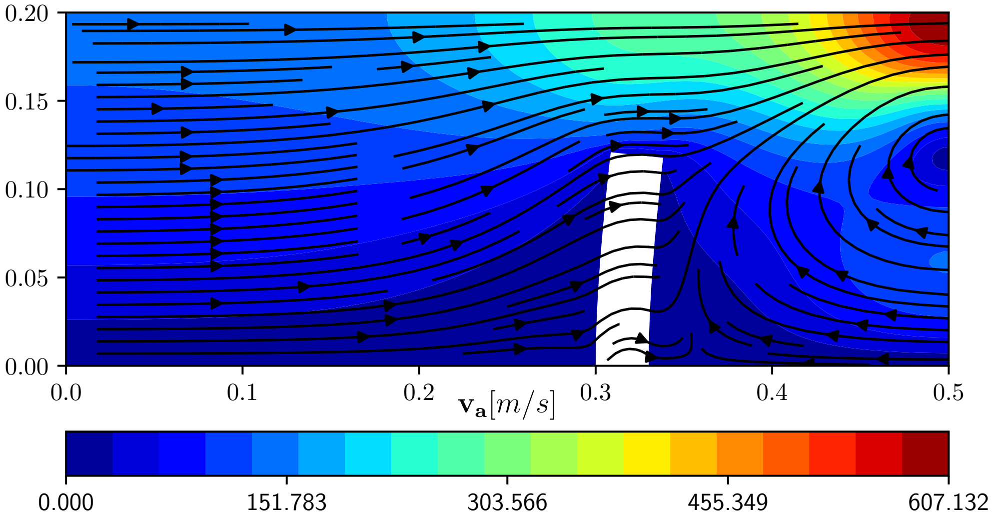

Figure 4.6: Adjoint velocity profile and vectors in the fluid domain, $\beta = 10^{-9}$.

velocity profile and the force acting in the solid domain, and on the bottom of the same Figure the pressure profile is shown. The force bends the solid to the right so that the channel cross section becomes larger than that of the reference case. Since the total pressure drop between the channel inlet and outlet is fixed by the boundary conditions ($250Pa$), if the pressure losses induced by the obstacle decrease then the fluid velocity has to increase. In particular it is worth noticing that, due to the regularization term in (4.39), it is more effective to apply an intense force near the tip of the solid rather than a weaker one largely distributed. In Figure 4.4 the axial component of the velocity field, v_x, is shown on a vertical line at $x = 0.49m$ on the left and on a horizontal one at $y = 0.18m$ on the right, for different values of the regularization β. Both lines cross the controlled region Ω_d. By reducing the value of β the control can act more strongly and the velocity is higher than that of the reference case. In Figure 4.5 the control force is reported for different amount of regularization. The force acting on the solid is very small in the case $\beta = 10^{-5}$, while becomes more relevant when reducing β, leading to a higher solid deformation. The adjoint velocity profile is reported in Figure 4.6 with arrows and colors related to the $\boldsymbol{v}_a$ magnitude. It can be easily verified that the source term of the adjoint velocity, which is the difference between the actual and the desired velocity, is located in the top right corner Ω_d.

Finally, in Table 4.1 we report the functionals and the average axial ve-

Table 4.1: Objective functionals $\mathcal{J}$ and average x-velocity over the controlled region Ω_d computed with no control ($\beta = \infty$) and different β values.

β	∞	10^{-5}	10^{-7}	10^{-9}
$\mathcal{J}(\boldsymbol{v}) \cdot 10^8$	113.69	111.68	32.75	1.10
$\bar{v}_x\ [m/s]$	0.0367	0.0375	0.0584	0.0651

locity over the controlled region as computed in the reference and in the controlled case with different β. The functional is reduced in every case and in particular with $\beta = 10^{-9}$, where the axial velocity is very close to the desired value $0.065 m/s$.

4.2.2 Test 2. Displacement matching

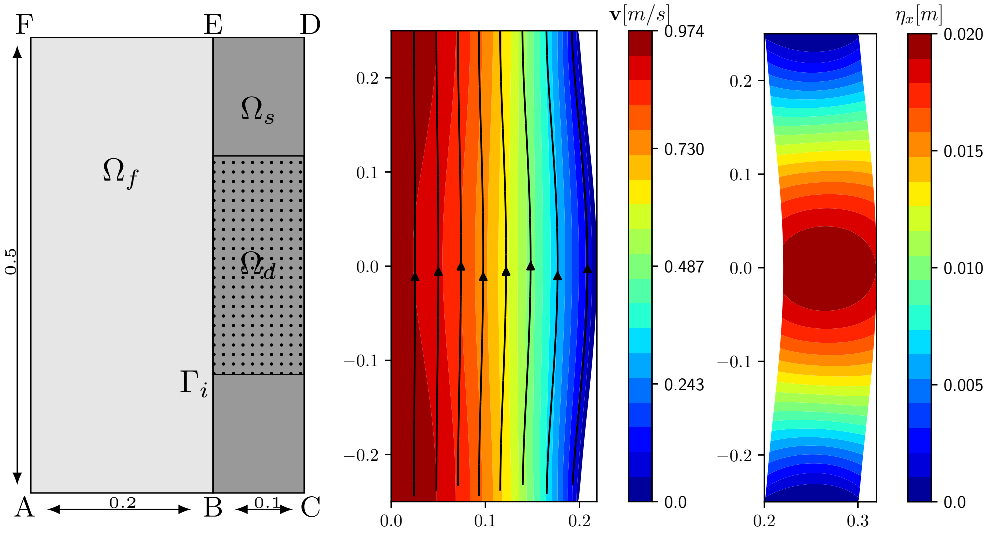

Figure 4.7: Geometry and controlled region defined by dotted square on the right Ω_d (left). Reference case with velocity profiles and streamlines in the liquid (middle). Solid displacement field η_x for the same reference configuration (right).

With this test case we study now a solid displacement matching profile, where the control is again a distributed force acting on the structure. The geometry considered is shown on the left of Figure 4.7. This test case has been studied with the other optimal control approaches presented in Chapters 3 and 5 as well. We recall that we used the same boundary conditions, physical

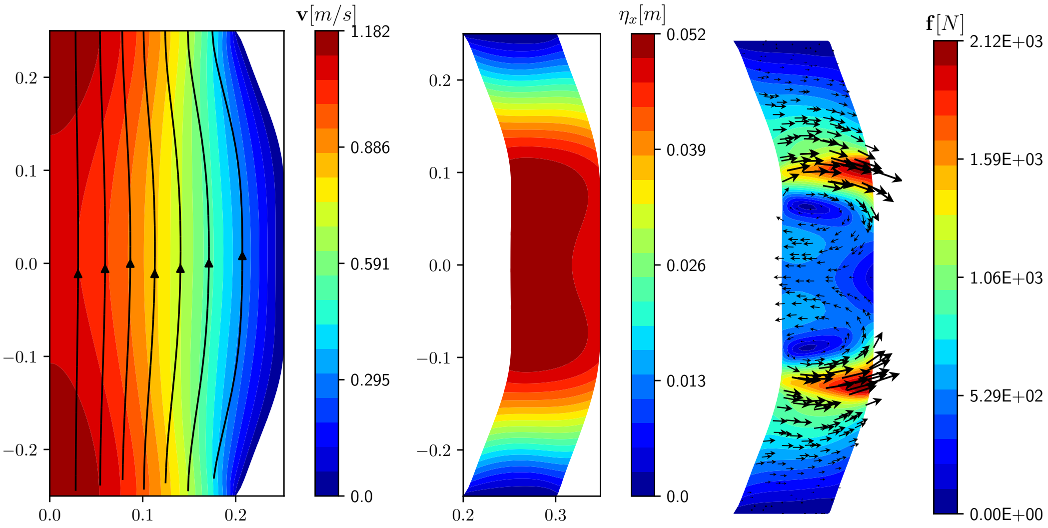

Figure 4.8: Controlled case with velocity profiles $\boldsymbol{v}$ and streamlines in the liquid and displacement $\boldsymbol{\eta}$ in the solid (on the left). Force vectors $\mathbf{f}$ in black and magnitude in colors (on the right).

Table 4.2: Objective functionals $\mathcal{J}$ and average x-displacement over the controlled region Ω_d computed with no control ($\beta = \infty$) and different β values.

β	∞	10^{-11}	10^{-12}	10^{-13}
$\mathcal{J}(\boldsymbol{\eta}, \mathbf{f}) \cdot 10^8$	1292.4	25.854	5.8864	2.3875
$\bar{\eta}_x\ [m]$	0.0180	0.0494	0.0498	0.0499

properties and objective functional, while changing the control parameter in order to compare the different controls in terms of functional reduction.

Now a fluid flows vertically from the bottom to the top in a plane channel. The fluid region Ω_f is on the left, the solid domain Ω_s, in gray, is on the right and the dotted region is the controlled domain $\Omega_d \subset \Omega_s$ The left boundary AF is a symmetry axis and on the bottom boundary AB pressure conditions with $p_{AB} = 11500Pa$ and vanishing tangential velocity are set. All the boundaries are fixed except the right segment CD, which is free to move with fixed endpoints C and D. The physical properties are the following

$$\rho_s = \rho_f = 10^3 kg/m^3, \quad \nu_f = 0.07 m^2/s, \quad \nu_s = 0.2, \quad E = 10^6 Pa\,, \qquad (4.40)$$

so the solid can easily deform. The optimal control algorithm aims to find the optimal force on the whole solid domain Ω_s such that the x-component of the displacement over the region Ω_d matches the uniform target value $\eta_d = 0.05m$.

The displacement in the remaining part solid domain is not controlled and thus can have any value, solution of the state system. Therefore, in the objective functional (4.16) we set $b = 1$, $a = 0$, $\eta_d = 0.05m$ obtaining

$$\mathcal{J}(\boldsymbol{\eta}, \mathbf{f}) = \frac{1}{2} \int_{\Omega_d} \omega(\eta_x - 0.05)^2 d\Omega + \frac{1}{2}\beta \int_{\Omega_c} ||\mathbf{f}||^2 d\Omega \,. \tag{4.41}$$

In Figure 4.7 we report the fluid velocity profile and the solid displacement in the reference configuration. The results obtained in the controlled case with $\beta = 10^{-13}$ are reported in Figure 4.8 and the functionals $\mathcal{J}(\boldsymbol{\eta}, \mathbf{f})$, together with the mean horizontal displacement, in Table 4.2. Finally, we report on the right of Figure 4.8 the profile of the force acting on the solid. The force has the highest intensity near the boundaries of the controlled domain Ω_d and pushes mainly to the right. Inside of Ω_d the force pushes, with lower intensity, to the left in order to balance the stress induced on the controlled region by the fluid, obtaining a flat profile with uniform displacement.

We now compare these results with those obtained applying the pressure boundary control and presented in Chapter 3. We first notice that with the distributed control the fluid velocity in the optimized configuration is much smaller. In fact, with the boundary control we have a large pressure gradient between the fluid inlet and outlet and as a consequence the velocity increases. Now, on the contrary, the boundary pressure values are fixed and are the same as in the reference configuration with no control. Furthermore, the solid deformation is now more uniform with an average value closer to the target one. The functional values reported in Table 4.2 are lower than those obtained with the boundary control, meaning that the distributed control has reached an optimized solution closer to the desired one. One can see that the greatest improvements are always obtained with the lowest β value.

CHAPTER 5

An inverse Young modulus estimation for fluid structure interaction systems

In this Chapter we study an optimal control problem based on adjoint variables and Lagrangian formalism for the Young modulus estimation of a fluid-structure interaction problem. A large part of the papers that can be found in literature refers to FSI direct problems, where the physical properties of the materials are known *a priori* and the solution of the corresponding equations gives the solid deformed shape and the fluid velocity-pressure fields. However, it is also interesting to study the inverse problem, where the goal is to find the optimal value of some physical properties, such that the FSI problem solution is close to a desired one. The latter is also called a *parameter estimation* problem. The objective of our optimal control problem is to obtain a desired solid shape by controlling the solid material properties. This problem has many industrially relevant applications where changes in the mechanical properties as a function of temperature are important. As a consequence of temperature changes, if the Young modulus is known then the solid temperature distribution, which corresponds to the desired shape, can be found in a straightforward manner. We take into account constraints over the control to avoid negative or very high values of the Young modulus and obtain a variational inequality in the optimality system that can be solved using the Lagrangian multiplier method. In literature a few papers dealing with FSI optimal control and parameter estimation can be found [48, 47]. In [48] a steady Lamé parameter estimation problem is studied, while in [47] the authors solve an unsteady interface displacement field minimization problem for cardiovascular applications. In the rest of this Chapter we first introduce the mathematical model used for the direct FSI problem. Then, we derive the optimality system from the first order necessary conditions and present a projected gradient-based method for the numerical solution. Finally, we report some numerical tests with different control constraints in order to validate the proposed approach.

5.1 Mathematical model

In this section we introduce the mathematical model that describes our FSI problem. We consider the following steady strong form of the FSI system

$$\nabla \cdot \boldsymbol{v} = 0 \qquad \text{on } \Omega_f \,, \tag{5.1}$$

$$\rho_f (\boldsymbol{v} \cdot \nabla)\boldsymbol{v} - \nabla \cdot \boldsymbol{\sigma}_f = \mathbf{0} \qquad \text{on } \Omega_f \,, \tag{5.2}$$

$$\nabla \cdot \boldsymbol{\sigma}_s(\boldsymbol{\eta}) = \mathbf{0} \qquad \text{on } \Omega_s \,, \tag{5.3}$$

where the fluid velocity and density are denoted with $\boldsymbol{v}$ and ρ_f, respectively. The solid Cauchy stress tensor $\boldsymbol{\sigma}_s$ of a Saint Venant-Kirchhoff material can be written as

$$\boldsymbol{\sigma}_s(\boldsymbol{\eta}) = E\mathbf{S}(\boldsymbol{\eta}) = \lambda_s (\nabla \cdot \boldsymbol{\eta})\mathbf{I} + \mu_s (\nabla \boldsymbol{\eta} + \nabla \boldsymbol{\eta}^T) \,, \tag{5.4}$$

where $\boldsymbol{\eta}$ is the unknown displacement field and E is the solid Young modulus. By substituting the following definitions of the Lamé parameters μ_s and λ_s

$$\mu_s = \frac{E}{2(1+\nu)} \qquad \lambda_s = \frac{E\nu}{(1+\nu)(1-2\nu)} \,, \tag{5.5}$$

into the (5.4) we obtain

$$\mathbf{S}(\boldsymbol{\eta}) = \frac{1}{2(1+\nu)} (\nabla \boldsymbol{\eta} + \nabla \boldsymbol{\eta}^T) + \frac{\nu}{(1+\nu)(1-2\nu)} (\nabla \cdot \boldsymbol{\eta})\mathbf{I} \,. \tag{5.6}$$

The Young modulus E and Poisson ratio ν determine the solid physical properties. The stress tensor $\boldsymbol{\sigma}_f$ for a Newtonian fluid with pressure p reads

$$\boldsymbol{\sigma}_f = \boldsymbol{\sigma}_f(p, \boldsymbol{v}) = -p\mathbf{I} + (\nabla \boldsymbol{v} + \nabla \boldsymbol{v}^T) \,. \tag{5.7}$$

The FSI strong formulation is completed with the appropriate boundary and interface conditions

$$\begin{array}{rlrl} \boldsymbol{v} = \boldsymbol{v}_0 & \text{on } \Gamma_d^f, & \boldsymbol{\eta} = \boldsymbol{\eta}_0 & \text{on } \Gamma_d^s\,, \\ \boldsymbol{\sigma}_f \cdot \mathbf{n}_f = \mathbf{0} & \text{on } \Gamma_n^f, & \boldsymbol{\sigma}_s \cdot \mathbf{n}_s = \mathbf{0} & \text{on } \Gamma_n^s\,, \\ \boldsymbol{\sigma}_f \cdot \mathbf{n}_f + \boldsymbol{\sigma}_s \cdot \mathbf{n}_s = \mathbf{0} & \text{on } \Gamma_i, & \boldsymbol{v} = \mathbf{0} & \text{on } \Gamma_i\,, \end{array} \tag{5.8}$$

where we impose Dirichlet boundary conditions for the fluid velocity and solid displacement on Γ_d^f and Γ_d^s, respectively. Neumann homogeneous boundary conditions are imposed on the surfaces Γ_n^f and Γ_n^s. On the interface Γ_i we impose vanishing fluid velocity and the normal components of the stress tensors $\boldsymbol{\sigma}$ have to be continuous. We denote with $\mathbf{n}_s$ and $\mathbf{n}_f$ the normal unit vectors to the solid and fluid boundaries with $\mathbf{n}_s = -\mathbf{n}_f$ on Γ_i. Since we are solving the FSI in a monolithic fashion the interface coupling conditions in (5.8) are automatically satisfied. We now introduce the following functional spaces to keep the notation clear

$$\begin{aligned} \boldsymbol{V} &= \{\boldsymbol{\phi} \in \boldsymbol{H}^1(\Omega) : \boldsymbol{\phi}_{\Gamma_d^f \cup \Gamma_d^s} = \mathbf{0}\}\,, \quad Q^{s,f} = L^2(\Omega^{s,f})\,, \\ \boldsymbol{W}^{s,f} &= \{\boldsymbol{\phi} \in \boldsymbol{H}^1(\Omega) : \boldsymbol{\phi}_{\Gamma^{s,f}} = \mathbf{0}\}\,. \end{aligned}$$

In order to recover the variational formulation of the state system we follow the standard approach obtaining

$$\int_{\Omega_f} (\nabla \cdot \boldsymbol{v})\, \psi \, d\Omega \; = 0 \qquad \forall \psi \in Q^f\,, \tag{5.9}$$

$$\begin{aligned} &\int_{\Omega_f} \left[(\rho_f (\boldsymbol{v} \cdot \nabla)\boldsymbol{v}) \cdot \boldsymbol{\phi} - p \nabla \cdot \boldsymbol{\phi} + \mu_f \nabla \boldsymbol{v} : \nabla \boldsymbol{\phi}\right] \, d\Omega \, + \\ &\quad \int_{\Omega_s} E \left[\frac{\nu}{(1+\nu)(1-2\nu)} (\nabla \cdot \boldsymbol{\eta})(\nabla \cdot \boldsymbol{\phi}) + \frac{1}{2(1+\nu)} \nabla \boldsymbol{\eta} : \nabla \boldsymbol{\phi}\right] \, d\Omega \, + \\ &\quad \int_{\Gamma} E \left[\frac{1}{2(1+\nu)} (\boldsymbol{\nabla} \boldsymbol{\eta} \cdot \mathbf{n}_s) \cdot \boldsymbol{\phi} + \frac{\nu}{(1+\nu)(1-2\nu)} (\boldsymbol{\nabla} \cdot \boldsymbol{\eta}) \mathbf{n}_s \cdot \boldsymbol{\phi}\right] \, d\Gamma \, + \\ &\quad \int_{\Gamma} [[p \mathbf{n}_f - \mu_f (\boldsymbol{\nabla} \boldsymbol{v} \cdot \mathbf{n}_f) \cdot \boldsymbol{\phi}] \, d\Gamma = 0 \qquad \forall \boldsymbol{\phi} \in \boldsymbol{V}\,, \end{aligned} \tag{5.10}$$

where the surface integrals vanish due to the boundary and interface conditions (5.8).

In order to obtain a symmetric formulation of the monolithic optimality system we introduce in (5.9-5.10) a mesh displacement field $\widehat{\boldsymbol{\eta}}$, solution of the following boundary value problem

$$\nabla^2 \widehat{\boldsymbol{\eta}} = \mathbf{0} \qquad \mathbf{x} \in \Omega_s \,, \tag{5.11}$$

$$\widehat{\boldsymbol{\eta}} = \boldsymbol{\eta} \quad \text{on } \Gamma_i \,, \tag{5.12}$$

$$\widehat{\boldsymbol{\eta}} = \mathbf{0} \quad \text{on } (\partial\Omega_s - \Gamma_i) \,. \tag{5.13}$$

For the same reasons we also extend the velocity field to the solid domain

$$\boldsymbol{v} = \begin{cases} \tau\,(\boldsymbol{\eta} - \widehat{\boldsymbol{\eta}}) & \text{on } \Omega_s(\boldsymbol{\eta}) \\ \boldsymbol{v} & \text{solution of (5.1-5.2) on } \Omega_f(\boldsymbol{\eta}) \end{cases} , \tag{5.14}$$

where τ is an arbitrary positive constant. We remark that, in a stationary problem, the solid physical velocity is zero, while this fictitious velocity can be seen as the driving element of the solid motion during the nonlinear optimization process. With this extension we can easily compute the shape derivatives of a functional on a moving domain. The FSI system can therefore be rewritten as

$$\int_{\Omega_f(\widehat{\boldsymbol{\eta}})} (\nabla \cdot \boldsymbol{v})\, \psi \, d\Omega \; = 0 \qquad \forall \psi \in Q^f \,, \tag{5.15}$$

$$\int_{\Omega_s(\widehat{\boldsymbol{\eta}})} E \left[\frac{1}{2(1+\nu)} \nabla \boldsymbol{\eta} : \nabla \boldsymbol{\phi} + \frac{\nu}{(1+\nu)(1-2\nu)} (\nabla \cdot \boldsymbol{\eta})(\nabla \cdot \boldsymbol{\phi}) \right] d\Omega +$$
$$\int_{\Omega_f(\widehat{\boldsymbol{\eta}})} \left[(\rho_f (\boldsymbol{v} \cdot \nabla) \boldsymbol{v}) \cdot \boldsymbol{\phi} - p \nabla \cdot \boldsymbol{\phi} + \mu_f \nabla \boldsymbol{v} : \nabla \boldsymbol{\phi} \right] d\Omega = 0 \quad \forall \boldsymbol{\phi} \in \boldsymbol{V} \,, \tag{5.16}$$

$$\int_{\Omega_s(\widehat{\boldsymbol{\eta}})} \nabla \widehat{\boldsymbol{\eta}} : \nabla \widehat{\boldsymbol{\eta}}_a \, d\Omega = 0 \qquad \forall\, \widehat{\boldsymbol{\eta}}_a \in \boldsymbol{W}^s \,, \tag{5.17}$$

$$\int_{\Omega_s(\widehat{\boldsymbol{\eta}})} (\boldsymbol{v} - \tau(\boldsymbol{\eta} - \widehat{\boldsymbol{\eta}})) \cdot \boldsymbol{\beta}_a \, d\Omega = 0 \qquad \forall \boldsymbol{\beta}_a \in Q^s \,. \tag{5.18}$$

5.1.1 Optimality system

In this parameter estimation problem we want to minimize the following quadratic functional based on the difference between the solid displacement $\boldsymbol{\eta}$ and the target one $\boldsymbol{\eta}_d$

$$\mathcal{J}(\boldsymbol{\eta}(E)) = \frac{1}{2} \int_{\Omega_s} \omega ||\boldsymbol{\eta} - \boldsymbol{\eta}_d||^2 \, d\Omega + \frac{1}{2} \beta \int_{\Omega_s} |E|^2 \, d\Omega \,, \tag{5.19}$$

where ω is a weight function used to determine where, in the solid domain, the displacement mismatch has to be minimized. The Tichonov regularization term is introduced to keep the control E in the space of square integrable functions $L^2(\Omega^s)$. If one is interested in having a more regular control then another term can be added to the cost functional obtaining

$$\mathcal{J}(\boldsymbol{\eta}(E)) = \frac{1}{2}\int_{\Omega_s} \omega(\boldsymbol{\eta}-\boldsymbol{\eta}_d)^2\, d\Omega + \frac{1}{2}\beta\int_{\Omega_s} |E|^2\, d\Omega + \frac{1}{2}\alpha\int_{\Omega_s} |\nabla E|^2\, d\Omega\,, \quad (5.20)$$

thus constraining the Young modulus to $E \in H^1(\Omega^s)$. Since in practical applications technical limits can occur, we take into account constraints over the Young modulus in order to avoid negative or very large values, see [39, 40]. For this purpose we define the space of admissible controls $\mathcal{E}_{ad}$ as

$$\mathcal{E}_{ad} = \{E \in L^2(\Omega^s) : \chi \leqslant E \leqslant \omega \text{ with } \chi, \omega \in \mathbb{R}^+\}\,, \quad (5.21)$$

where χ and ω are the lower and upper limits for the control, respectively. The set of all the admissible solutions $\mathcal{A}_{ad}$ is defined as follows

Definition. *$(\boldsymbol{\eta}, E)$ is said to be an admissible solution if $\boldsymbol{\eta} \in H^1(\Omega^s)$, the functional $\mathcal{J}(\boldsymbol{\eta}(E))$ is bounded, and there exists a $E \in \mathcal{E}_{ad}$ such that $(\boldsymbol{\eta}, E)$ satisfies the problem in (5.9-5.10).*

With this notation, the optimal control problem can then be formulated as

Problem. *Given $\boldsymbol{\eta}_d$, find $(\boldsymbol{\eta}, E) \in \mathcal{A}_{ad}$ such that $\mathcal{J}(\boldsymbol{\eta}(E)) \leqslant \mathcal{J}(\mathbf{w}(h))$ $\forall(\mathbf{w}, h) \in \mathcal{A}_{ad}$.*

If $(\bar{\boldsymbol{\eta}}, \bar{E})$ is an optimal solution of the control problem and the Gateaux derivative of $\mathcal{J}(\bar{\boldsymbol{\eta}}(\bar{E}))$ exists, then the following variational inequality holds true

$$\mathcal{J}'(\bar{\boldsymbol{\eta}}(\bar{E})) \cdot (h - \bar{E}) \geqslant 0 \quad \forall h \in \mathcal{E}_{ad}\,. \quad (5.22)$$

In fact from the definition of optimal solution $(\bar{\boldsymbol{\eta}}, \bar{E})$, we have

$$\mathcal{J}(\bar{\boldsymbol{\eta}}(\bar{E})) - \mathcal{J}(\tilde{\boldsymbol{\eta}}(\tilde{E})) \geqslant 0 \quad \forall \tilde{E} \in \mathcal{E}_{ad}\,. \quad (5.23)$$

As $\mathcal{E}_{ad}$ is convex, then we can set $\tilde{E} = ht + (1-t)\bar{E}$ for all $t \in [0,1]$ and for all $h \in \mathcal{E}_{ad}$. Hence

$$\mathcal{J}(\bar{\boldsymbol{\eta}}(\bar{E} - t(\bar{E} - h))) - \mathcal{J}(\bar{\boldsymbol{\eta}}(\bar{E})) \geqslant 0 \quad \forall t \in [0,1]\,, \quad (5.24)$$

which, by using the definition of the Gateaux derivative, implies (5.22) when t tends to 0.

We now present a strategy that can be adopted in order to deal with this variational inequality. We introduce an auxiliary variable s to transform the inequality constraint into an equality, which can then be treated with standard techniques for equality constrained minimization problems. We replace

$$\chi \leqslant E \leqslant \omega \qquad \text{on } \Omega^s\,, \tag{5.25}$$

by

$$(E - E_0)^2 - E_m^2 + s^2 = 0 \qquad \text{on } \Omega^s\,, \tag{5.26}$$

with $s \in L^2(\Omega^s)$ and $E_0 = (\chi + \omega)/2$, $E_m = (\omega - \chi)/2$. It can be easily verified that if (5.25) is satisfied, then so is (5.26). Furthermore, if $(\bar{\boldsymbol{\eta}}, \bar{E})$ is an optimal solution, then it can be shown that a subspace of the solution space exists, $\mathcal{A}'_{ad} \subset \mathcal{A}_{ad}$, such that

1. on $\mathcal{A}'_{ad}$ we have $\chi < E < \omega$ and

   $$\mathcal{J}'(\bar{\boldsymbol{\eta}}(\bar{E})) \cdot \tilde{E} = 0 \qquad \forall \tilde{E} \in L^2(\Omega^s)\,, \tag{5.27}$$

   with $s^2 = E_m^2 - (E - E_0)^2$;

2. on $\mathcal{A}_{ad} - \mathcal{A}'_{ad}$ we have $s = 0$ which implies $E = \chi$ or $E = \omega$.

In case 1 the constraints are said to be *inactive* since they do not limit the control. As a consequence, the optimal solution obtained corresponds to a local minimum of the objective functional. In case 2 one of the constraints is *active* and limits the control, therefore the optimal solution may not be a functional minimum. No more improvements can be made since the control coincides with one of the bounds, however we have found the optimal solution in the admissible set $\mathcal{E}_{ad}$. If we use this equation in a numerical algorithm the variable s introduces many local minima, leading to a poor computational behavior, therefore it will not be used in our algorithm. In this work we deal instead with the constraints on the control by using a projected gradient method that will be presented in the next section.

In order to recover the optimality system we use the Lagrangian multiplier method, which is used to find stationary points, such as local minima, of constrained problems. Here the constraints are represented by the state equations of the FSI problem. The following augmented Lagrangian functional $\mathcal{L}$ is the sum of the cost functional (5.19) and of the state equations multiplied by the appropriate Lagrangian multiplier, which are the so-called adjoint variables $(\boldsymbol{v}_a, p_a, \boldsymbol{\eta}_a)$

$$
\begin{aligned}
\mathcal{L}(p, \boldsymbol{v}, E, \boldsymbol{\eta}, \widehat{\boldsymbol{\eta}}, p_a, \boldsymbol{v}_a, \widehat{\boldsymbol{\eta}}_a, \widehat{\mathbf{s}}_a, \beta_a) &= \mathcal{J}(\boldsymbol{\eta}(E)) + \int_{\Omega_f} (\nabla \cdot \boldsymbol{v})\, p_a \, d\Omega \qquad (5.28)\\
&+ \int_{\Omega_f} [\rho_f (\boldsymbol{v} \cdot \nabla)\boldsymbol{v} + \nabla p - \nabla \cdot (\mu_f \nabla \boldsymbol{v})] \cdot \boldsymbol{v}_a \, d\Omega + \int_{\Omega_s} \nabla^2 \widehat{\boldsymbol{\eta}} \cdot \widehat{\boldsymbol{\eta}}_a \, d\Omega \\
&+ \int_{\Omega_s} \left[-\nabla \cdot E \left(\frac{1}{2(1+\nu)} \nabla \boldsymbol{\eta} + \frac{\nu}{(1+\nu)(1-2\nu)} \mathbf{I} (\nabla \cdot \boldsymbol{\eta}) \right) \right] \cdot \boldsymbol{v}_a \, d\Omega \\
&+ \int_{\Gamma_i} \widehat{\mathbf{s}}_a \cdot \left[(\widehat{\boldsymbol{\eta}} - \boldsymbol{\eta}) + \frac{\boldsymbol{v}}{\tau} \right] d\Gamma + \int_{\Omega_s} \boldsymbol{\beta}_a \cdot [\boldsymbol{v} - \tau(\boldsymbol{\eta} - \widehat{\boldsymbol{\eta}})] \, d\Omega \, .
\end{aligned}
$$

In order to derive the optimality system we impose the following first order necessary condition

$$
\delta \mathcal{L} = 0 \, . \qquad (5.29)
$$

In the following we denote with δq the variation of a generic function q and with $(D\mathcal{L}/Dq)\delta q$ the Fréchet derivative of a functional $\mathcal{L}$ in the direction δq. Moreover, the shape derivatives of a functional F on a domain moving with velocity $\delta \boldsymbol{v}$ can be computed as

$$
\frac{dF}{d\Omega(\widehat{\boldsymbol{\eta}})} \delta \boldsymbol{v} = \int_{\partial\Omega(\widehat{\boldsymbol{\eta}})} y \delta \boldsymbol{v} \cdot \mathbf{n} \, d\Gamma \, , \qquad (5.30)
$$

$$
\frac{dF}{d\Gamma(\widehat{\boldsymbol{\eta}})} \delta \boldsymbol{v} = \int_{\Gamma(\widehat{\boldsymbol{\eta}})} (\nabla_n + \chi)\, y \delta \boldsymbol{v} \cdot \mathbf{n} \, d\Gamma \, , \qquad (5.31)
$$

where ∇_n is the normal derivative operator and χ the mean curvature of Γ. We remark that the above shape derivatives vanish when the integrated function vanishes on the boundary.

The stationary points of the Lagrangian functional can be found by setting to zero the Fréchet derivatives taken with respect to all the problem variables, since each variation is independent from the others. When the derivatives are taken with respect to the adjoint variables $(p_a, \boldsymbol{v}_a, \widehat{\boldsymbol{\eta}}_a, \boldsymbol{\beta}_a)$ the weak form of the state system (5.1-5.3) is recovered together with the boundary conditions. By taking the derivatives with respect to the state variables $(\boldsymbol{v}, p, \boldsymbol{\eta}, \widehat{\boldsymbol{\eta}})$, the weak form of the adjoint or dual system is obtained. We first collect all the terms involving the variations $\delta\boldsymbol{v}$

$$
\begin{aligned}
&\frac{D\mathcal{L}}{D\boldsymbol{v}}\delta\boldsymbol{v} = \int_{\Omega_f} (\nabla\cdot\delta\boldsymbol{v})\, p_a \, d\Omega \, + \int_{\Omega_s} \delta\boldsymbol{v}\cdot\boldsymbol{\beta}_a \, d\Omega + \frac{1}{\tau}\int_{\Gamma_i} \delta\boldsymbol{v}\cdot\widehat{\mathbf{s}}_a \, d\Gamma + \\
&\int_{\Omega_f} \Big[(\rho_f(\delta\boldsymbol{v}\cdot\nabla)\boldsymbol{v})\cdot\boldsymbol{v}_a + (\rho_f(\boldsymbol{v}\cdot\nabla)\delta\boldsymbol{v})\cdot\boldsymbol{v}_a - \nabla\cdot(\mu_f\nabla\delta\boldsymbol{v})\cdot\boldsymbol{v}_a \Big] \, d\Omega + \\
&\int_{\partial\Omega_f} (\nabla\cdot\boldsymbol{v})\, p_a \, \delta\boldsymbol{v}\cdot\mathbf{n} \, d\Gamma \, + \int_{\partial\Omega_d} \omega\frac{(\boldsymbol{\eta}-\boldsymbol{\eta}_d)^2}{2}\delta\boldsymbol{v}\cdot\mathbf{n} \, d\Omega \\
&\int_{\partial\Omega_f} \boldsymbol{v}_a\cdot\Big[\rho_f(\boldsymbol{v}\cdot\nabla)\boldsymbol{v} + \nabla p - \nabla\cdot(\mu_f\nabla\boldsymbol{v})\Big]\delta\boldsymbol{v}\cdot\mathbf{n} \, d\Gamma + \qquad (5.32)\\
&\int_{\partial\Omega_s} \boldsymbol{v}_a\cdot\left[-\nabla\cdot E\left(\frac{1}{2(1+\nu)}\nabla\boldsymbol{\eta} + \frac{\nu}{(1+\nu)(1-2\nu)}\mathbf{I}(\nabla\cdot\boldsymbol{\eta})\right)\right] \delta\boldsymbol{v}\cdot\mathbf{n} \; d\Gamma + \\
&\int_{\partial\Omega_s} \left(\nabla^2\widehat{\boldsymbol{\eta}}\cdot\widehat{\boldsymbol{\eta}}_a\right) \delta\boldsymbol{v}\cdot\mathbf{n} \, d\Gamma + \int_{\Gamma_i} (\nabla_n + \chi) \left[\widehat{\mathbf{s}}_a\cdot\left[(\widehat{\boldsymbol{\eta}}-\boldsymbol{\eta}) + \frac{\boldsymbol{v}}{\tau}\right]\right] \, \delta\boldsymbol{v}\cdot\mathbf{n} \, d\Gamma + \\
&\int_{\partial\Omega_s} \boldsymbol{\beta}_a\cdot[\boldsymbol{v} - \tau(\boldsymbol{\eta}-\widehat{\boldsymbol{\eta}})] \; \delta\boldsymbol{v}\cdot\mathbf{n} \, d\Gamma = 0 \qquad \forall\delta\boldsymbol{v}\in\boldsymbol{V}\,.
\end{aligned}
$$

The surface integrals over $\partial\Omega_s$ and $\partial\Omega_f$ vanish since the integrated functions are equal to zero, due to the state system (5.15-5.16). The term integrated on $\partial\Omega_d$ vanishes as well, since we can take an arbitrary weight function ω that vanishes on $\partial\Omega_d$. Finally, the term referring to the interface shape derivative can be simplified due to the (5.14). The resulting equation for $\delta\boldsymbol{v}$ is therefore the following

$$
\begin{aligned}
&\int_{\Omega_f} \Big[(\rho_f(\delta\boldsymbol{v}\cdot\nabla)\boldsymbol{v})\cdot\boldsymbol{v}_a + (\rho_f(\boldsymbol{v}\cdot\nabla)\delta\boldsymbol{v})\cdot\boldsymbol{v}_a - \nabla\cdot(\mu_f\nabla\delta\boldsymbol{v})\cdot\boldsymbol{v}_a \Big] d\Omega + \\
&\quad \int_{\Omega_f} (\nabla\cdot\delta\boldsymbol{v}) p_a \, d\Omega + \int_{\Omega_s} \delta\boldsymbol{v}\cdot\boldsymbol{\beta}_a \, d\Omega + \frac{1}{\tau}\int_{\Gamma_i} \delta\boldsymbol{v}\cdot\widehat{\mathbf{s}}_a \, d\Gamma = 0 \quad \forall\delta\boldsymbol{v}\in\boldsymbol{V}\,.
\end{aligned} \qquad (5.33)
$$

Collecting now the terms with $\delta\boldsymbol{\eta}$ we get

$$
\begin{aligned}
&\frac{D\mathcal{L}}{D\boldsymbol{\eta}}\delta\boldsymbol{\eta} = \int_{\Omega_d} \omega(\boldsymbol{\eta}-\boldsymbol{\eta}_d)\delta\boldsymbol{\eta} \, d\Omega + \int_{\Omega_s} [\mu_s\nabla\delta\boldsymbol{\eta} : \nabla\boldsymbol{v}_a + \lambda_s(\nabla\cdot\delta\boldsymbol{\eta})(\nabla\cdot\boldsymbol{v}_a)] \; d\Omega \\
&-\tau\int_{\Omega_s} \delta\boldsymbol{\eta}\cdot\boldsymbol{\beta}_a \, d\Omega - \int_{\Gamma_i} \widehat{\mathbf{s}}_a\cdot\delta\boldsymbol{\eta} \, d\Gamma = 0 \qquad \forall\delta\boldsymbol{\eta}\in\mathbf{H}^1_{\Gamma^s_d}(\Omega_s)\,. \qquad (5.34)
\end{aligned}
$$

The following expressions of $\boldsymbol{\beta}_a$ and $\widehat{\mathbf{s}}_a$ can be obtained by integrating by parts the terms where the variation $\delta\boldsymbol{\eta}$ is differentiated

$$\boldsymbol{\beta}_a = -\frac{1}{\tau}\nabla\cdot[\mu_s\nabla\boldsymbol{v}_a + \lambda_s\mathbf{I}(\nabla\cdot\boldsymbol{v}_a)] + \frac{\omega}{\tau}(\boldsymbol{\eta}-\boldsymbol{\eta}_d)\,, \tag{5.35}$$

$$\widehat{\mathbf{s}}_a = [\mu_s\nabla\boldsymbol{v}_a + \lambda_s\mathbf{I}(\nabla\cdot\boldsymbol{v}_a)]\cdot\mathbf{n}\,. \tag{5.36}$$

By substituting (5.35-5.36) into the (5.33) we obtain

$$\begin{aligned}&\int_{\Omega_f}(\nabla\cdot\delta\boldsymbol{v})\,p_a\,d\Omega + \frac{1}{\tau}\int_{\Omega_s}[\mu_s\nabla\boldsymbol{v}_a : \nabla\delta\boldsymbol{v} + \lambda_s(\nabla\cdot\boldsymbol{v}_a)(\nabla\cdot\delta\boldsymbol{v})]\,d\Omega +\\ &\int_{\Omega_f}\Big[(\rho_f(\delta\boldsymbol{v}\cdot\nabla)\boldsymbol{v})\cdot\boldsymbol{v}_a + (\rho_f(\boldsymbol{v}\cdot\nabla)\delta\boldsymbol{v})\cdot\boldsymbol{v}_a - \nabla\cdot(\mu_f\nabla\delta\boldsymbol{v})\cdot\boldsymbol{v}_a\Big]\,d\Omega +\\ &\frac{1}{\tau}\int_{\Omega_d}\omega(\boldsymbol{\eta}-\boldsymbol{\eta}_d)\delta\boldsymbol{v}\,d\Omega = 0 \qquad \forall\delta\boldsymbol{v}\in\boldsymbol{V}\,.\end{aligned} \tag{5.37}$$

Collecting $\delta\widehat{\boldsymbol{\eta}}$ terms we obtain

$$\int_{\Omega_s}\nabla\delta\widehat{\boldsymbol{\eta}} : \nabla\widehat{\boldsymbol{\eta}}_a\,d\Omega + \tau\int_{\Omega_s}\delta\widehat{\boldsymbol{\eta}}\cdot\boldsymbol{\beta}_a\,d\Omega + \int_{\Gamma_i}\widehat{\mathbf{s}}_a\cdot\delta\widehat{\boldsymbol{\eta}}\,d\Gamma = 0 \quad \forall\delta\widehat{\boldsymbol{\eta}}\in\mathbf{H}^1_{\Gamma^s_d}(\Omega_s)\,, \tag{5.38}$$

that, by using (5.35-5.36), can be rewritten as

$$\begin{aligned}\int_{\Omega_s}\nabla\widehat{\boldsymbol{\eta}}_a : \nabla\delta\widehat{\boldsymbol{\eta}}\,d\Omega = -\int_{\Omega_s}[\mu_s\nabla\boldsymbol{v}_a : \nabla\delta\widehat{\boldsymbol{\eta}} + \lambda_s(\nabla\cdot\boldsymbol{v}_a)(\nabla\cdot\delta\widehat{\boldsymbol{\eta}})]\,d\Omega +\\ \int_{\Omega_d}\omega(\boldsymbol{\eta}-\boldsymbol{\eta}_d)\delta\widehat{\boldsymbol{\eta}}\,d\Omega \qquad \forall\delta\widehat{\boldsymbol{\eta}}\in\mathbf{H}^1_{\Gamma^s}(\Omega_s)\,.\end{aligned} \tag{5.39}$$

By setting to zero the Fréchet derivatives taken along the direction δp we obtain

$$\frac{D\mathcal{L}}{Dp}\delta p = \int_{\Omega_f}(\nabla\cdot\boldsymbol{v}_a)\delta p\;d\Omega = 0 \qquad \forall\delta p\in L^2(\Omega)\,. \tag{5.40}$$

Finally, when taking the derivatives with respect to the control parameter E we recover the variational equality

$$\begin{aligned}\frac{D\mathcal{L}}{DE}\delta E = \int_{\Omega_s}(\mathbf{S}(\boldsymbol{\eta}) : \nabla\boldsymbol{v}_a)\delta E\,d\Omega + \int_{\Omega_s}\beta E\delta E + \alpha\nabla E\cdot\nabla\delta E\,d\Omega = 0\\ \forall\delta E\in H^1(\Omega_s)\,,\end{aligned} \tag{5.41}$$

that in the case $\alpha = 0$ reduces to the following expression

$$E = \frac{\mathbf{S}(\boldsymbol{\eta}) : \nabla\boldsymbol{v}_a}{\beta}\,. \tag{5.42}$$

To summarize, the adjoint system in weak form can be written as

$$
\begin{aligned}
&\int_{\Omega_f} (\nabla \cdot \boldsymbol{v}_a)\delta p \, d\Omega = 0 && \forall \delta p \in L^2(\Omega)\,, \qquad (5.43)\\
&\int_{\Omega_f} (\nabla \cdot \delta \boldsymbol{v})\, p_a \, d\Omega + \frac{1}{\tau}\int_{\Omega_s} \left[\mu_s \nabla \boldsymbol{v}_a : \nabla \delta \boldsymbol{v} + \lambda_s (\nabla \cdot \boldsymbol{v}_a)(\nabla \cdot \delta \boldsymbol{v})\right] d\Omega + \\
&\quad \int_{\Omega_f} \Big[(\rho_f (\delta \boldsymbol{v} \cdot \nabla)\boldsymbol{v}) \cdot \boldsymbol{v}_a + (\rho_f (\boldsymbol{v} \cdot \nabla)\delta \boldsymbol{v}) \cdot \boldsymbol{v}_a - \nabla \cdot (\mu_f \nabla \delta \boldsymbol{v}) \cdot \boldsymbol{v}_a \Big] d\Omega + \\
&\quad \frac{1}{\tau}\int_{\Omega_d} \omega(\boldsymbol{\eta} - \boldsymbol{\eta}_d)\delta \boldsymbol{v} \, d\Omega = 0 && \forall \delta \boldsymbol{v} \in \boldsymbol{V}\,, \qquad (5.44)\\
&\int_{\Omega_s} \nabla \widehat{\boldsymbol{\eta}}_a : \nabla \delta \widehat{\boldsymbol{\eta}} \, d\Omega = -\int_{\Omega_s} \left[\mu_s \nabla \boldsymbol{v}_a : \nabla \delta \widehat{\boldsymbol{\eta}} + \lambda_s (\nabla \cdot \boldsymbol{v}_a)(\nabla \cdot \delta \widehat{\boldsymbol{\eta}})\right] d\Omega + \\
&\quad \int_{\Omega_d} \omega(\boldsymbol{\eta} - \boldsymbol{\eta}_d)\delta \widehat{\boldsymbol{\eta}} \, d\Omega && \forall \delta \widehat{\boldsymbol{\eta}} \in \mathbf{H}^1_{\Gamma^s}(\Omega_s)\,. \qquad (5.45)
\end{aligned}
$$

We remark that the equation for the adjoint displacement $\boldsymbol{\eta}_a$ has been neglected since it is not necessary to determine the control E.

The strong form of the *adjoint system* can be recovered by integrating by parts the terms where the variations δ are differentiated. After performing the integration by parts, we recover the adjoint state $(\boldsymbol{v}_a^f, \boldsymbol{v}_a^s, p_a) \in \mathbf{H}^1_{\partial\Omega_f - \Gamma_i}(\Omega_f) \cap \mathbf{H}^2(\Omega_f) \times \mathbf{H}^1_{\partial\Omega_s - \Gamma_i}(\Omega_s) \cap \mathbf{H}^2(\Omega_s) \times L^2_0(\Omega_f) \cap \mathbf{H}^1(\Omega_f)$, by solving

$$
\begin{aligned}
&\nabla \cdot \boldsymbol{v}_a^f = 0\,, && (5.46)\\
&-\rho_f (\nabla \boldsymbol{v})^T \boldsymbol{v}_a^f + \rho_f [(\boldsymbol{v} \cdot \nabla)\boldsymbol{v}_a^f] + \nabla p_a - \nabla \cdot (\mu_f \nabla \boldsymbol{v}_a^f) = \frac{\omega}{\tau}(\boldsymbol{\eta} - \boldsymbol{\eta}_d)\,, && (5.47)\\
&\nabla \cdot \boldsymbol{\sigma}_s(\boldsymbol{v}_a^s) = 0\,. && (5.48)
\end{aligned}
$$

with boundary conditions defined as

$$
\begin{aligned}
&\boldsymbol{v}_a^s = \boldsymbol{v}_a^f && \text{on } \Gamma_i\,,\\
&\boldsymbol{\sigma}_s(\boldsymbol{v}_a^s) \cdot \mathbf{n} = \boldsymbol{\sigma}_f(\boldsymbol{v}_a^f) \cdot \mathbf{n} && \text{on } \Gamma_i\,,\\
&\mu_f (\nabla \boldsymbol{v}_a) \cdot \mathbf{n} = -(\boldsymbol{v} \cdot \mathbf{n})\, \boldsymbol{v}_a\,, \ \ p_a = 0 && \text{on } \Gamma_n^f\,,\\
&\boldsymbol{v}_a = 0 && \text{on } \Gamma_{fd} \cup \Gamma_{sd}\,.
\end{aligned}
\tag{5.49}
$$

We remark that since we use a monolithic approach with a finite element approximation for both the state (5.15-5.16) and the adjoint system (5.43-5.44) the equilibrium conditions on the interface are automatically satisfied.

Algorithm 5 Description of the Projected Gradient Descent algorithm.

```
1. Set a state $(\boldsymbol{v}^0, p^0, \boldsymbol{\eta}^0)$ satisfying (5.15-5.16)    ▷ State setup - Reference case
2. Compute the functional $\mathcal{J}^0$ in (5.20)
3. Set $r^0 = 1$
for $i = 1 \to i_{max}$ do
    4. Solve the system (5.43-5.44) to obtain the adjoint state $(\boldsymbol{v}_a^i, p_a^i)$
    5. Compute the control update $\delta E^i$ by solving (5.41)
    6. Set $r^i = r^0$
    7. Set $E^i = P_L\left(E^{i-1} + \delta E^i\right)$
    while $\mathcal{J}^i(E^i) > \mathcal{J}^{i-1}(E^{i-1})$ do    ▷ Line search
        7. Set $r^i = \rho\, r^i$
        8. Solve (5.15-5.16) for the state $(\boldsymbol{v}^i, p^i, \boldsymbol{\eta}^i)$ with $E^i = P_L\left(E^{i-1} + r^i \delta E^i\right)$
        if $r^i < toll$ then
            Line search not successful    ▷ End of the algorithm
        end if
    end while
end for
```

5.2 Numerical implementation and tests

In this section we first describe our approach to solve the optimality system, then the finite element discretization used is presented and finally some numerical tests are reported. Due to its complexity the optimality system can not be solved in practice with a coupled *one-shot* approach. A *segregated* gradient based method is, instead, more suitable since the state and adjoint systems and the optimality condition are solved sequentially until a given criteria is satisfied, see [44].

In order to satisfy the inequality constraints we *project back* to the set of admissible controls $\mathcal{E}_{ad}$, see for more details [30]. To clarify let us suppose that the inequality constraint on the control E is satisfied by the current iterate E_{old}. Next, assume that the new iterate for the control given by

$$E_{new} = E_{old} + \delta E \,, \tag{5.50}$$

where δE is a step size, does not satisfy the constraint. By projecting back to $\mathcal{E}_{ad}$ we find a new E that satisfies the constraint and that is nearest E_{new} and use that point instead as the new iterate.

In Algorithm 5 the outline of the projected gradient method is reported. In the setup phase the state system is solved obtaining the reference state

$(\boldsymbol{v}^0, p^0, \boldsymbol{\eta}^0)$ and the reference functional $\mathcal{J}^0$. After the setup, by solving the adjoint system (5.43-5.44) we recover the adjoint velocity $\boldsymbol{v}_a$ that is exploited in (5.41) in order to obtain the gradient direction δE. Then a line search with backtracking strategy and contraction factor $\rho = 0.7$ is performed until a decrease of the objective functional is attained. The operator P_L used in the line search is the projection operator that projects back the control E to the set of admissible controls $\mathcal{E}_{ad}$. This algorithm ends either when two consecutively computed functionals are almost equal and no further improvements can be achieved or when the step length r becomes lower than a tolerance value $toll = 10^{-7}$. We implemented this algorithm in the in-house finite element code FEMuS, implemented with openMPI libraries, that uses a multigrid solver with mesh-moving capability and PETSc libraries for the linear systems. This code and its different solvers are available at [1].

We now introduce the finite element discretization used. Let Ω_h be an open bounded domain, $X^h \subset H^1(\Omega_h)$ and $S^h \subset L^2(\Omega_h)$ be two families of finite dimensional sub-spaces parameterized by h that tends to zero. We denote with S_0^h the family of finite dimensional sub-spaces containing piece-wise constant functions. In order to satisfy the *BBL inf-sup* condition (see [27]) we consider the velocity field $\mathbf{u}_h \in \mathbf{X}^h$ and the pressure $p_h \in S^h$ and use standard Taylor-Hood elements. We consider quadratic displacements fields $(\boldsymbol{\eta}, \widehat{\boldsymbol{\eta}}) \in X_2^h$. The Young modulus is discretized as a piece-wise constant function $E_h \in S_0^h$ when $\alpha = 0$, while a point-wise discretization $E_h \in X_2^h$ is adopted when $\alpha > 0$. The discretization of the adjoint variables follows that of the corresponding state variable. The discretized form of the optimality system then, for the state variables $(\boldsymbol{v}_h, p_h, \boldsymbol{\eta}_h, \widehat{\boldsymbol{\eta}}_h)$, reads

$$\int_{\Omega_f(\widehat{\boldsymbol{\eta}})} (\nabla \cdot \boldsymbol{v}_h)\, \psi_h \, d\Omega = 0 \,, \tag{5.51}$$

$$\int_{\Omega_f(\widehat{\boldsymbol{\eta}})} [(\rho_f(\boldsymbol{v}_h \cdot \nabla)\boldsymbol{v}_h) \cdot \boldsymbol{\phi}_h - p_h \nabla \cdot \boldsymbol{\phi}_h + \mu_f \nabla \boldsymbol{v}_h : \nabla \boldsymbol{\phi}_h] \, d\Omega + \tag{5.52}$$

$$\int_{\Omega_s(\widehat{\boldsymbol{\eta}})} \frac{E_h}{2(1+\nu)} \nabla \boldsymbol{\eta}_h : \nabla \boldsymbol{\phi}_h + \frac{E_h \nu}{(1+\nu)(1-2\nu)} (\nabla \cdot \boldsymbol{\eta}_h)(\nabla \cdot \boldsymbol{\phi}_h) \, d\Omega = 0 \,,$$

$$\int_{\Omega_s(\widehat{\boldsymbol{\eta}})} \nabla \widehat{\boldsymbol{\eta}}_h : \nabla \widehat{\boldsymbol{\eta}}_{ha} \, d\Omega = 0 \,, \tag{5.53}$$

$$\int_{\Omega_s(\widehat{\boldsymbol{\eta}})} (\boldsymbol{v}_h - \tau(\boldsymbol{\eta}_h - \widehat{\boldsymbol{\eta}}_h)) \cdot \boldsymbol{\beta}_{ha} \, d\Omega = 0 \,. \tag{5.54}$$

For the adjoint variables $(\boldsymbol{v}_{ha}, p_{ah})$ we have to solve

$$\int_{\Omega_f} (\nabla \cdot \boldsymbol{v}_{ha}) \psi_h \, d\Omega = 0 \,, \tag{5.55}$$

$$\begin{aligned}
&\int_{\Omega_f} p_{ha} \nabla \cdot \boldsymbol{\phi}_h \, d\Omega + \frac{1}{\tau} \int_{\Omega_s} [\mu_s \nabla \boldsymbol{v}_{ha} : \nabla \boldsymbol{\phi}_h + \lambda_s (\nabla \cdot \boldsymbol{v}_{ha})(\nabla \cdot \boldsymbol{\phi}_h)] \, d\Omega + \\
&\quad \int_{\Omega_f} \Big[(\rho_f (\boldsymbol{\phi}_h \cdot \nabla) \boldsymbol{v}_h) \cdot \boldsymbol{v}_{ha} + (\rho_f (\boldsymbol{v} \cdot \nabla) \boldsymbol{\phi}_h) \cdot \boldsymbol{v}_{ha} - \nabla \cdot (\mu_f \nabla \boldsymbol{\phi}_h) \cdot \boldsymbol{v}_{ha} \Big] \, d\Omega + \\
&\frac{1}{\tau} \int_{\Omega_d} \omega (\boldsymbol{\eta}_h - \boldsymbol{\eta}_d) \boldsymbol{\phi}_h \, d\Omega = 0 \,,
\end{aligned} \tag{5.56}$$

$$\begin{aligned}
&\int_{\Omega_s} \nabla \widehat{\boldsymbol{\eta}}_{ha} : \nabla \boldsymbol{\phi}_h \, d\Omega = - \int_{\Omega_s} [\mu_s \nabla \boldsymbol{v}_{ha} : \nabla \boldsymbol{\phi}_h + \lambda_s (\nabla \cdot \boldsymbol{v}_{ha})(\nabla \cdot \boldsymbol{\phi}_h)] \, d\Omega + \\
&\quad \int_{\Omega_d} \omega (\boldsymbol{\eta}_h - \boldsymbol{\eta}_d) \delta \widehat{\boldsymbol{\eta}}_h \, d\Omega \,,
\end{aligned} \tag{5.57}$$

and for the control E_h we can write the following equation

$$\int_{\Omega_s} [(\mathbf{S}(\boldsymbol{\eta}_h) : \nabla \boldsymbol{v}_{ha} + \beta E_h) \varphi_h + \alpha \nabla E_h \cdot \nabla \varphi_h] \, d\Omega = 0 \,, \tag{5.58}$$

for all test functions $(\boldsymbol{\phi}_h, \widehat{\boldsymbol{\eta}}_{ha}) \in \mathbf{X}_2^h$, $(\psi_h, \boldsymbol{\beta}_{ha}) \in S^h$, $\varphi_h \in S_0^h$ or $\varphi_h \in X_2^h$.

5.2.1 Test 1. Displacement enhancement

In order to validate our optimal control algorithm we consider a simple test case. The plane channel domain with the geometrical properties is reported on the left of Figure 5.1. The fluid domain Ω_f and the solid one Ω_s are coupled at the interface Γ_i. Our optimal control problem aims to reach a target displacement $\boldsymbol{\eta}_d$ in the solid subset Ω_d, by finding the optimal value of the Young modulus in Ω_s. On the fluid inlet AB and outlet EF we impose Neumann boundary conditions, with given pressure, namely $p_{in} = 11.5kPa$ and $p_{out} = 10kPa$. The solid right boundary is free to move with fixed end-points C and D. The domain is symmetric with respect to the left axis AF. We set the solid and fluid densities as $\rho_s = \rho_f = 1000kg/m^3$, fluid kinematic viscosity $\nu_f = 0.07m^2/s$, Young modulus $E = 10^6 Pa$ and Poisson modulus $\nu = 0.2$. With this choice of the physical properties we have laminar fluid motion in the channel. The above value of the Young modulus is the reference one which is used in the uncontrolled case and as initial guess for the optimal control algorithm. We use a multigrid approach

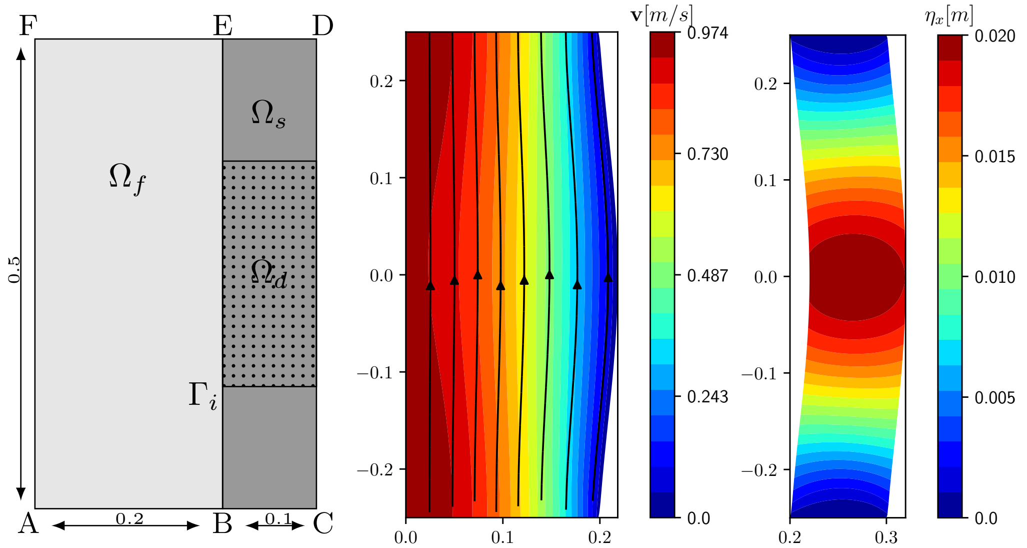

Figure 5.1: Test case domain (left). The dotted square Ω_d is the controlled region. Velocity field profile with streamlines (center) and solid displacement field (right) for the reference solution with no control.

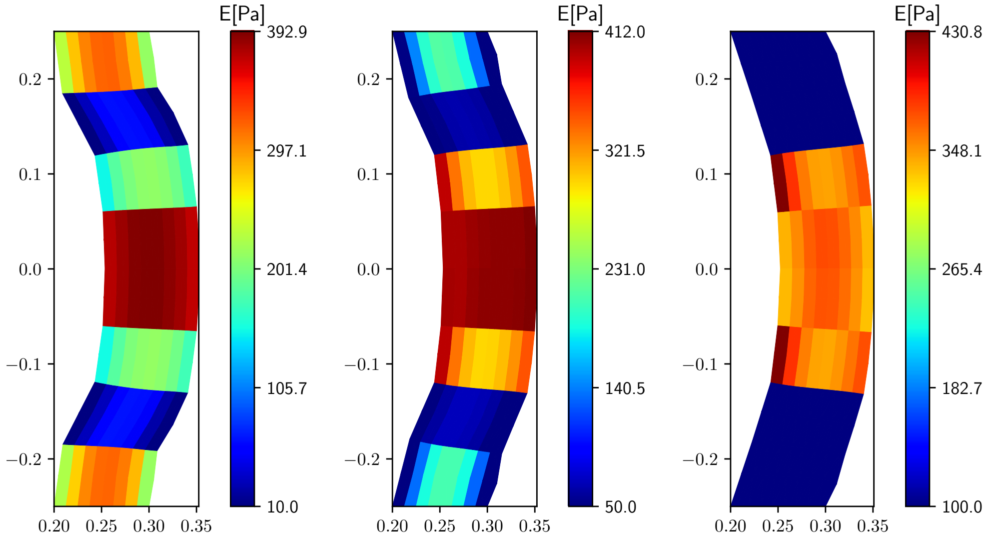

Figure 5.2: Young modulus E fields, discretization $l = 3$ with different $E_{min} = 10Pa$ (left), $50Pa$ (center), $100Pa$ (right). E and E_{min} are scaled by $2.4 \cdot 10^3$.

for the solution of both the state and adjoint systems. The coarsest grid $l = 0$ has $n_e = 8$ quadratic elements and the finer levels are obtained through

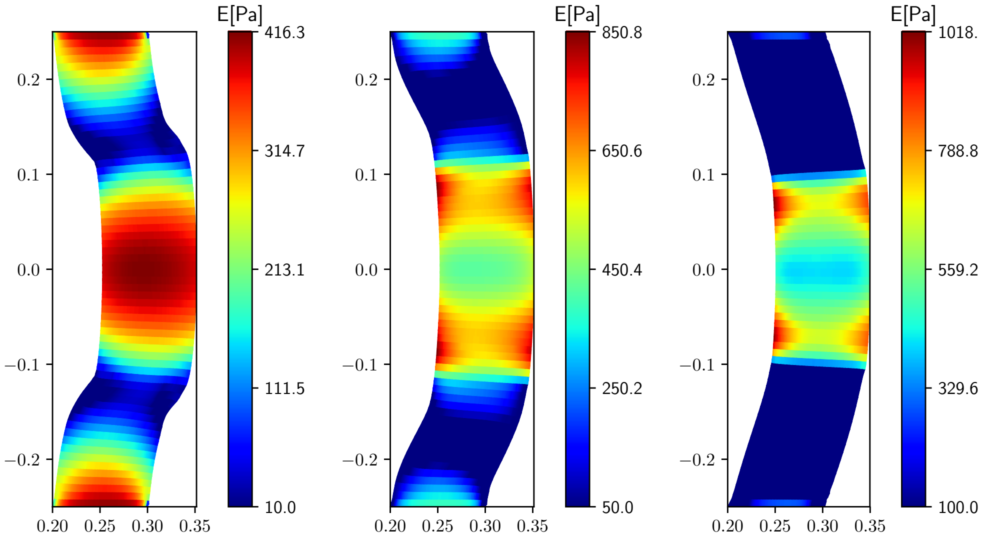

Figure 5.3: Young modulus E fields, discretization $l = 6$ with different $E_{min} = 10Pa$ (left), $50Pa$ (center), $100Pa$ (right). E and E_{min} are scaled by $2.4 \cdot 10^3$.

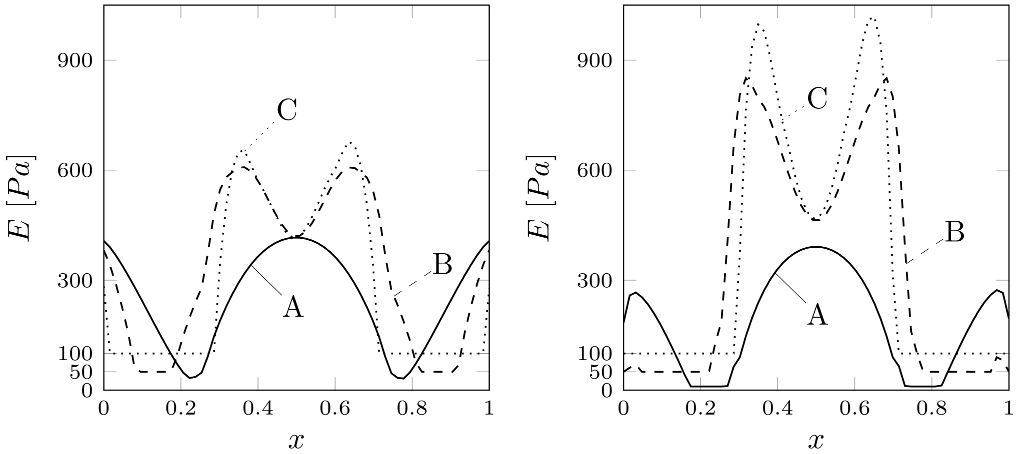

Figure 5.4: Young modulus profile on the solid vertical mid-line (left) and on the interface Γ_i (right), with different $E_{min} = 10Pa$ (A), $50Pa$ (B), $100Pa$ (C). E and E_{min} are scaled by $2.4 \cdot 10^3$.

a standard mid-point refinement approach. We solve the optimal control problem with different discretization levels, the finest one $l = 6$ has $n_e = 8192$ elements (33153 grid nodes).

The reference solution obtained with no control is reported in Figure 5.1.

The fluid velocity profile with streamlines and the solid displacement field are shown in the center and on the right of the same Figure, respectively. The fluid deforms the solid, obtaining a smooth solid profile, with a maximum deformation of $0.02m$ obtained in the central region of Ω_d. We choose the target displacement $\eta_x = 0.05m$ in the region Ω_d, and wish to obtain a flat solid profile, with large deformations. The displacement in the remaining part of the solid domain is not controlled and therefore we can have any value solution of the state system. Our choice of the target is such that the solid profile we aim to recover can be obtained only if the Young modulus is not uniform in the whole solid domain, with a complex distribution. We remark that this test case has been studied with the optimal control approaches presented in Chapters 3 and 4 as well.

In Figure 5.2 we report the profile of the Young modulus E obtained after the optimization process, for $l = 3$ and with different values of the Young modulus lower bound E_{min}. In order to improve the readability of the Figures we scaled all E values by $2.4{\cdot}10^3$. By comparing these results with the reference solution we notice that the control is able to obtain a profile close to the desired one. The Young modulus highest values are located near the middle point of the right side, which is the target region Ω_d, in order to try to recover the desired uniform displacement. In the upper and lower parts of the solid sub-domain the solution is almost symmetric. By increasing the Young modulus lower limit the region near the solid endpoints where $E = E_{min}$ becomes larger, as well as the maximum value of E in the central region.

Table 5.1: Objective functionals. E_{min} is scaled by $2.4 \cdot 10^3$. The reference case with no control is labeled with NC.

	$E_{min}[Pa]$				
Level	10	50	100	200	NC
2	$1.63{\cdot}10^{-7}$	$2.08{\cdot}10^{-7}$	$1.82{\cdot}10^{-7}$	$2.73{\cdot}10^{-6}$	$1.23{\cdot}10^{-5}$
3	$1.41{\cdot}10^{-7}$	$1.12{\cdot}10^{-7}$	$1.53{\cdot}10^{-7}$	$2.58{\cdot}10^{-6}$	$1.23{\cdot}10^{-5}$
4	$1.23{\cdot}10^{-7}$	$1.62{\cdot}10^{-7}$	$1.18{\cdot}10^{-7}$	$2.58{\cdot}10^{-6}$	$1.23{\cdot}10^{-5}$
5	$1.19{\cdot}10^{-7}$	$9.17{\cdot}10^{-8}$	$1.16{\cdot}10^{-7}$	$2.52{\cdot}10^{-6}$	$1.23{\cdot}10^{-5}$
6	$7.15{\cdot}10^{-8}$	$4.18{\cdot}10^{-8}$	$7.20{\cdot}10^{-8}$	$2.23{\cdot}10^{-6}$	$1.23{\cdot}10^{-5}$

In Figure 5.3 we report the results obtained on the finest grid, $l = 6$, with the same values of E_{min}. By comparing these results with those obtained on a coarser grid (Figure 5.2), it is worth noticing that the solution is similar. Clearly, in the case $l = 6$, the number of degrees of freedom available for the optimal control is higher and then, with higher resolution, the solid deformation is closer to the desired one, see Table 5.1. In this Table we report the functional obtained with different grid resolution, from $l = 2$ to $l = 6$ and with different values of the Young modulus lower bound E_{min}. The effects of the penalty constraints are more important with higher lower bounds and then the solution obtained is further away from the target one, in particular when $E_{min} = 200Pa$. We would like to point out that the functionals obtained with $E_{min} = 50Pa$ are lower than those with $E_{min} = 10Pa$. Although it may seem strange, we recall that in the context of optimization problems many local minima can exist, thus the final solution attained is usually affected by the choice of the initial guess and by the evolution of the solution during the optimization process. The Young modulus profile, obtained with different values of E_{min}, on the solid mid-line and on the fluid-solid interface is shown in Figure 5.4.

5.2.2 Test 2. Displacement reduction

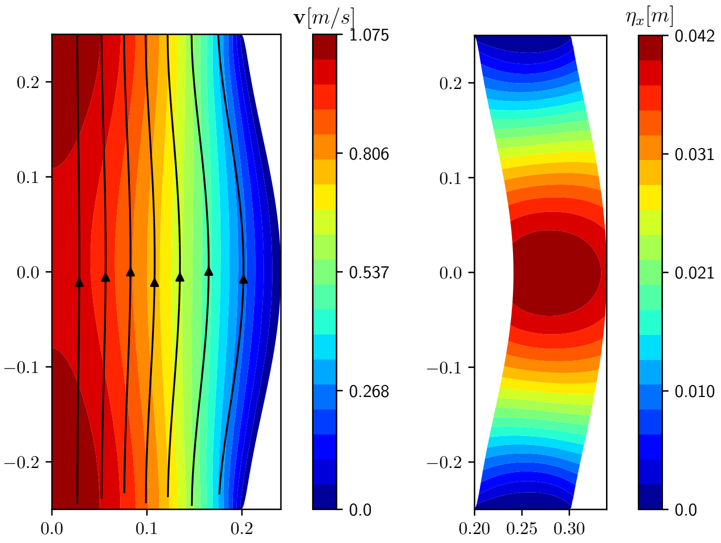

Figure 5.5: Velocity field profile with streamlines (left) and solid displacement field (right) for the reference solution with no control.

With this test we want to test our method against a displacement reduction problem. Since we expect that the control tries to increase the Young

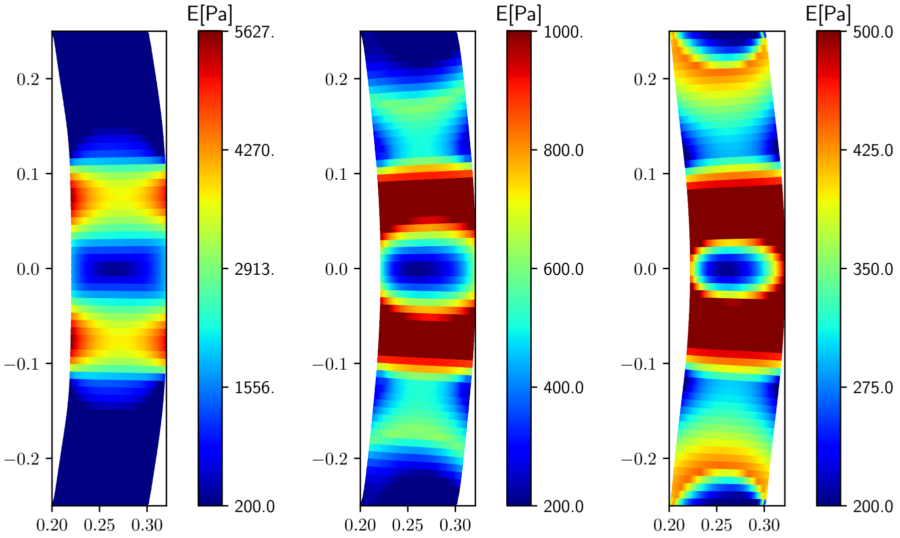

Figure 5.6: Young modulus E fields, discretization $l = 6$ with different $E_{max} = \infty$ (left), $1000Pa$ (center), $500Pa$ (right). E and E_{max} are scaled by $2.4 \cdot 10^3$.

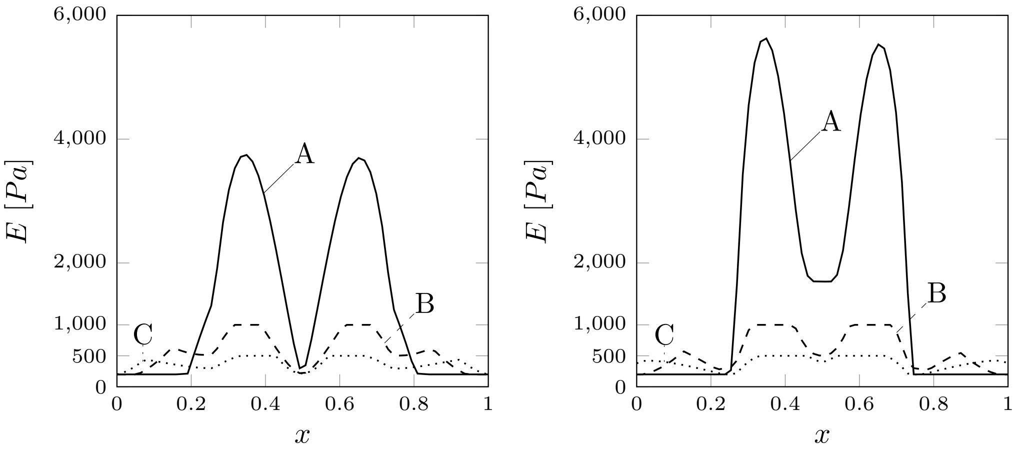

Figure 5.7: Young modulus profile on the solid vertical mid-line (left) and on the interface Γ_i (right), with different $E_{max} = \infty$ (A), $1000Pa$ (B), $500Pa$ (C). E and E_{max} are scaled by $2.4 \cdot 10^3$.

modulus in order to reduce the solid deformation, we impose also an upper bound to the control. The domain, boundary conditions and material properties are the same as in the previous test case. However, the value of the Young modulus used for the reference case with no control is reduced

Table 5.2: Objective functionals. E_{max} is scaled by $2.4 \cdot 10^3$. The reference case with no control is labeled with NC.

	$E_{max}[Pa]$					
Level	500	750	1000	1500	∞	NC
3	$5.65 \cdot 10^{-8}$	$4.21 \cdot 10^{-8}$	$3.69 \cdot 10^{-8}$	$1.53 \cdot 10^{-8}$	$1.45 \cdot 10^{-8}$	$3.64 \cdot 10^{-6}$
6	$4.64 \cdot 10^{-8}$	$3.41 \cdot 10^{-8}$	$2.94 \cdot 10^{-8}$	$1.55 \cdot 10^{-8}$	$4.25 \cdot 10^{-9}$	$3.64 \cdot 10^{-6}$

from the previous test and set to $480 \cdot 10^3 Pa$. Thus the displacement in the uncontrolled situation is now higher and is reported on the right of Figure 5.5, while the fluid velocity profile is shown on the left of the same figure. We choose as target displacement a uniform value $\eta_x = 0.02m$ in the target region Ω_d, thus wishing to reduce the solid deformation.

We now report and analyze the results obtained with different values of the upper bound on the control, ranging from $500Pa$ to ∞ (i.e. no upper bound imposed). In Figure 5.6 the Young modulus profile and the solid deformation field are reported from left to right for $E_{max} = \infty$, $1000Pa$ and $500Pa$. The Young modulus profile, obtained with different values of E_{max}, on the solid mid-line and on the fluid-solid interface is shown in Figure 5.7. When no upper limits are imposed on the control, the optimal profile of E has two peaks close to the boundaries of the controlled domain Ω_d, while in the rest of the solid domain the control has a uniform value equal to the lower bound $E_{min} = 200Pa$. When we set upper limits, the E distribution still has two peaks in the same region, but now their height is cut by the constraint. For a quantitative comparison we gathered in Table 5.2 the objective functionals obtained at the end of the optimization process. The lowest functional value corresponds to the case where the upper limit is not imposed and it increases when we set stricter limits on the control E.

5.2.3 Test 3. Control with gradient regularization

In this test case we want to recover smoother controls, so we impose further regularization on the gradient of the control. With referral to the (5.58), we take $\alpha > 0$ so that $E \in H^1$ and investigate the effects of the choice of α. We study again the solid displacement enhancement problem of the test in Section 5.2.1. The domain and the reference configuration with no control

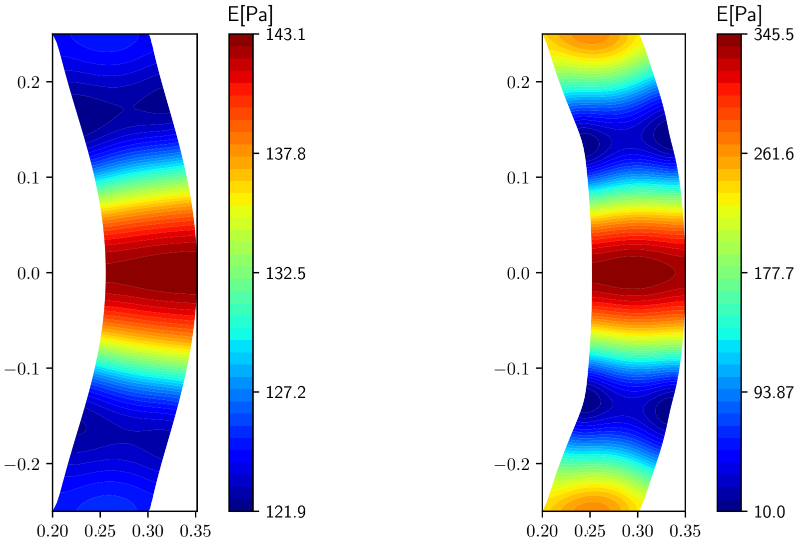

Figure 5.8: Young modulus E fields, discretization $l = 6$ with $E_{min} = 10Pa$ and $\alpha = 10^{-1}$ (left), $\alpha = 10^{-3}$ (right). E and E_{min} are scaled by $2.4 \cdot 10^3$.

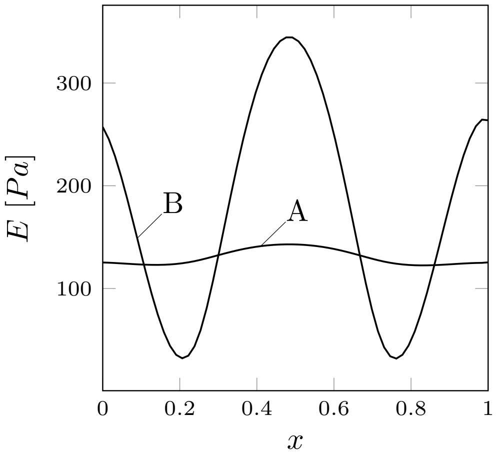

Figure 5.9: Young modulus profile on the solid vertical mid-line, with $E_{min} = 10Pa$ and $\alpha = 10^{-1}$ (A), $\alpha = 10^{-3}$ (B). E and E_{min} are scaled by $2.4 \cdot 10^3$.

are the same as in Figure 5.1. We recall that the aim of this test consists in matching the target deformation $\eta_x = 0.05m$ in the controlled region Ω_d, starting from a maximum displacement of about $0.02m$.

In Figure 5.8 the Young modulus profile is shown for $\alpha = 10^{-1}$ and 10^{-3} with $E_{min} = 10Pa$. In Table 5.3 we report the functional values obtained by changing the lower bound E_{min} and with the same values of α. The add of

Table 5.3: Objective functionals. E_{min} is scaled by $2.4 \cdot 10^3$. The reference case with no control is labeled with NC.

	$E_{min}[Pa]$				
α	10	50	100	200	NC
10^{-1}	$3.29{\cdot}10^{-7}$	$3.29{\cdot}10^{-7}$	$3.51{\cdot}10^{-7}$	$2.68{\cdot}10^{-6}$	$1.23{\cdot}10^{-5}$
10^{-3}	$9.79{\cdot}10^{-8}$	$9.20{\cdot}10^{-8}$	$3.22{\cdot}10^{-7}$	$2.68{\cdot}10^{-6}$	$1.23{\cdot}10^{-5}$

the regularization term leads to smoother solutions if compared with those of Test 1, in particular with the higher value of α. In this case we have an optimal solution where the limits on the control are inactive and the control is not very effective. This can be deduced also from Figure 5.9, where the Young modulus profile on the solid vertical mid-line is reported and has an almost uniform value in the whole solid. For $\alpha = 10^{-1}$, we obtain the same functional for different values of E_{min} which means that the control is higher than the lower constraint in the whole domain. By reducing α, the regularization term becomes less important and the optimal solution recovered by the algorithm is closer to both the target one and to the one obtained without such term in Section 5.2.1.

Conclusions

In this work we applied the optimal control principles to stationary fluid-structure interaction systems. We first implemented a monolithic FSI direct solver in an in-house finite element code with multi-grid capabilities and validated our solver by performing well known benchmarks. Then we used the adjoint formalism for the optimization of FSI systems. We extended the velocity field into the solid domain in order to obtain a symmetric adjoint system, coupling adjoint variables and forces on the interface, thus allowing us to use the same coupled solver for the state and adjoint systems. To solve the minimization problem we adopted the Lagrangian multiplier method and the optimality system was recovered by imposing the first order necessary conditions. This optimality system was solved with an iterative gradient-based algorithm implemented in the FEM code.

In Chapter 3 we studied an optimal pressure boundary control applied to the FSI system. The objective has been the matching of a displacement field in a particular region of the solid domain by controlling the pressure on a fluid boundary, such as the inlet or an auxiliary duct. We compared the optimal solutions obtained with a simple steepest descent algorithm and with a quasi-Newton one. Both methods showed accuracy and robustness. However, the quasi-Newton algorithm converged faster to the optimal solution.

In Chapter 4 a distributed optimal control was investigated. An external force acting on the solid modifies the shape of the solid domain in order to recover the desired objective. We considered as objectives both fluid velocity and solid displacement matching ones.

Finally, in Chapter 5, we studied a stationary inverse parameter estimation problem where the goal was to find the optimal distribution of the Young modulus in the solid subdomain in order to obtain a desired solid deformation or shape. Upper and lower limits on the Young modulus were taken into account, since they are of great interest in practical applications. We used a projected gradient method in order to satisfy the inequality constraints on the control. The Young modulus was taken in L^2, then we added a regularization term based on its gradient and obtained a control in H^1. The results obtained show the feasibility and robustness of the approaches proposed.

A test case was considered with all the optimal control methods presented. We used the same geometry, objective functional, reference state, material properties and boundary conditions in order to compare the effectiveness of the methods. With the distributed control the functional are the lowest, while when applying the pressure boundary control we recovered the highest values. This can be easily explained, in fact our distributed control can act directly in the solid controlled region, with great effectiveness. The effects of the boundary control instead have to propagate from the fluid boundary to the target domain that may be far away, which means that, in this case, the objective functional is less sensitive to the control parameter.

List of Figures

List of Tables

Bibliography

[1] *Code FEMuS*. `https://github.com/FemusPlatform/femus`. 55, 64, 83, 104

[2] R. A. Adams, *Sobolev spaces*, Academic Press, New York, 1975. 27

[3] L. Armijo, *Minimization of functions having lipschitz continuous first partial derivatives*, Pacific J. Math., 16 (1966), pp. 1–3. 63

[4] E. Aulisa, S. Bnà, and G. Bornia, *A monolithic ale newton–krylov solver with multigrid-richardson–schwarz preconditioning for incompressible fluid-structure interaction*, Computers & Fluids, 174 (2018), pp. 213–228. 7

[5] E. Aulisa, A. Cervone, S. Manservisi, and P. Seshaiyer, *A multilevel domain decomposition approach for studying coupled flow applications*, Comm. in Comput.l Phys., 6 (2009), pp. 319–341. 7

[6] E. Aulisa, S. Manservisi, and P. Seshaiyer, *A computational multilevel approach for solving 2d navier–stokes equations over non-matching grids*, Comput. meth. in appl. mech. and eng., 195 (2006), pp. 4604–4616. 64

[7] Y. Bazilevs, M.-C. Hsu, and M. Bement, *Adjoint-based control of fluid-structure interaction for computational steering applications*, Procedia Computer Science, 18 (2013), pp. 1989–1998. 4

[8] J. Bonet and R. D. Wood, *Nonlinear continuum mechanics for finite element analysis*, Cambridge university press, 1997. 10

[9] J. H. Bramble, *Multigrid methods*, vol. 294, CRC Press, 1993. 64

[10] S. Brenner and R. Scott, *The mathematical theory of finite element methods*, vol. 15, Springer Science, 2007. 27

[11] C. G. Broyden, J. Dennis Jr, and J. J. Moré, *On the local and superlinear convergence of quasi-newton methods*, IMA Journal of Applied Mathematics, 12 (1973), pp. 223–245. 49

[12] M. Bukač, S. Čanić, and B. Muha, *A partitioned scheme for fluid–composite structure interaction problems*, Journal of Computational Physics, 281 (2015), pp. 493–517. 7

[13] A. Calderer, S. Kang, and F. Sotiropoulos, *Level set immersed boundary method for coupled simulation of air/water interaction with complex floating structures*, Journal of Computational Physics, 277 (2014), pp. 201–227. 7

[14] D. Cerroni, R. Da Vià, and S. Manservisi, *A projection method for coupling two-phase vof and fluid structure interaction simulations*, Journal of Computational Physics, 354 (2018), pp. 646–671. 7

[15] D. Cerroni, D. Giommi, S. Manservisi, and F. Menghini, *Preliminary monolithic fluid structure interaction model for ventricle contraction*, Lecture Notes in Applied and Computational Mechanics, 84 (2018), pp. 217–231. 7

[16] D. Cerroni and S. Manservisi, *A penalty-projection algorithm for a monolithic fluid-structure interaction solver*, J. Computat. Phys., 313 (2016), pp. 13–30. 82

[17] D. Cerroni, S. Manservisi, and F. Menghini, *An improved monolithic multigrid fluid- structure interaction solver with a new moving mesh technique*, Internat. J. of Math. Mod. and Meth. in Appl. Sci., 9 (2015), pp. 227–234. 28, 64

[18] A. Chinchuluun, P. M. Pardalos, R. Enkhbat, and I. Tseveendorj, *Optimization and optimal control*, Springer, 2010. 41

[19] L. Chirco, R. Da Vià, and S. Manservisi, *An optimal control method for fluid structure interaction systems via adjoint boundary pressure*, Journal of Physics: Conference Series, 923 (2017), p. 012026. 56

[20] L. Chirco and S. Manservisi, *An adjoint based pressure boundary optimal control approach for fluid-structure interaction problems*, Computers and Fluids, 182 (2019), pp. 118–127. 56

[21] P. G. Ciarlet, *Mathematical Elasticity: Volume I: three-dimensional elasticity*, North-Holland, 1988. 10, 15

[22] J. Donea, S. Giuliani, and J.-P. Halleux, *An arbitrary lagrangian-eulerian finite element method for transient dynamic fluid-structure interactions*, Computer methods in applied mechanics and engineering, 33 (1982), pp. 689–723. 28

[23] L. Failer, D. Meidner, and B. Vexler, *Optimal control of a linear unsteady fluid–structure interaction problem*, Journal of Optimization Theory and Applications, 170 (2016), pp. 1–27. 4

[24] L. Formaggia, A. Quarteroni, and A. Veneziani, *Cardiovascular Mathematics, vol. 1*, Springer, Heidelberg, 2009. 7

[25] M. B. Giles and N. A. Pierce, *An introduction to the adjoint approach to design*, Flow, turbulence and combustion, 65 (2000), pp. 393–415. 42

[26] A. Gilmanov, T. B. Le, and F. Sotiropoulos, *A numerical approach for simulating fluid structure interaction of flexible thin shells undergoing arbitrarily large deformations in complex domains*, Journal of Computational Physics, 300 (2015), pp. 814–843. 7

[27] V. Girault and P.-A. Raviart, *Finite element methods for Navier-Stokes equations: theory and algorithms*, vol. 5, Springer Science & Business Media, 2012. 104

[28] M. Gunzburger and S. Manservisi, *The velocity tracking problem for navier–stokes flows with bounded distributed controls*, SIAM Journal on Control and Optimization, 37 (1999), pp. 1913–1945. 41

[29] M. Gunzburger and S. Manservisi, *Analysis and approximation for linear feedback control for tracking the velocity in navier-stokes flows*, Computer Methods in Applied Mechanics and Engineering, 189 (2000), pp. 803–823. 41

[30] M. D. Gunzburger, *Perspectives in flow control and optimization*, vol. 5, Siam, 2003. 3, 41, 43, 59, 103

[31] M. D. Gunzburger, H. Kim, and S. Manservisi, *On a shape control problem for the stationary navier-stokes equations*, ESAIM: Mathematical Modelling and Numerical Analysis, 34 (2000), pp. 1233–1258. 42

[32] J. Hron and S. Turek, *A monolithic fem/multigrid solver for an ale formulation of fluid-structure interaction with applications in biomechanics*, in Fluid-structure interaction, Springer, 2006, pp. 146–170. 56

[33] V. John and G. Matthies, *Higher-order finite element discretizations in a benchmark problem for incompressible flows*, International Journal for Numerical Methods in Fluids, 37 (2001), pp. 885–903. 32

[34] A. A. Johnson and T. E. Tezduyar, *Mesh update strategies in parallel finite element computations of flow problems with moving boundaries and interfaces*, Computer methods in applied mechanics and engineering, 119 (1994), pp. 73–94. 28

[35] J. Kim and T. R. Bewley, *A linear systems approach to flow control*, Annu. Rev. Fluid Mech., 39 (2007), pp. 383–417. 41

[36] P. Le Tallec and J. Mouro, *Fluid structure interaction with large structural displacements*, Computer Meth. in Appl. Mech. and Eng., 190 (2001), pp. 3039–3067. 7, 28

[37] G. Leugering, S. Engell, A. Griewank, M. Hinze, R. Rannacher, V. Schulz, M. Ulbrich, and S. Ulbrich, *Constrained optimization and optimal control for partial differential equations*, vol. 160, Springer Science & Business Media, 2012. 41

[38] E. Lund, H. Møller, and L. A. Jakobsen, *Shape design optimization of stationary fluid-structure interaction problems with large displacements and turbulence*, Structural and Multidisciplinary Optimization, 25 (2003), pp. 383–392. 3

[39] S. Manservisi, *An optimal control approach to an inverse nonlinear elastic shell problem applied to car windscreen design*, Computer methods in applied mechanics and engineering, 189 (2000), pp. 463–480. 97

[40] S. Manservisi and M. Gunzburger, *Variational inequality formulation of an inverse elasticity problem*, Applied Numerical Mathematics, 34 (2000), pp. 99–126. 97

[41] K. Maute, M. Nikbay, and C. Farhat, *Sensitivity analysis and design optimization of three-dimensional non-linear aeroelastic systems by the adjoint method*, Internat. J. for Num. Meth. in Eng., 56 (2003), pp. 911–933. 3

[42] G. Nabh, *On high order methods for the stationary incompressible Navier-Stokes equations*, Interdisziplinäres Zentrum für Wiss. Rechnen der Univ. Heidelberg, 1998. 33

[43] B. R. Noack, M. Morzynski, and G. Tadmor, *Reduced-order modelling for flow control*, vol. 528, Springer Science & Business Media, 2011. 41

[44] J. Nocedal and S. Wright, *Numerical optimization*, Springer Science & Business Media, 2006. 41, 55, 63, 103

[45] R. W. Ogden, *Non-linear elastic deformations*, Courier Corporation, 1997. 26

[46] H. Park and W. Lee, *Feedback control of natural convection*, Computer methods in applied mechanics and engineering, 191 (2001), pp. 1013–1028. 41

[47] M. Perego, A. Veneziani, and C. Vergara, *A variational approach for estimating the compliance of the cardiovascular tissue: An inverse fluid-structure interaction problem*, SIAM Journal on Scientific Computing, 33 (2011), pp. 1181–1211. 42, 94

[48] T. Richter and T. Wick, *Optimal control and parameter estimation for stationary fluid-structure interaction problems*, SIAM Journal on Scientific Computing, 35 (2013), pp. B1085–B1104. 4, 94

[49] R. Rivlin, *Large elastic deformations of isotropic materials. i. fundamental concepts*, Philosophical Transactions of the Royal Society of London. Series A, Mathematical and Physical Sciences, 240 (1948), pp. 459–490. 25

[50] C. W. Rowley and D. R. Williams, *Dynamics and control of high-reynolds-number flow over open cavities*, Annu. Rev. Fluid Mech., 38 (2006), pp. 251–276. 41

[51] P. A. Sackinger, P. R. Schunk, and R. R. Rao, *A newton–raphson pseudo-solid domain mapping technique for free and moving boundary problems: a finite element implementation*, Journal of Computational Physics, 125 (1996), pp. 83–103. 28

[52] M. Schäfer, S. Turek, F. Durst, E. Krause, and R. Rannacher, *Benchmark computations of laminar flow around a cylinder*, in Flow simulation with high-performance computers II, Springer, 1996, pp. 547–566. 30

[53] J. C. Simo and T. J. Hughes, *Computational inelasticity*, vol. 7, Springer Science & Business Media, 2006. 22

[54] J. Sokolowski and J.-P. Zolesio, *Introduction to shape optimization*, in Introduction to Shape Optimization, Springer, 1992, pp. 5–12. 59, 60, 79

[55] T. E. Tezduyar, S. Sathe, R. Keedy, and K. Stein, *Space–time finite element techniques for computation of fluid–structure interactions*, Computer methods in applied mechanics and engineering, 195 (2006), pp. 2002–2027. 10

[56] T. E. Tezduyar, S. Sathe, and K. Stein, *Solution techniques for the fully discretized equations in computation of fluid–structure interactions with the space–time formulations*, Computer Methods in Applied Mechanics and Engineering, 195 (2006), pp. 5743–5753. 10

[57] S. Turek and J. Hron, *Proposal for numerical benchmarking of fluid-structure interaction between an elastic object and laminar incompressible flow*, in Fluid-structure interaction, Springer, 2006, pp. 371–385. 7, 30, 34

[58] Y. Wu and X.-C. Cai, *A fully implicit domain decomposition based ale framework for three-dimensional fluid–structure interaction with application in blood flow computation*, Journal of Computational Physics, 258 (2014), pp. 524–537. 7

[59] Y. Yan and D. E. Keyes, *Smooth and robust solutions for dirichlet boundary control of fluid–solid conjugate heat transfer problems*, Journal of Computational Physics, 281 (2015), pp. 759–786. 41